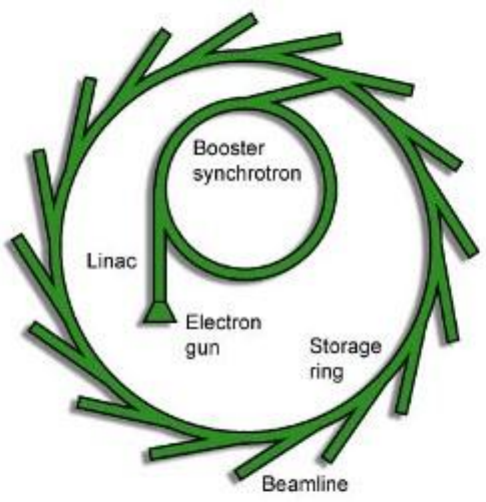

Photon metrology using Synchrotron light sources

Alan Owens
European Space Agency
Noordwijk, The Netherlands

Outline

Synchrotron radiation

Light Sources

Beamlines – controlling the beam

Photon metrology – basic characterization

Defect metrology

Pump and probe techniques

XAFS metrology
- Response functions
- Surface topology and metrology

Properties of Synchrotron radiation sources

- High brightness and high intensity, 10 orders of magnitude more than that of X-rays produced in conventional X-ray tubes.
- The production mechanism is unique in that it can be precisely described.
- High level of polarization (linear or elliptical).
- High collimation, small angular divergence of the beam.
- Low emittance - the product of source cross section and solid angle of emission is small.
- Wide tunability in energy/wavelength by monochromatization (from sub-eV up to MeV).
- High brilliance, exceeding other natural and artificial light sources by many orders of magnitude.
- Pulsed light emission with durations of 1 ns or less

Synchrotron (Ivaneko-Pomeranchuk) radiation

Classically an electron moving in a magnetic field will execute a spiral trajectory and radiate as a dipole. The emission is isotropic at the Larmor frequency

$$\nu_L = \frac{eB}{2\pi m_o c}$$ = 2.8 MHz per Gauss ,

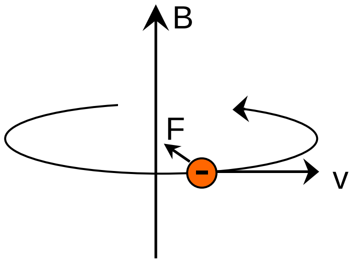

$$F = q\,(\vec{E} + \vec{V} \times \vec{B})$$

where *B* represents the magnetic field component perpendicular to the particle velocity vector.

If the electron is non-relativistic, the radiation is isotropic and is emitted only at the Larmor frequency. This is known as cyclotron radiation. In the relativistic case, synchrotron radiation is emitted in a relativistically narrow cone of angle, $\theta \sim \gamma^{-1}$, where γ is the particle energy in units of its rest energy (typically 10^3 - 10^4). The frequency distribution is no longer discrete as in the non-relativistic case, but is an asymmetric distribution with a maximum of the envelope at

$$\nu_m = 2/3\gamma^2 \nu_L$$

or in terms of energy

$$E_m = 5 \times 10^{-9} \gamma^2 B \quad \text{(keV)}$$

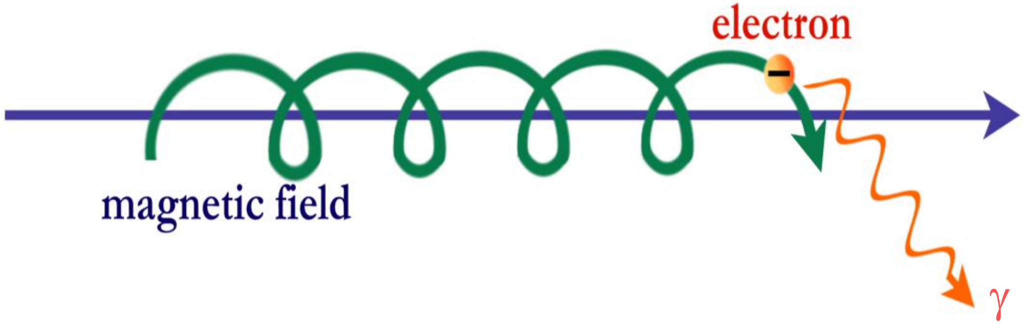

D. Iwanenko, I. Pomeranchuk, *On the maximal energy attainable in betatron*, Phys. Rev., **65** (1944) 343
J. Schwinger, "*On the Classical Radiation of Accelerated Electrons*", Phys. Rev.,**75** (1949)1912.

Synchrotron sources

Crab Nebula

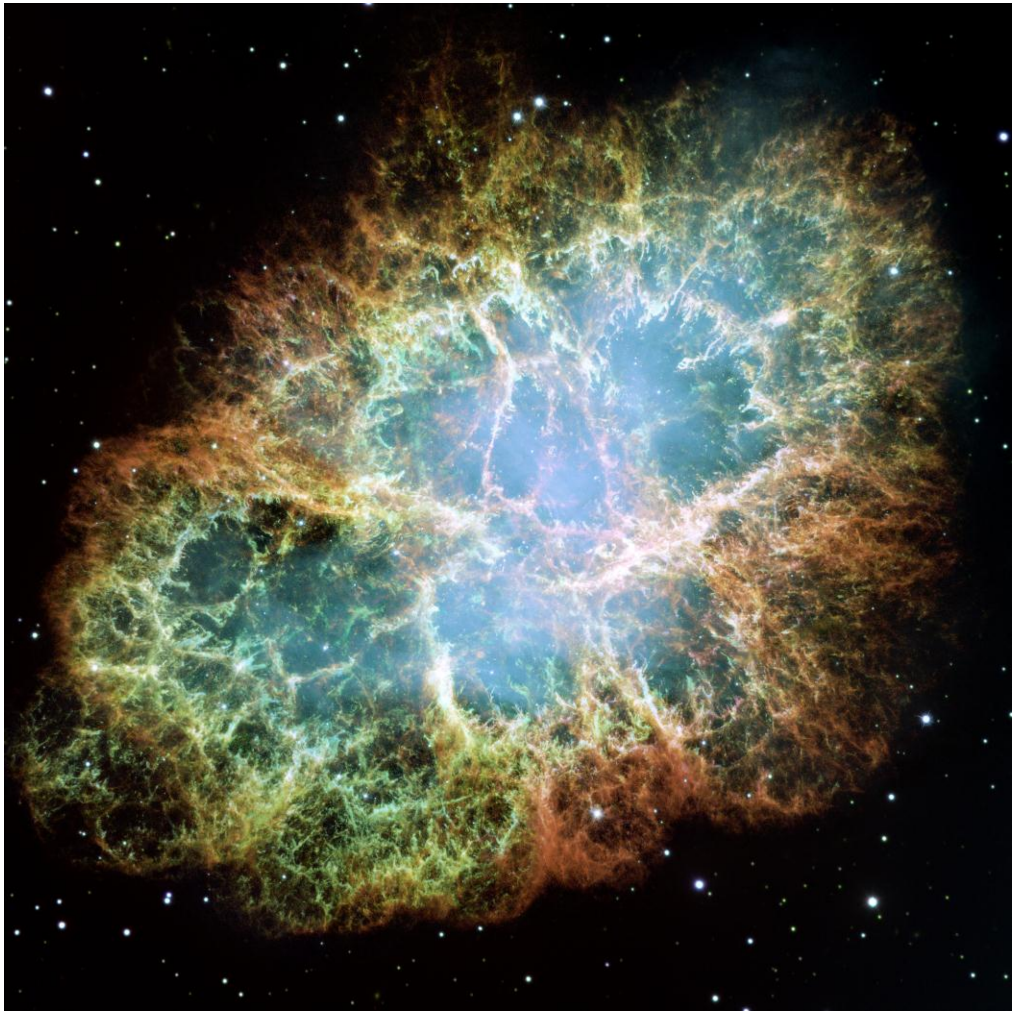

First light observed 1054 AD

“Song Shi”, official annals of the Song dynasty, chapter 12.

GE synchrotron, New York State

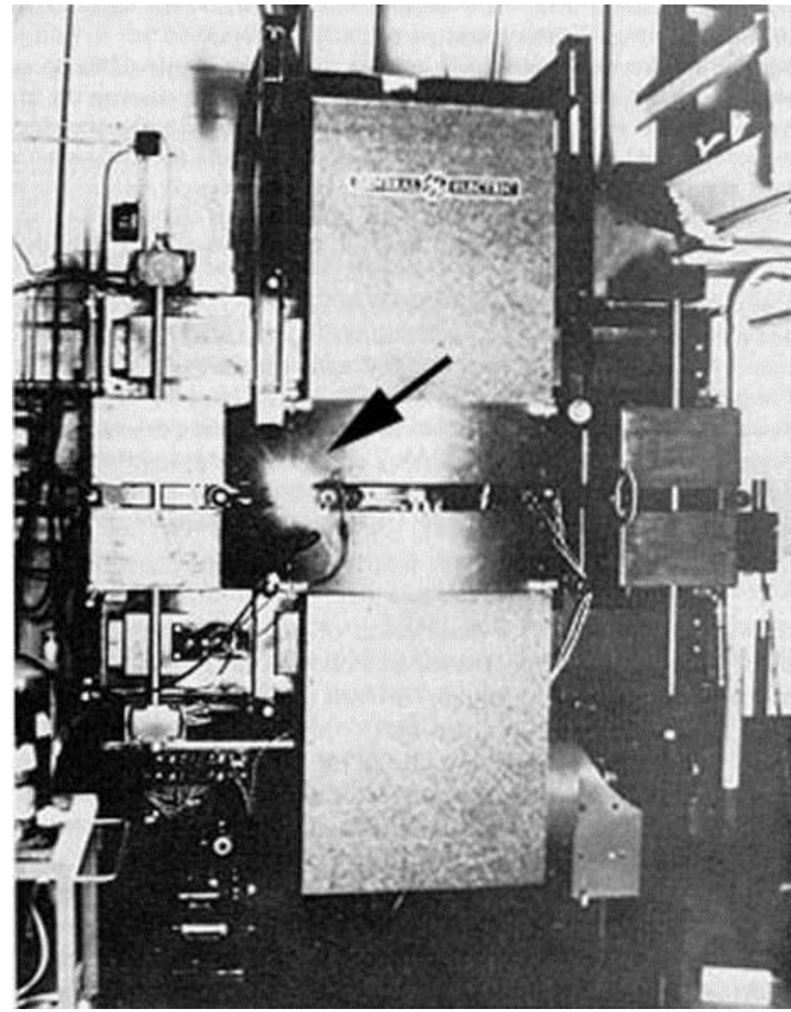

First light observed 1947 AD

Elder et al., "*Radiation from Electrons in a Synchrotron*", *Phys. Rev.*, 71(1947) 829

The Crab pulsar

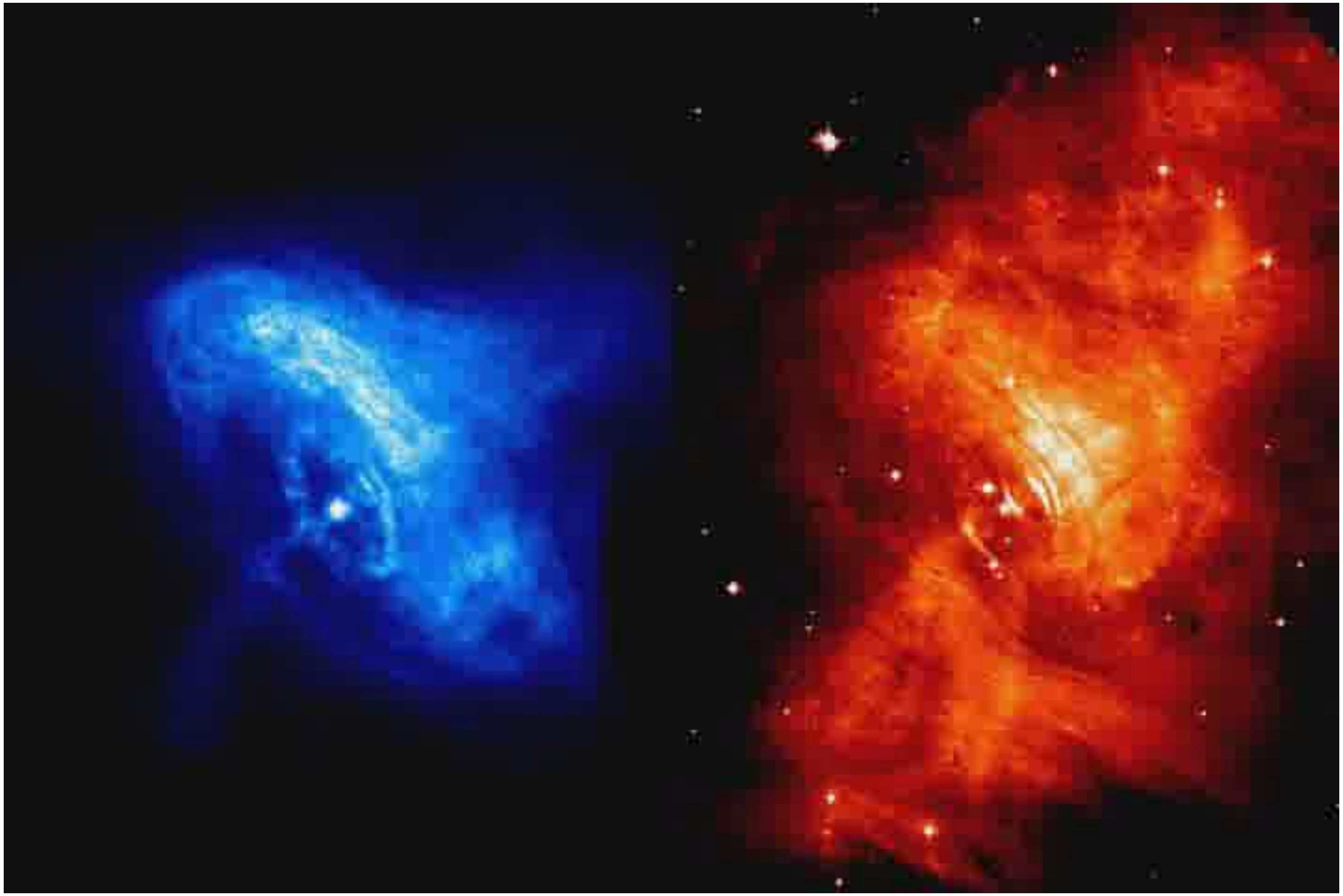

Chandra (0.3-3) keV

Hubble (optical)

The Crab pulsar

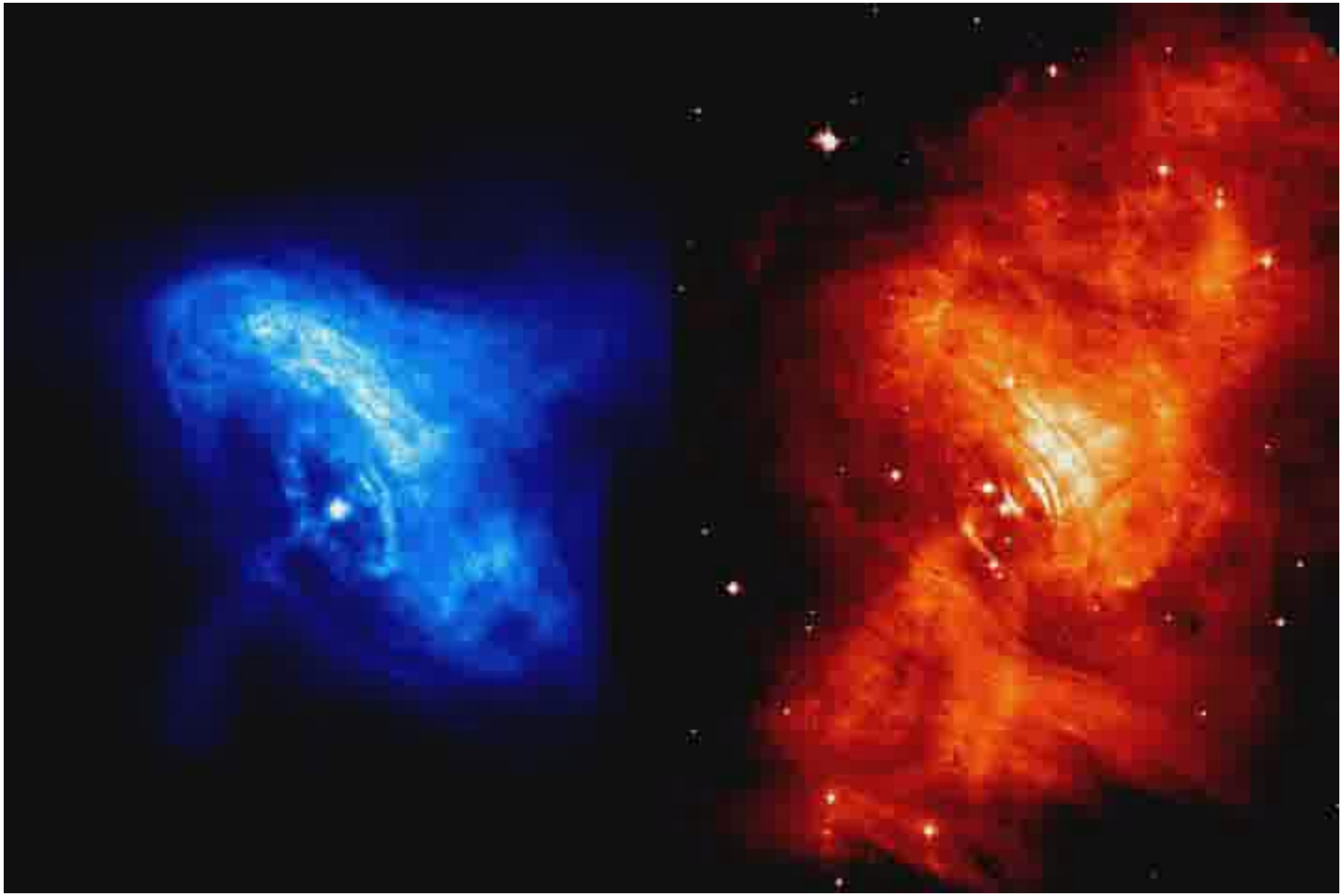

Chandra (0.3-3) keV Hubble (optical)

Practical implementation

Synchrotron radiation is electromagnetic radiation produced by relativistic charged particles accelerated in circular orbits

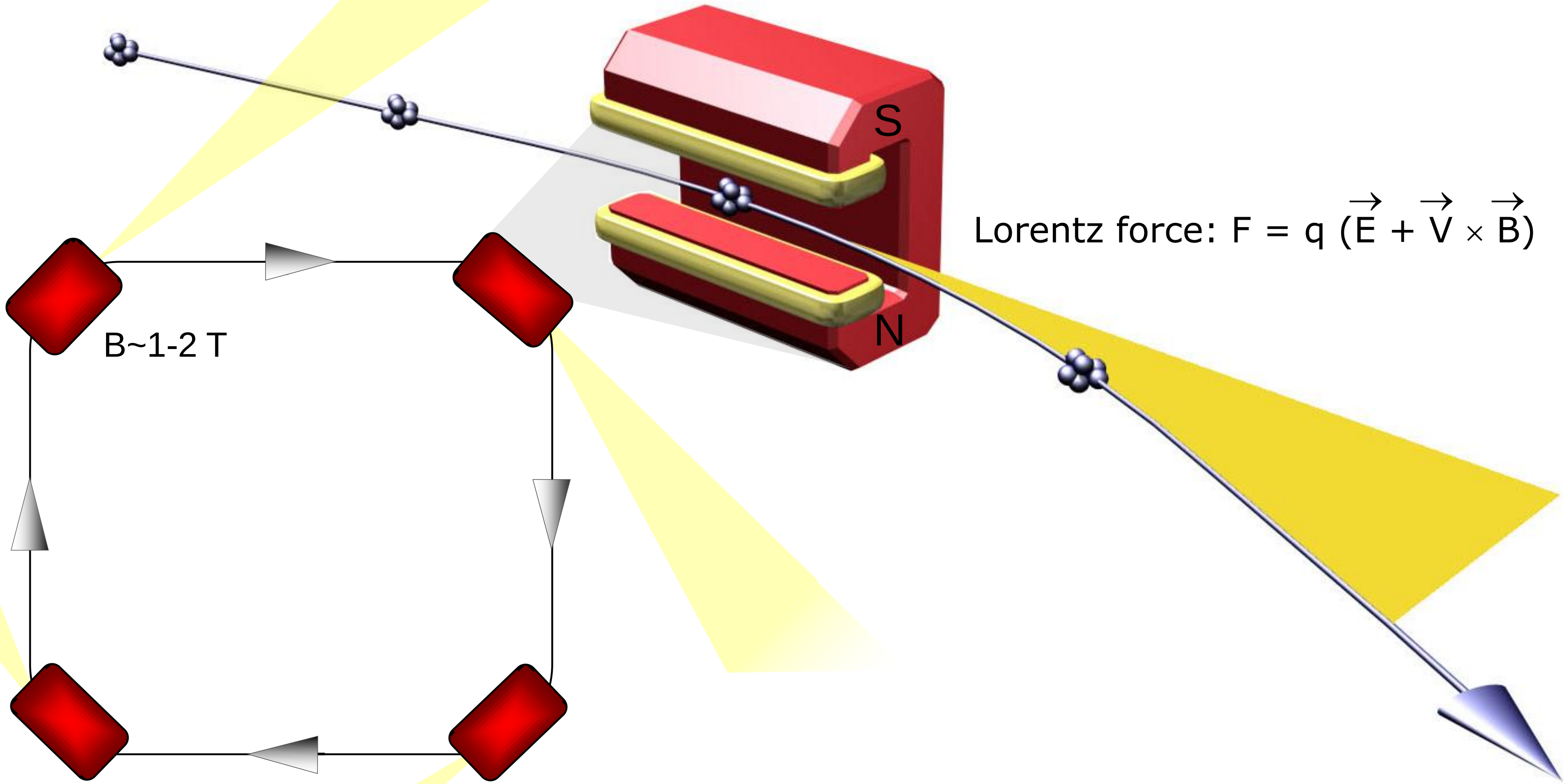

Lorentz force: $F = q\,(\vec{E} + \vec{V} \times \vec{B})$

Synchrotron radiation is emitted tangentially at each magnetic device in the form of horizontal layers (shown in yellow) with very little divergence. It can extracted via windows situated regularly along the length of the ring. Each beam feeds into a measurement station dedicated to a particular material analysis technique

Light sources

At present, there are over 50 synchrotron light sources operating world wide which can be broadly grouped into three categories, or generations.

1st generation synchrotron radiation light sources which were operated partially for synchrotron radiation and partially for other programs, such as high energy physics. Typically the light source was parasitic on the primary program. Examples include the CHESS facility at Cornell, USA and DORIS at DESY, Germany.

2nd generation synchrotron radiation light sources which are dedicated synchrotron radiation facilities but are not designed for low emittance or with straight sections for insertion devices. Examples include the Daresbury SRS in the UK and HASYLAB at DESY.

3rd generation synchrotron radiation light sources, which are dedicated synchrotron radiation facilities designed for low emittance and with many straight sections for incorporating insertion devices. Examples include Soleil & ESRF in France, the ALS in the USA, BESSY II in Germany and Diamond in the UK.

Considerable effort is now underway developing fourth-generation light sources, which will most likely combine a hard X-ray (wavelength less than 1Å) free-electron laser (FEL) with a very long undulator in a high-energy electron linear accelerator. Such a device would have a peak brightness many orders of magnitude beyond that of the third-generation sources, as well as pulse lengths of 100 fs or shorter, and be fully coherent.

Diamond Light Source, Harwell, UK

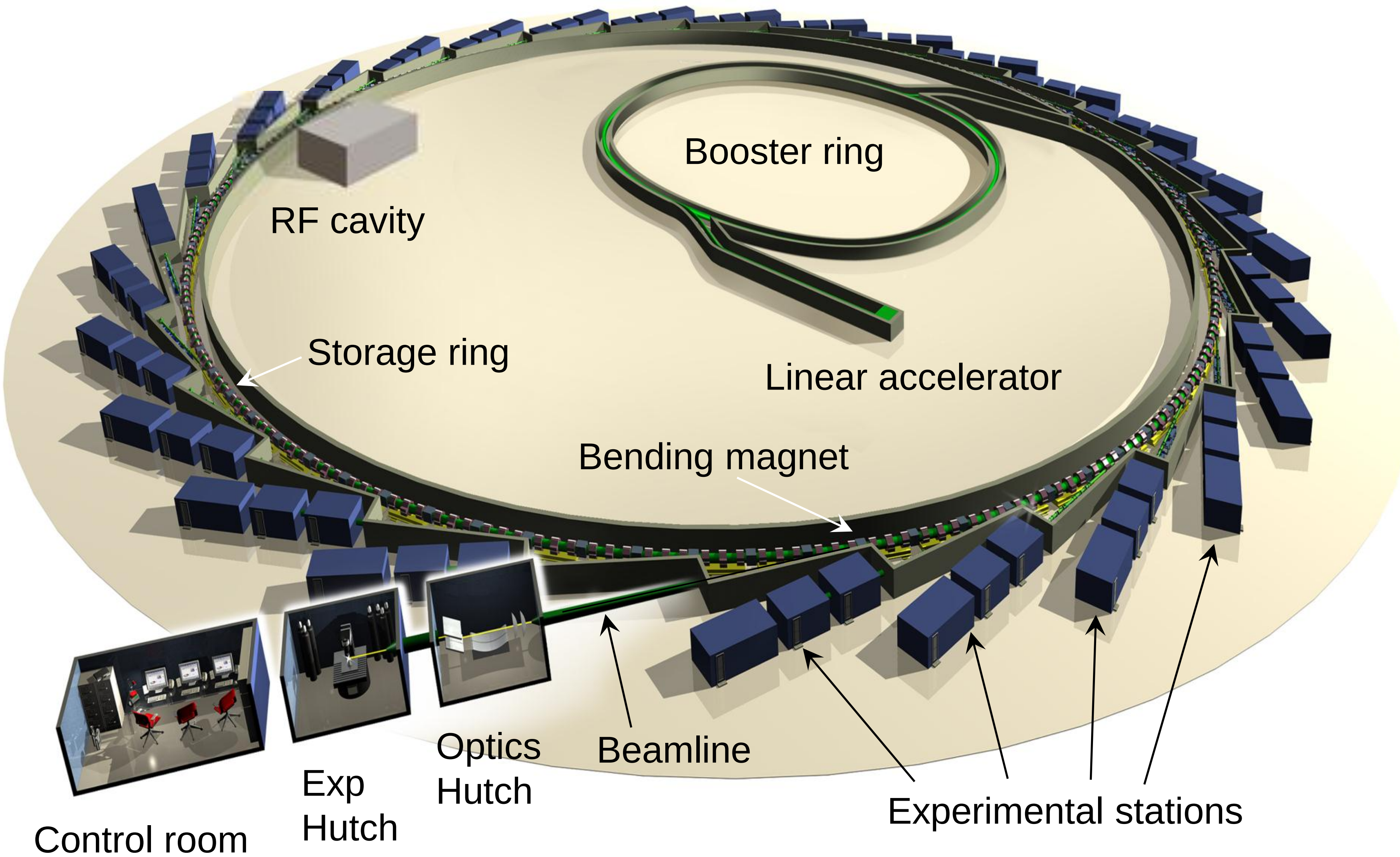

Flux and Brilliance

Each generation differs from the previous generation by innovation and is improved by at least an order of magnitude in performance, usually quantified by the flux and the brilliance of the source. The flux is defined as

$$\Phi = \frac{N_p}{0.1\% \, mrad}$$

(photons/(s, 0.1 % energy spread, mrad horizontally)

where N_p is the number of photons emitted per second for a given stored beam current.

The brilliance, B, is the peak flux density in phase space,

$$B = \frac{N_p}{0.1\%, mm^2, mrad^2}$$

The flux is a function only of the electron current and energy, while the brilliance takes into account the phase space defined by diffraction effects and the electron beam emittance.

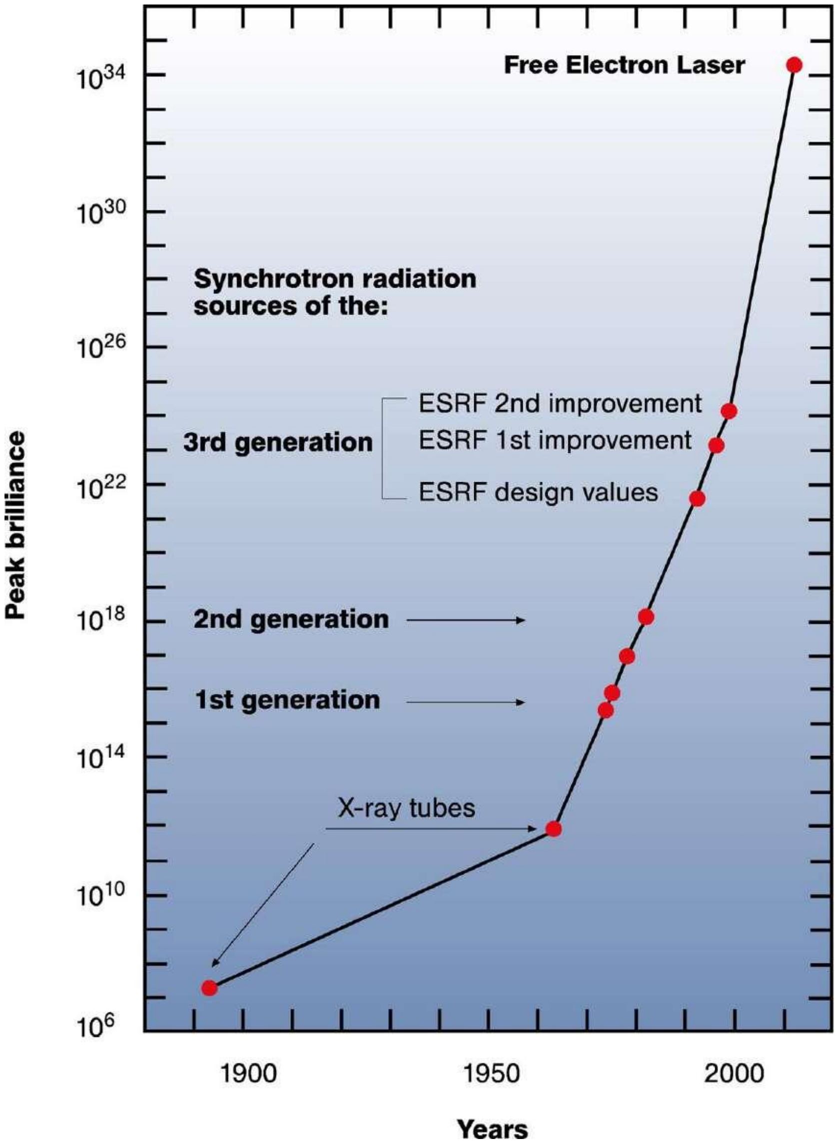

Properties of the beam

The beam emerging from the bending magnets is known as "white light" and has a well defined energy spectrum extending from the microwave through to the hard X-ray regions of the electromagnetic spectrum. The spectrum is usually characterized by its critical energy, E_c, which is defined as the energy at which half the radiant power is carried by photons above E_c. The critical energy is given by

$$E_c(\text{keV}) = 0.665E^2/\rho\ ,$$

where E is electron beam energy in GeV and ρ is the bending radius. Critical energies generally ranges from ~10 keV for second generation machines to ~50 keV for third generation machines (usable end energy ~4E_c).

White light direct from an extraction point is extremely intense with a brilliance of

~ 10^{15} photons $s^{-1}mm^{-2}mrad^{-2}$ (second generation machines)

~ 10^{20} photons $s^{-1}mm^{-2}mrad^{-2}$ (third generation machines)

For comparison a rotating anode X-ray generator has a brilliance

~ 10^9 photons $s^{-1}mm^{-2}mrad^{-2}$

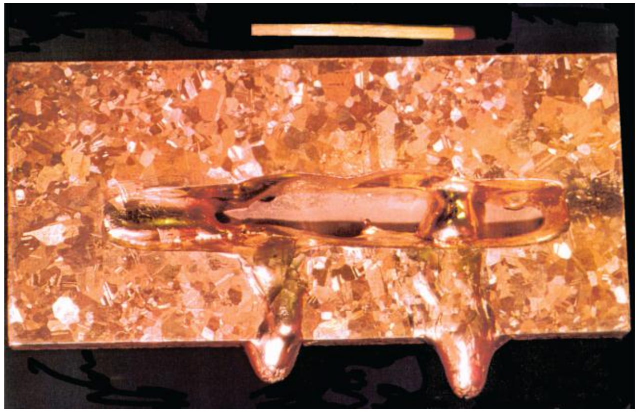

<u>Bottom line</u>: White light fluxes at a detector can be up to 10^{14} photons cm^{-2}

which will seriously melt it – count rates need to be in the range ~10^2-10^5 photons s^{-1}.

Flux reduction strategies

Absorbers	pros	cons
	simple	difficult to control harmonic amplification
Collimation/ Aperture reduction		
Pinholes Knife edges	very precise simple to implement	diffraction, difficult to align, leak above ~20 keV
Monochromaterizing		
	very effective reduces flux by many orders of magnitude	usefulness and energy range depend on quality of monochromater
Detuning the rocking curve		
	very effective also suppresses harmonics	need MOSTAB
Low current		
circulate less electrons	the best simple beam decay correction	affects whole light source users become unfriendly

Harmonics

Bragg reflection

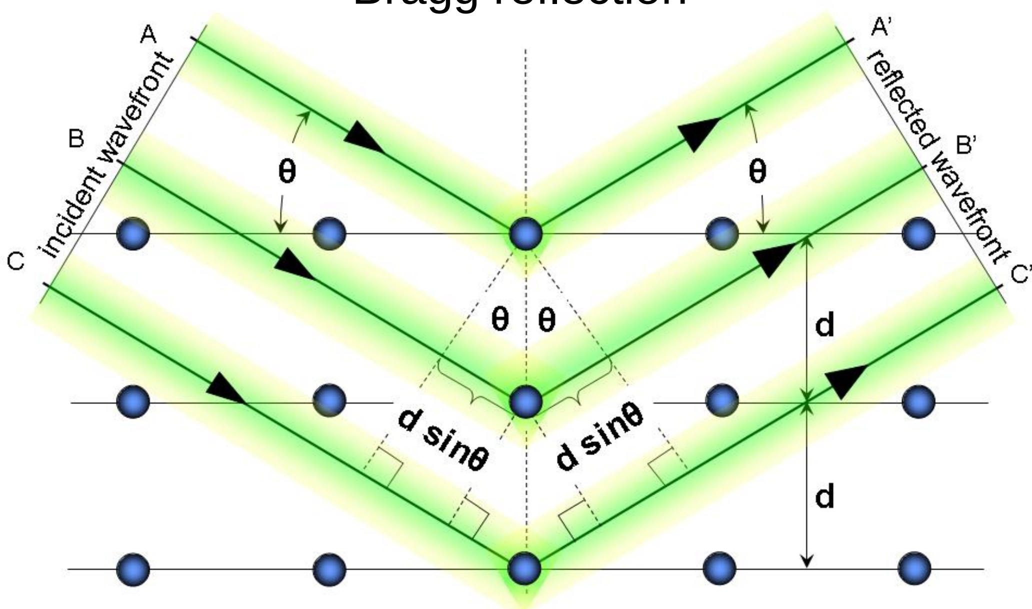

Since $2d\sin\theta = n\lambda$

the monochromator transmits not only the desired fundamental energy (n=1), but also higher harmonics of that energy.

Si crystals with a diamond structure (space group Fd3m(Oh7)) will not produce harmonics that satisfy the eq. $h+k+l=n$, where n is twice an odd number.

Common methods of reducing harmonic X-ray content include

- detuning the second crystal
- using a harmonic rejection mirror
- work at a high enough energy

Typically, when two Si(111) crystals are detuned by 50% on the rocking curve, the intensity of the third harmonic is reduced by a factor of 10^3.

Beamline layout

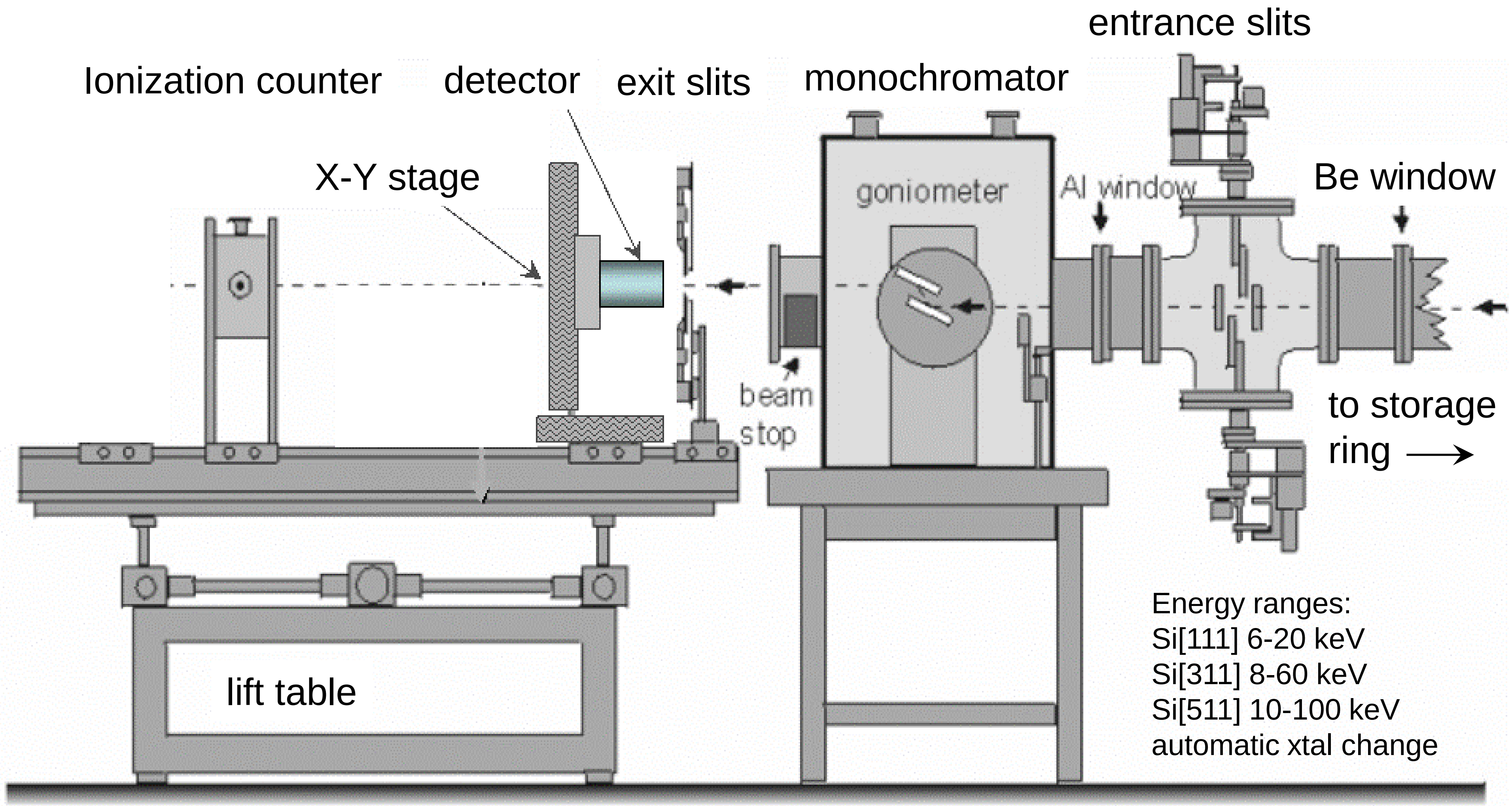

Beamline X-1 HASYLAB, DESY Hamburg

HASYLAB measurements

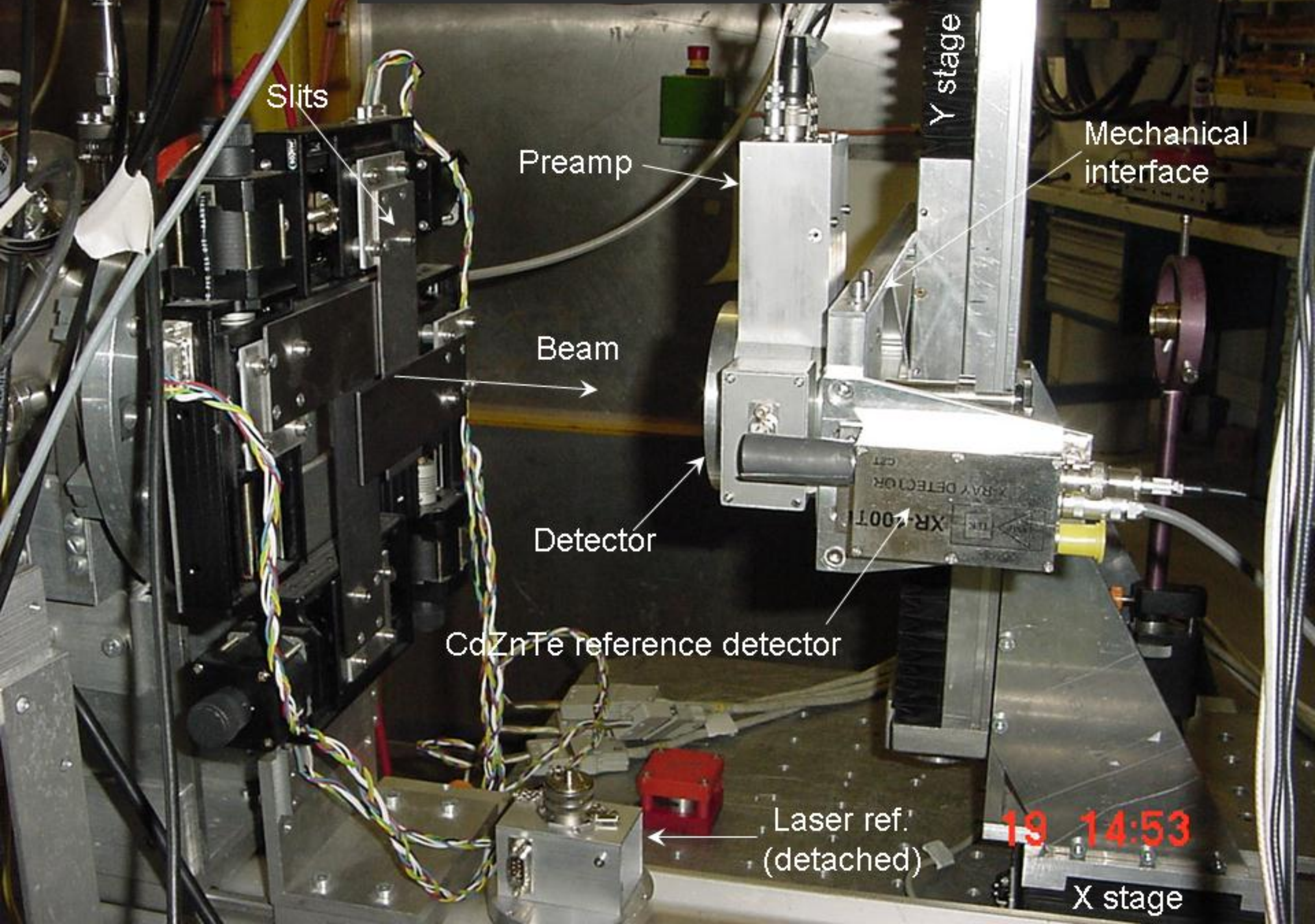

HASYLAB measurements

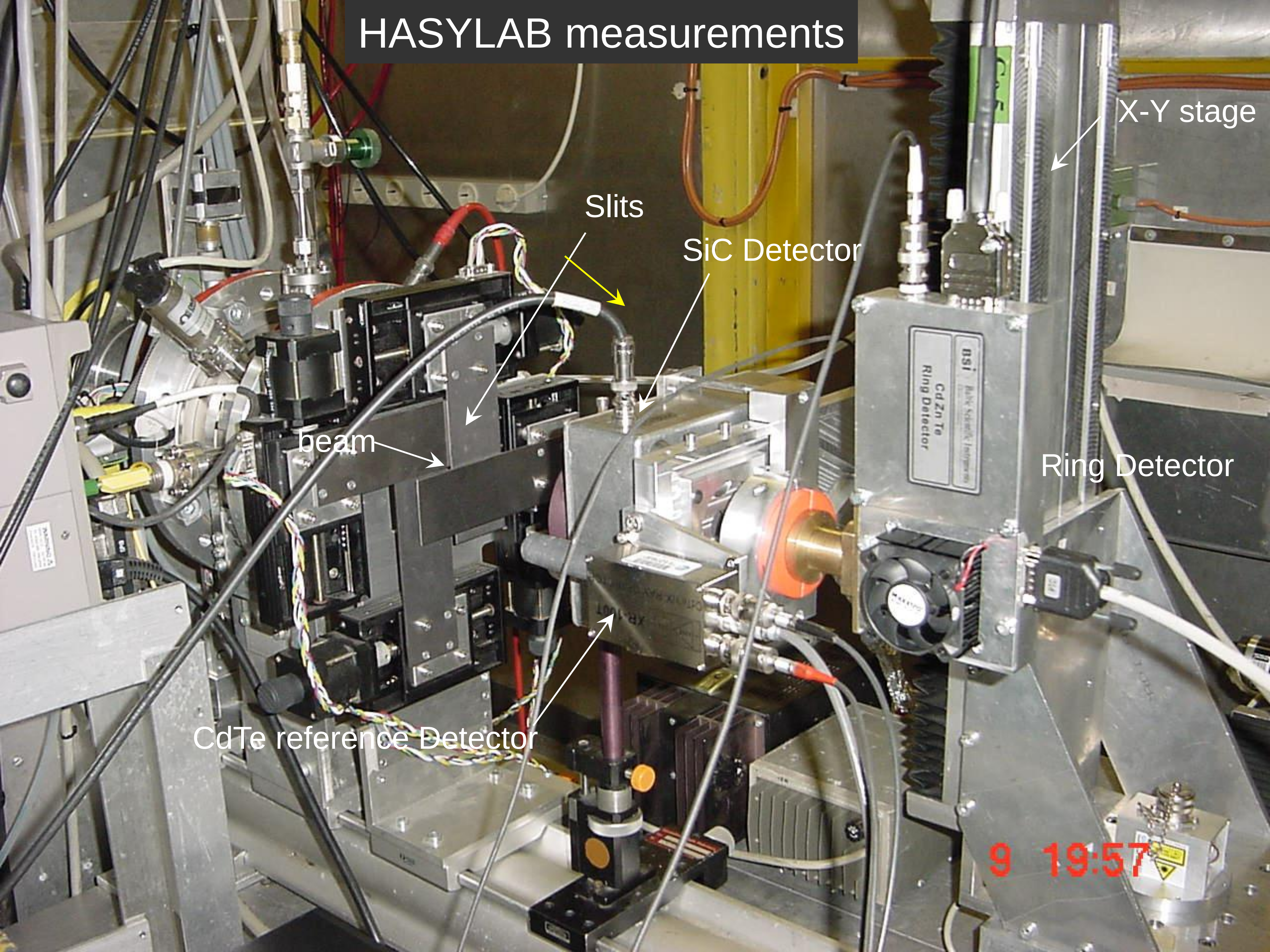

Insertion devices – Wigglers and Undulators

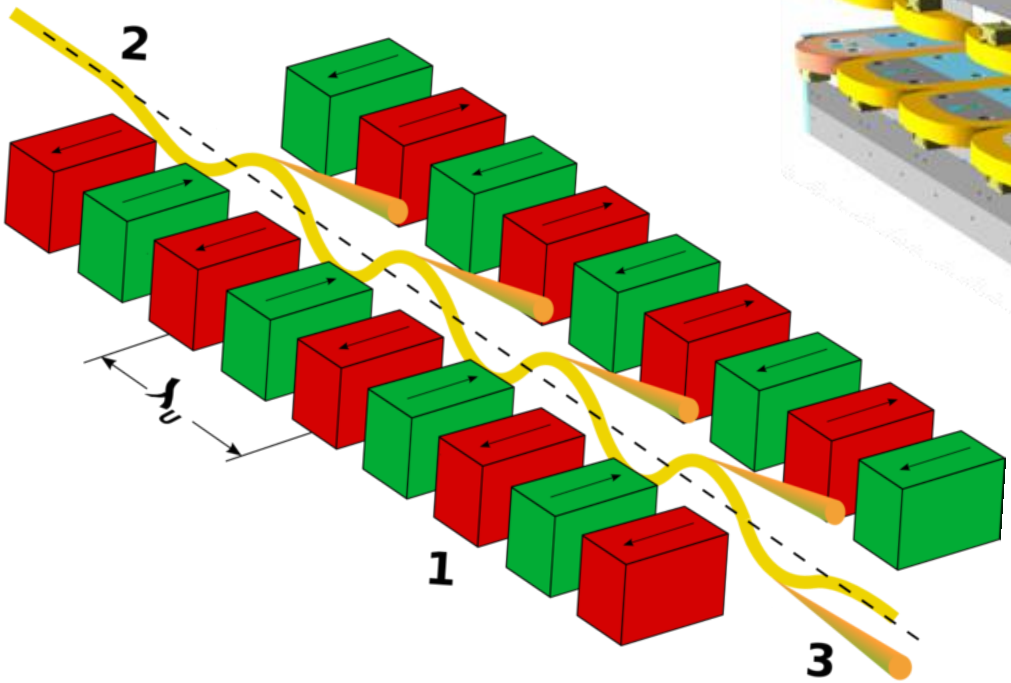

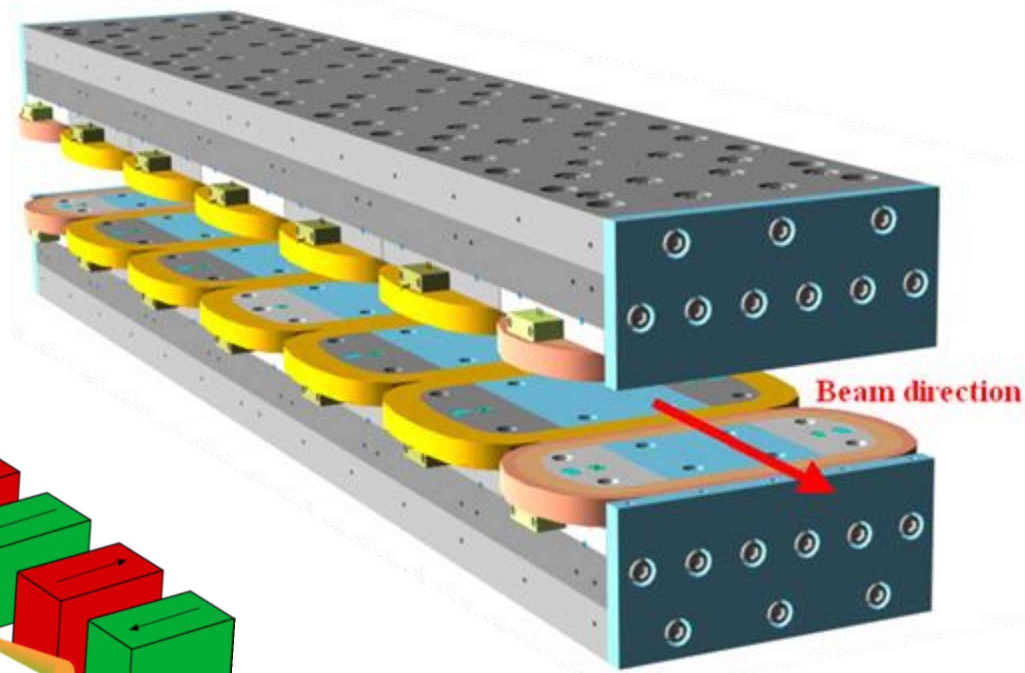

deflection parameter

$$K = \frac{eB\lambda_u}{2\pi\beta m_e c}$$

For *K*<< 1 the oscillation amplitude of the motion is small and the radiation displays interference patterns which lead to narrow energy bands. If *K*>>1 the oscillation amplitude is bigger and the radiation contributions from each field period sum up independently, leading to a broad energy spectrum. In this regime the device is no longer called an *undulator*; it is called a *wiggler.*

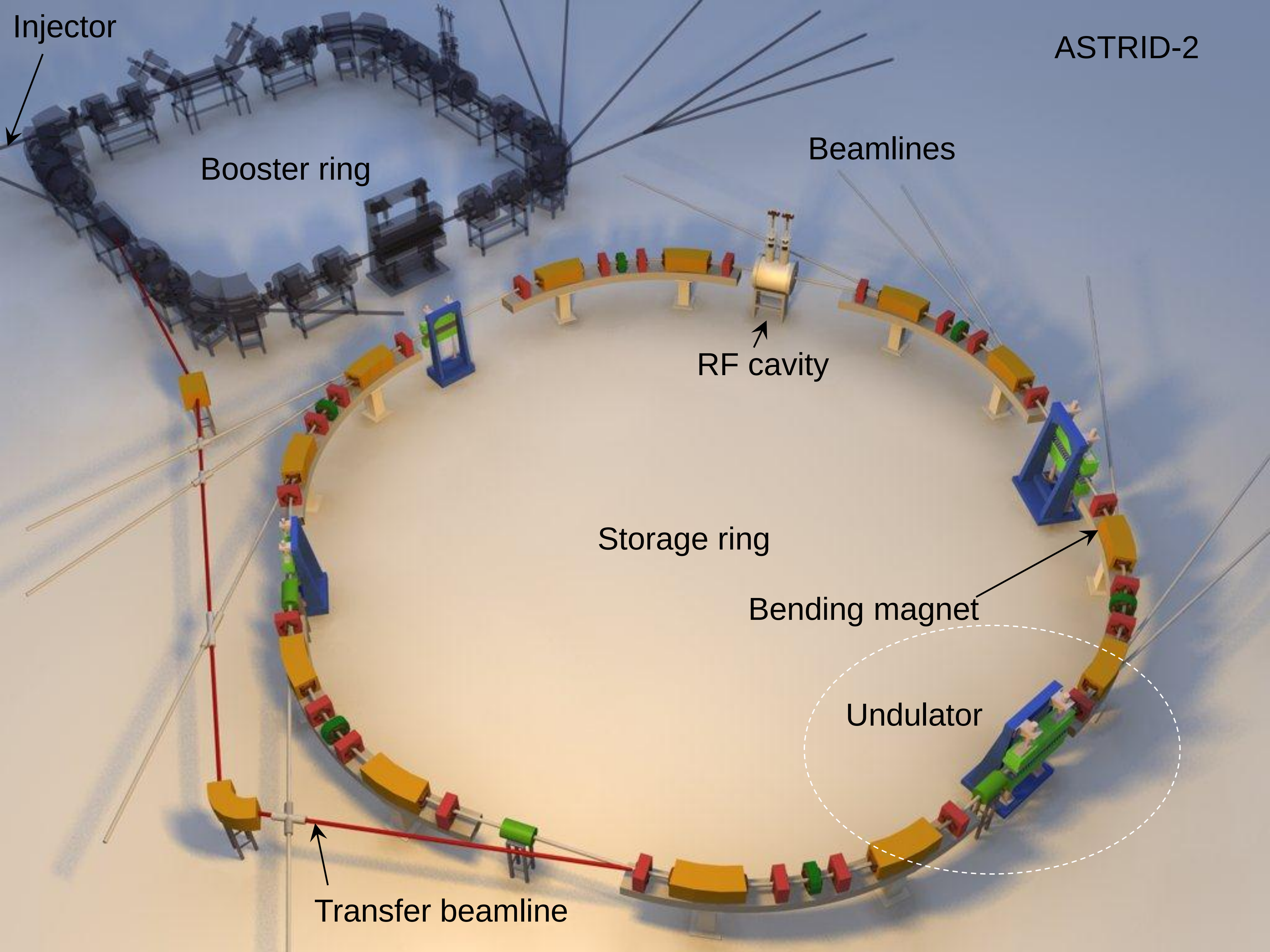
Injector
ASTRID-2
Booster ring
Beamlines
RF cavity
Storage ring
Bending magnet
Undulator
Transfer beamline

Enhancing the energy range - Insertion devices

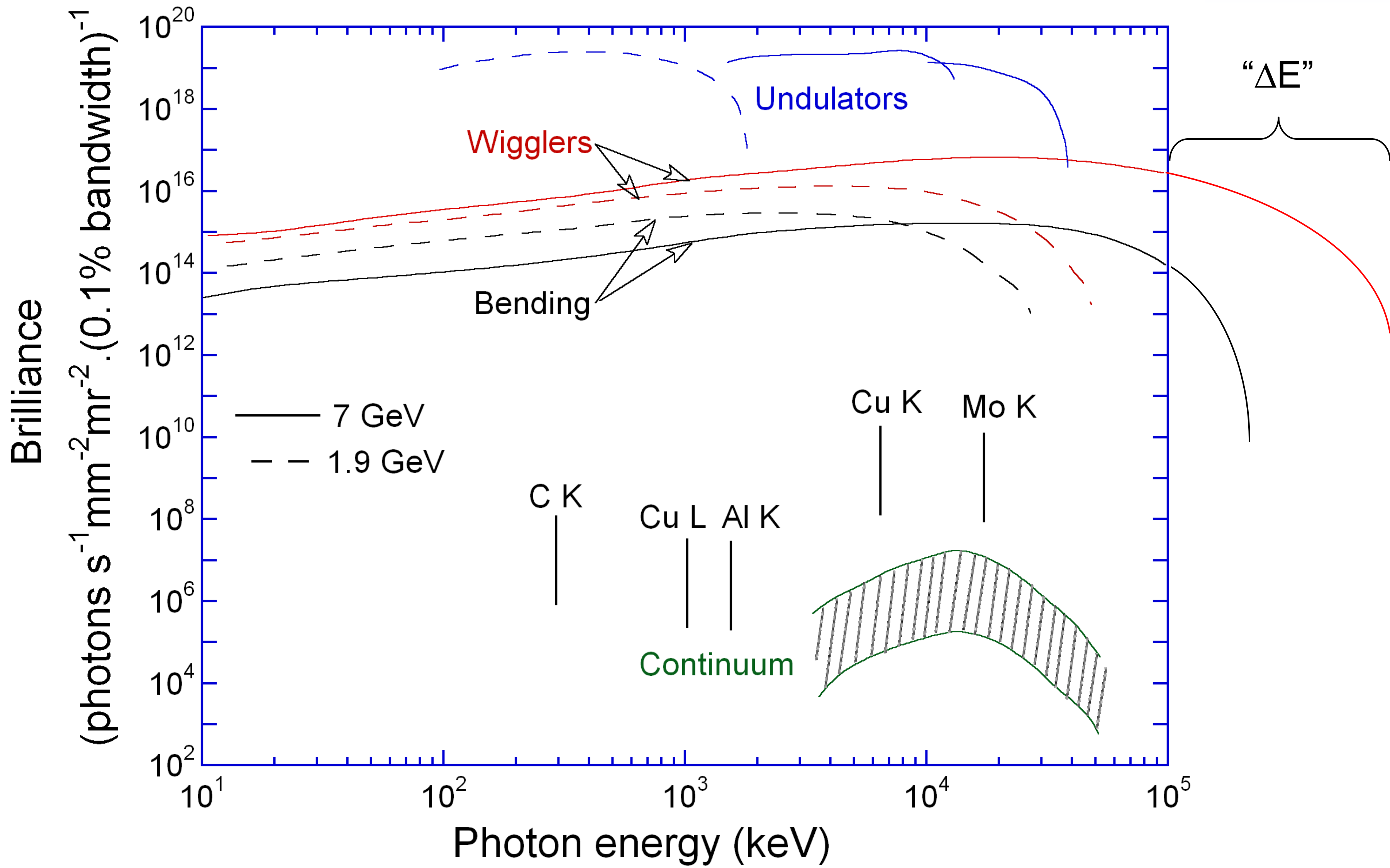

ESRF High energy spectra taken on beamline ID15

- Gamma-ray energies achieved using 2 insertion devices (asymmetrical multipole wiggler (AMPW) & superconducting wavelength shifter (SCWS)
- Energy range from 30 keV to 1 MeV
- Difficult to separate the monochromatic beam from white light above 800 keV

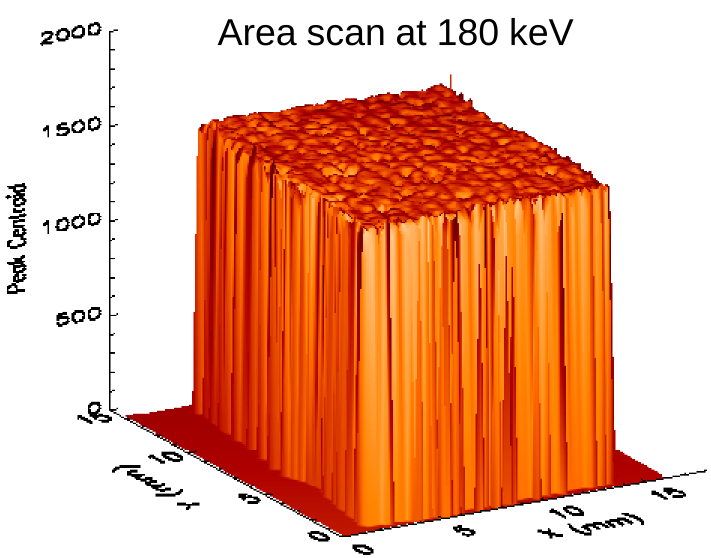

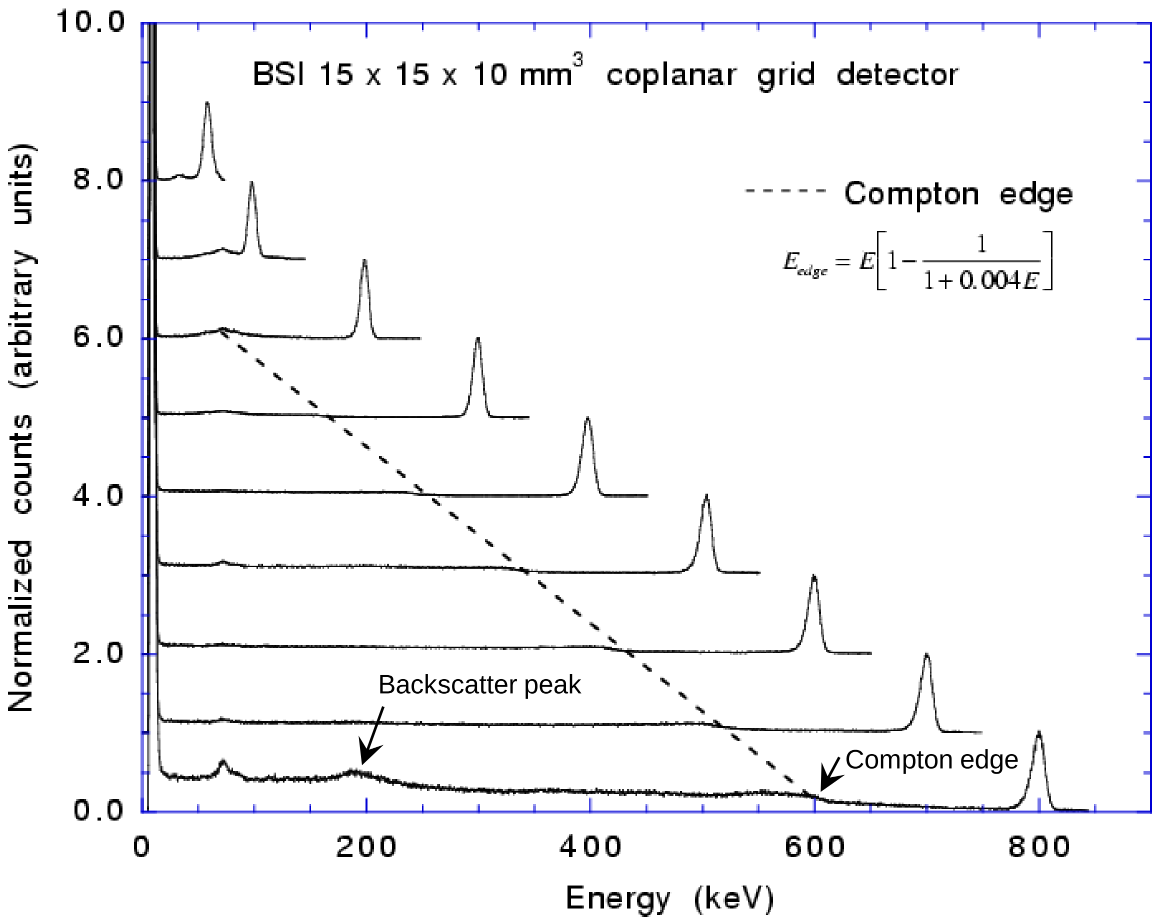

Examples - basic detector characterization

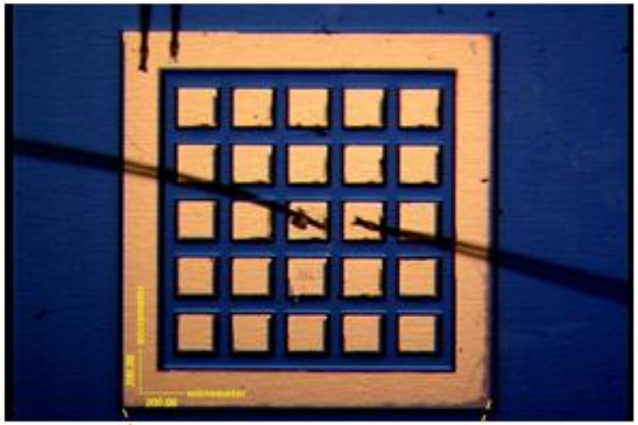

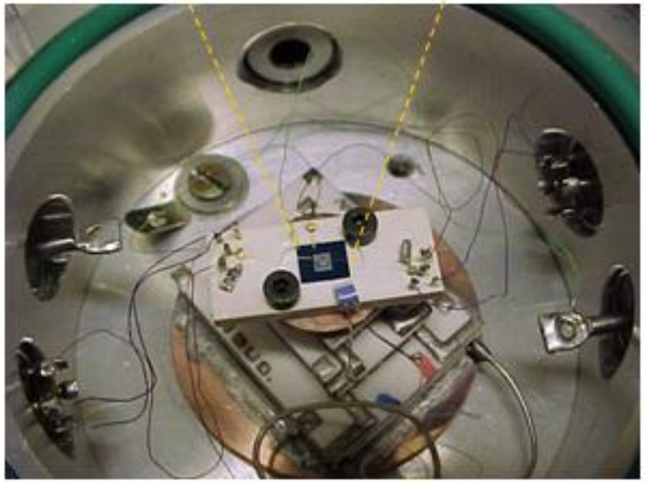

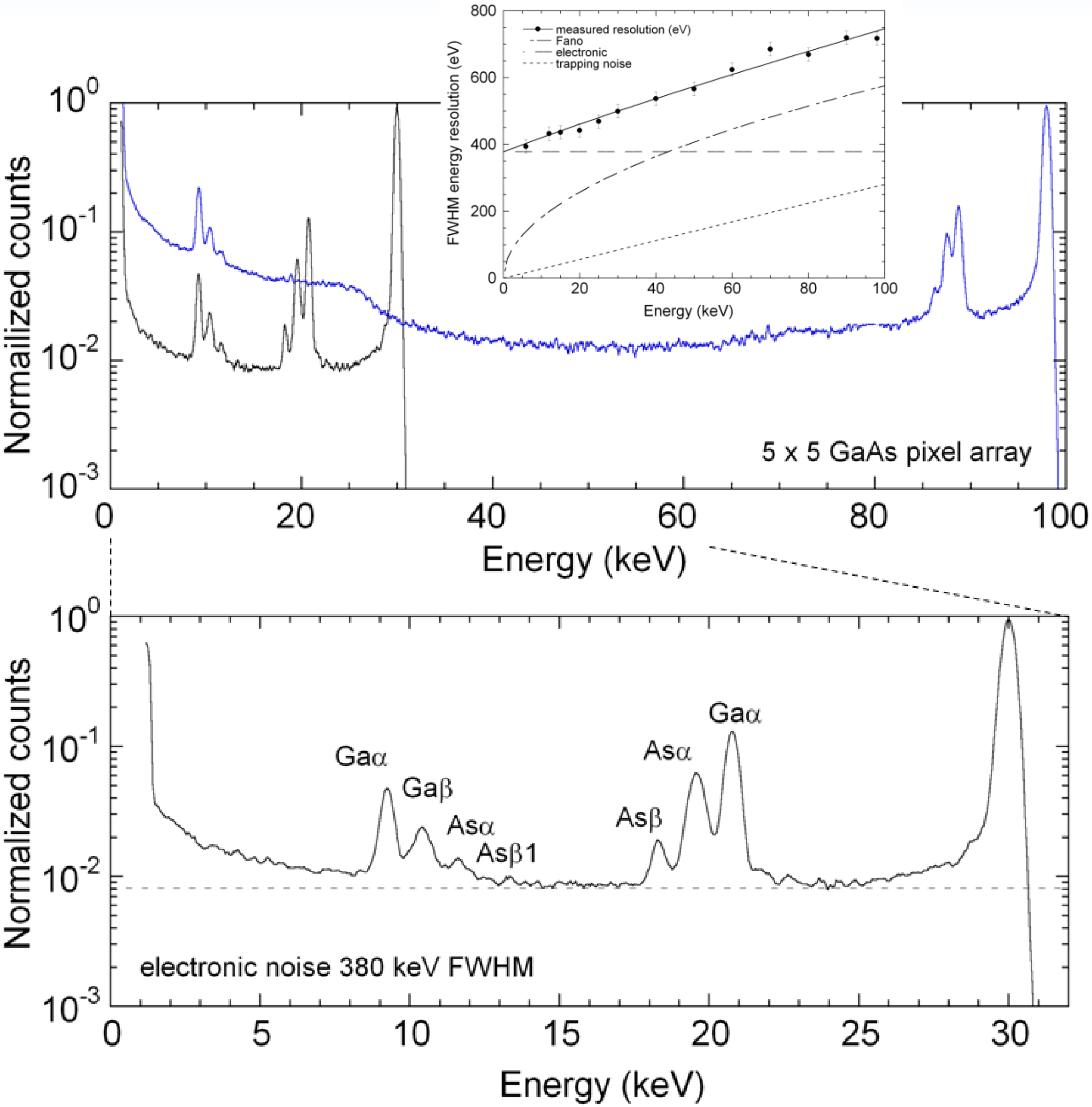

SiC detector – low energy response

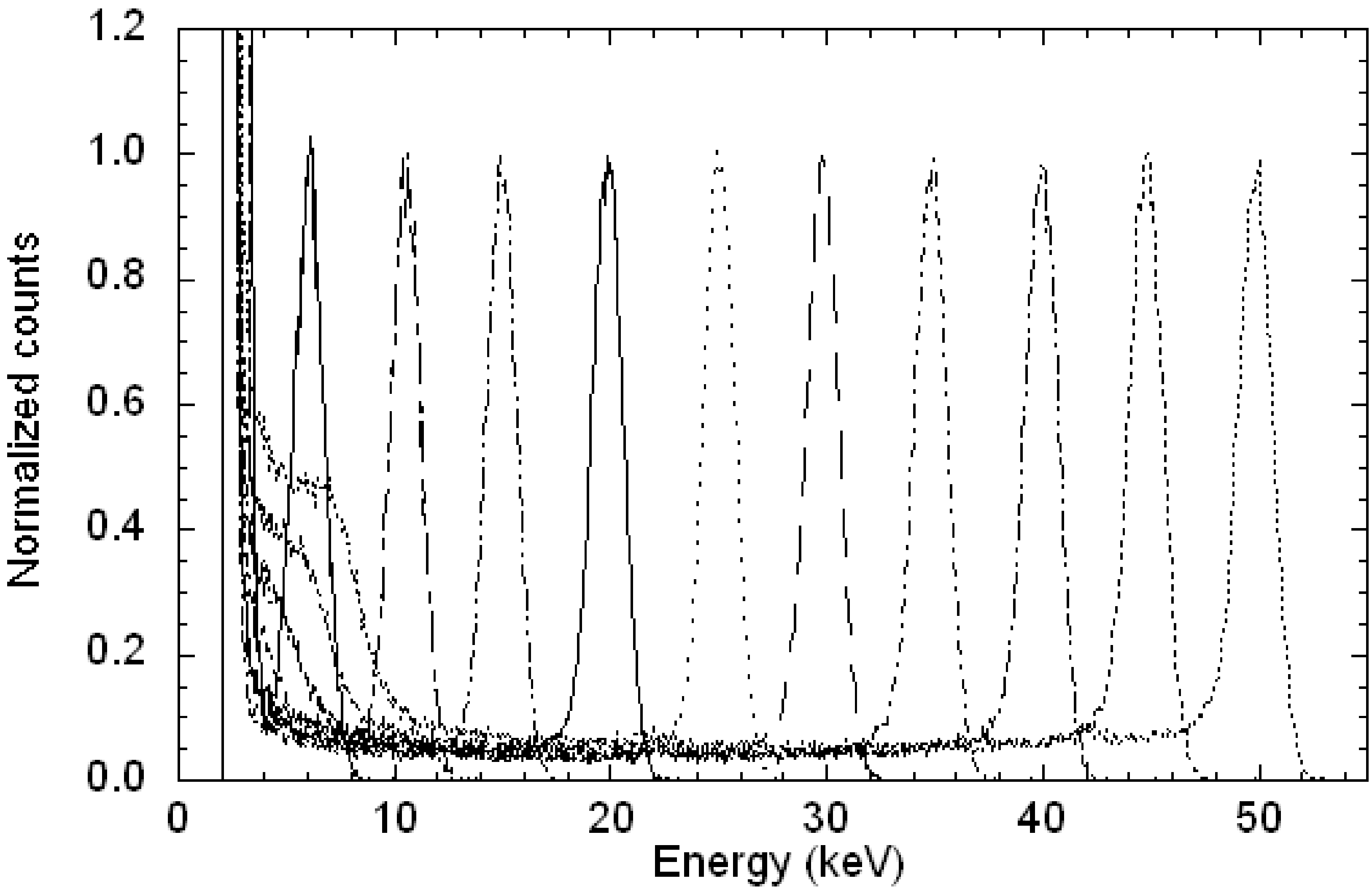

SiC array development

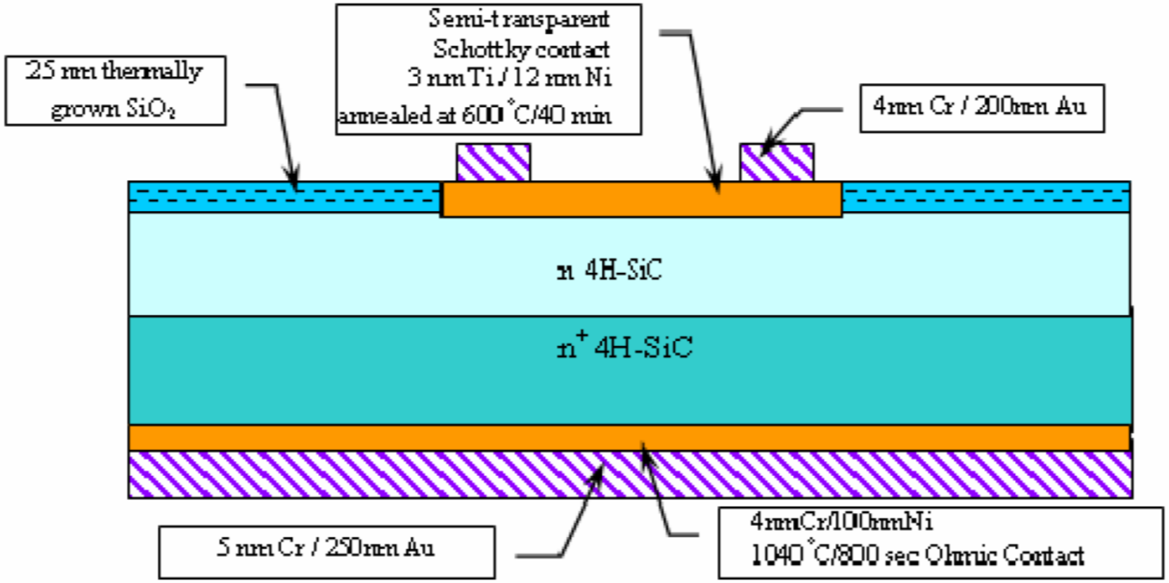

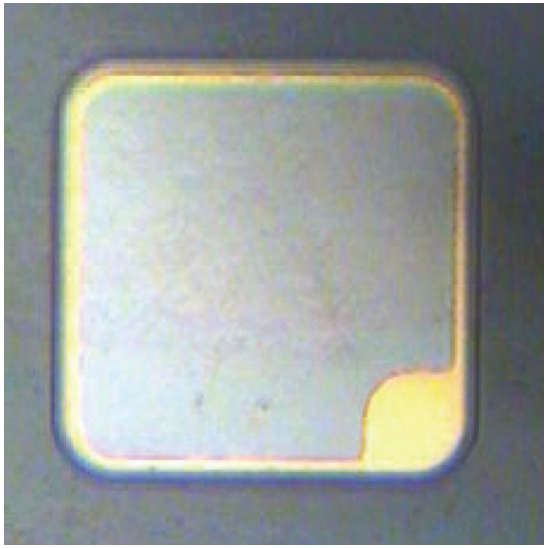

diode construction

SiC detector – high energy response

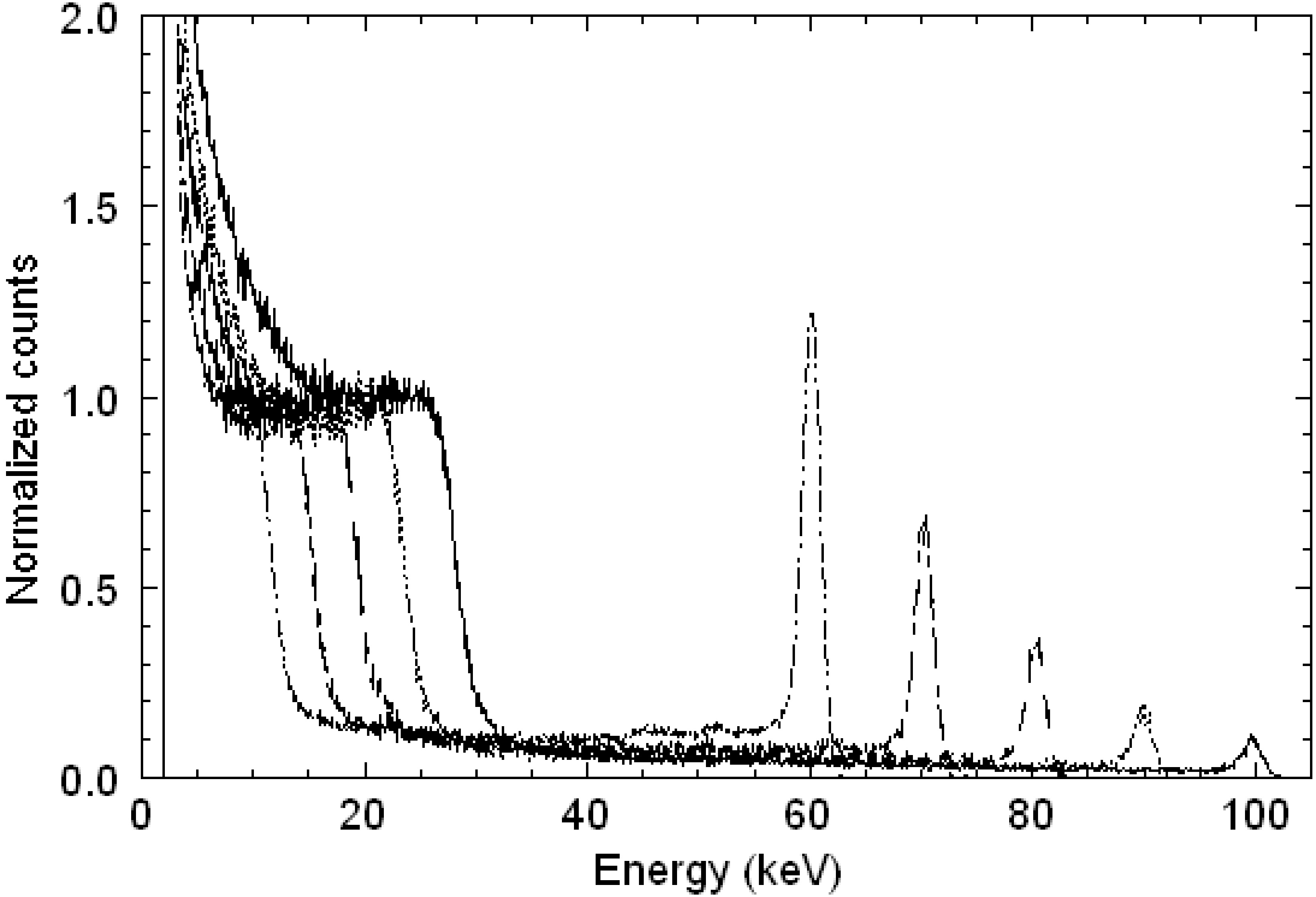

Count rate distribution at 12 keV – quick look

10 x 10 μm² beam, 10 μm steps

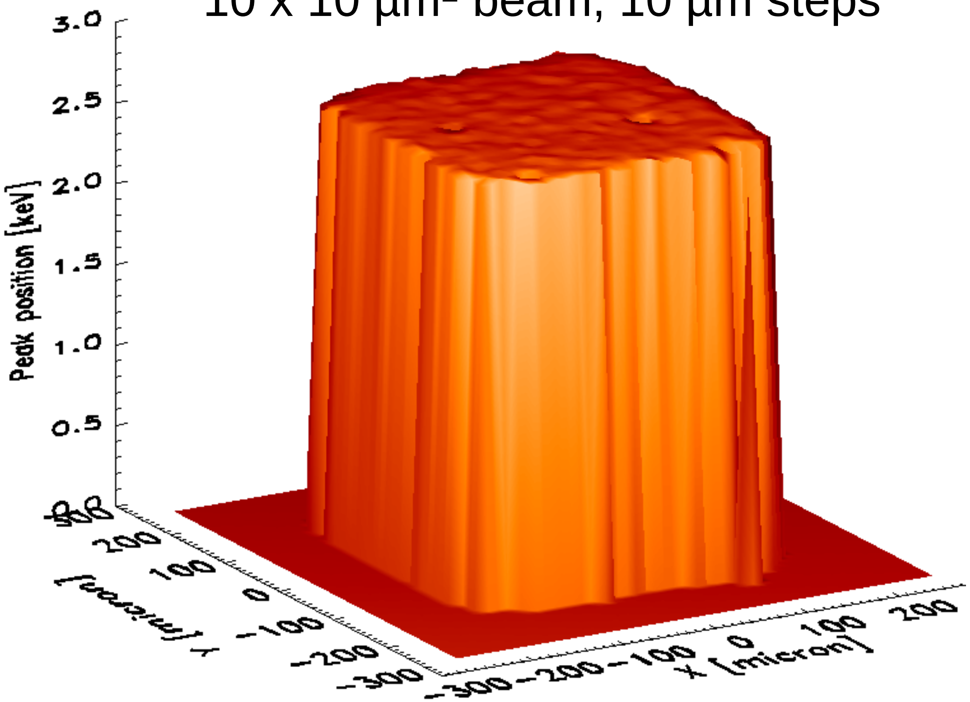

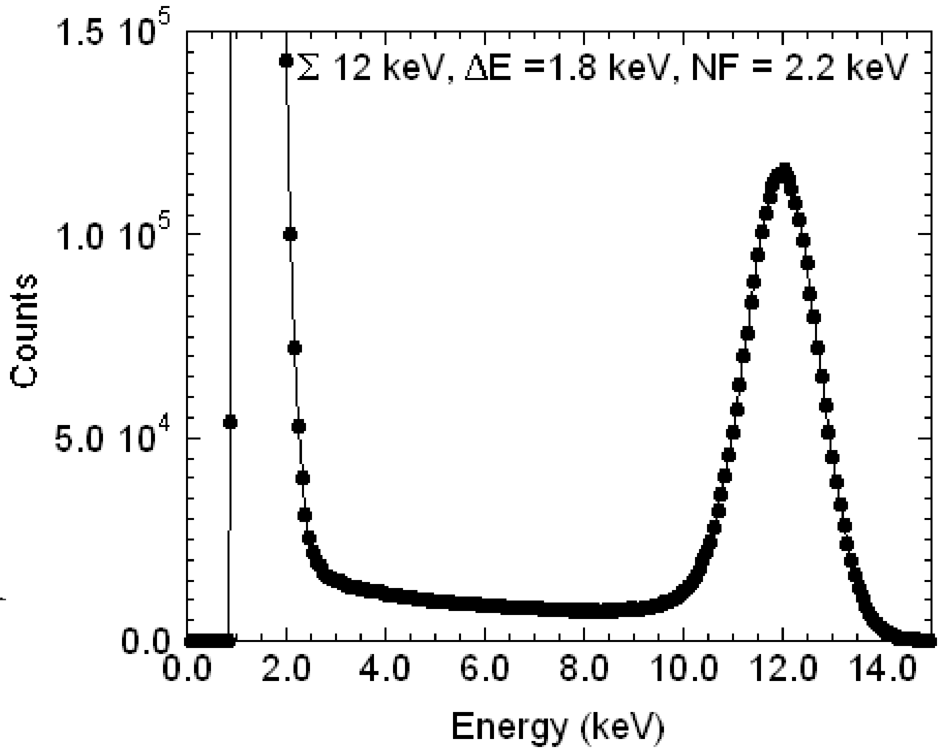

Single point resolution 1.7 keV

BESSY II SiC efficiency measurements 12th Dec 2006

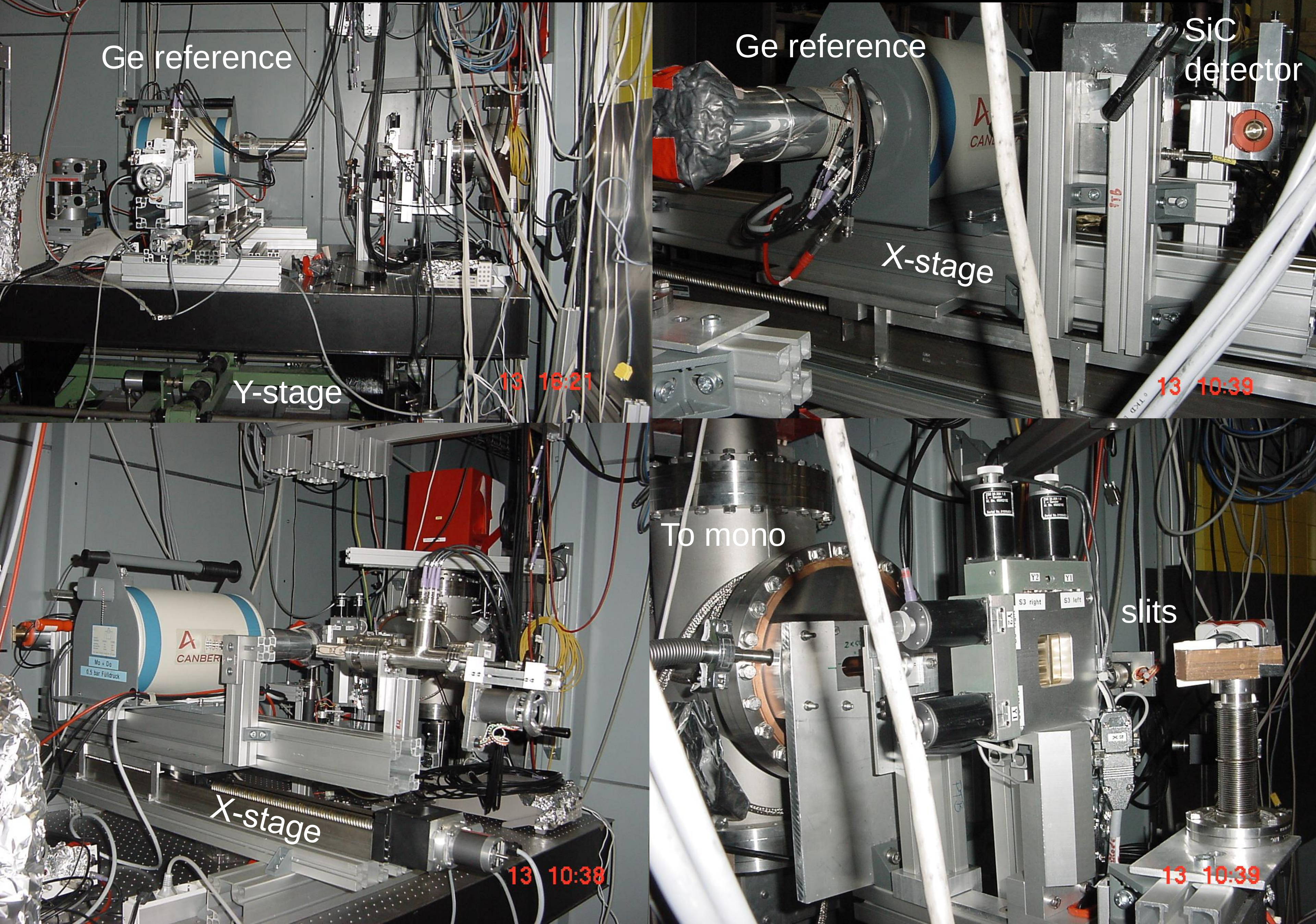

Efficiency and depletion depth determination

(data corrected for dead layers, air path, window thickness and dead time)

(harmonics can be used)

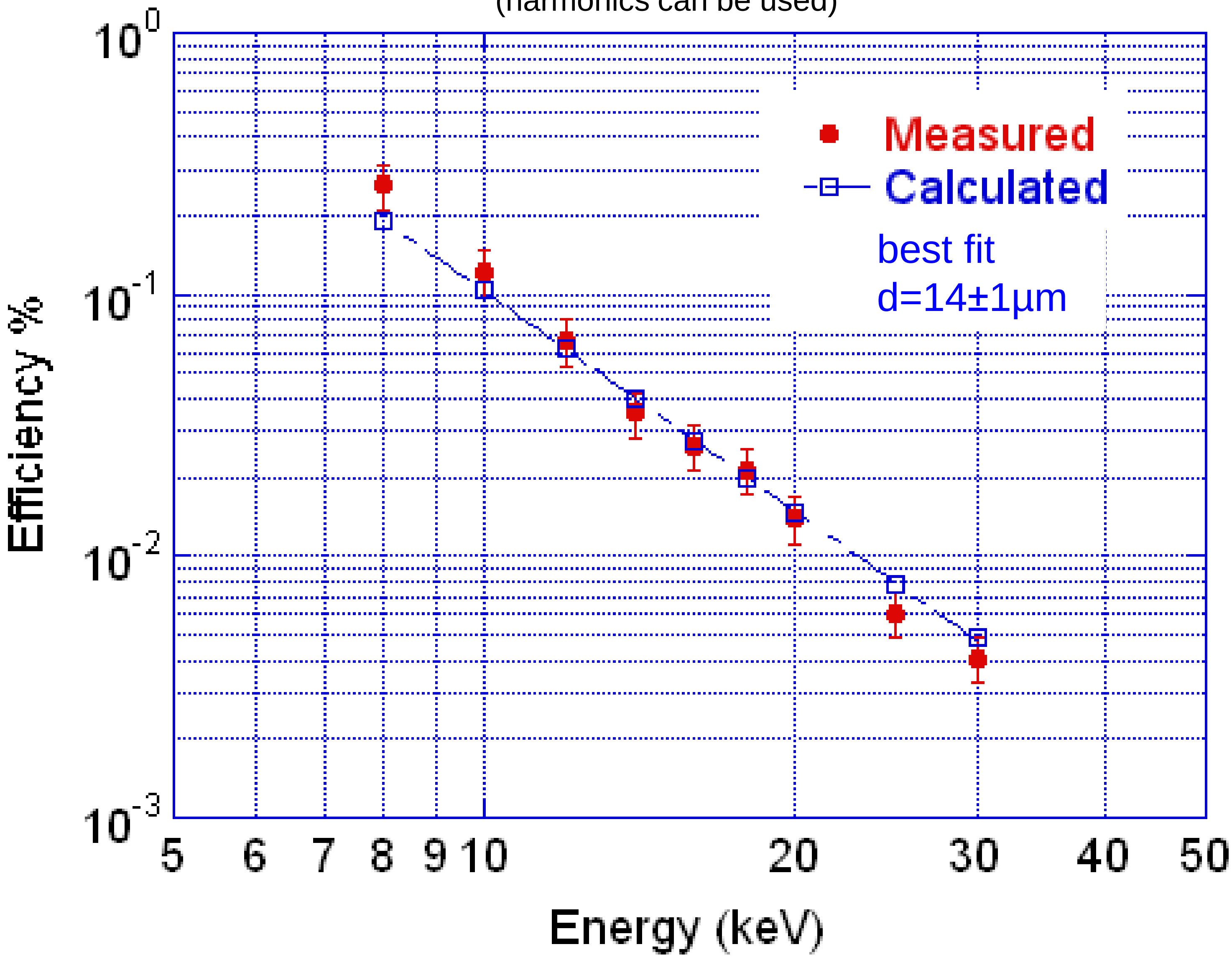

Pump and probe techniques

Investigation of polarization effects in compound semiconductors

Defined as a time dependent variation in the detectors properties, such as count rate, charge collection and resolving power. Seems to be correlated with

- material properties (purity, stoichiometry)
- temperature
- high resistivity
- dielectric constant
- Correlated with the total energy deposition per unit time
- Particularly acute in groups II-VI and I-VII compounds (TlBr, CdTe, CdZnTe, HgI_2)

Its treatment has been largely anecdotal and qualitative.

Recently, a 1 D semiempirical model was proposed by Bale and Szeles, Phys. Rev. B **77**, 035205 (2008) in which polarization was presumed to be caused by deep hole trapping

Based on "pump and probe" measurements Kozerezov et al have developed a full 3 D analytical model of polarization (Kozorezov et al. "*Polarization effects in thallium bromide x-ray detectors*", J. Appl. Phys., **108** (2010) 064507)

Polarization in TlBr X-ray detectors

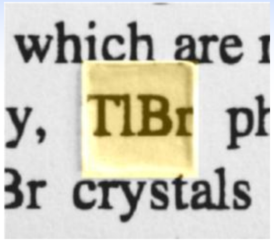

2.8 x 2.8 .x 1 mm^3 TlBr planar detector
Au contacts
V_b=840V
T=-30-+23^{o}C

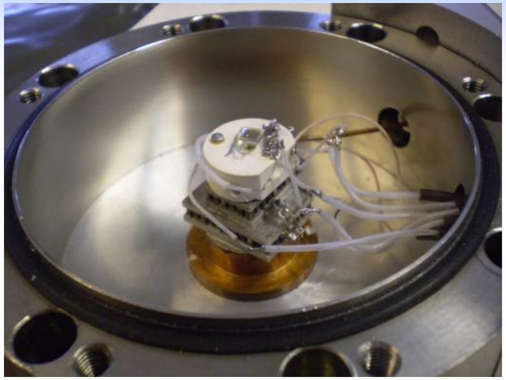

Polarization effect in TlBr

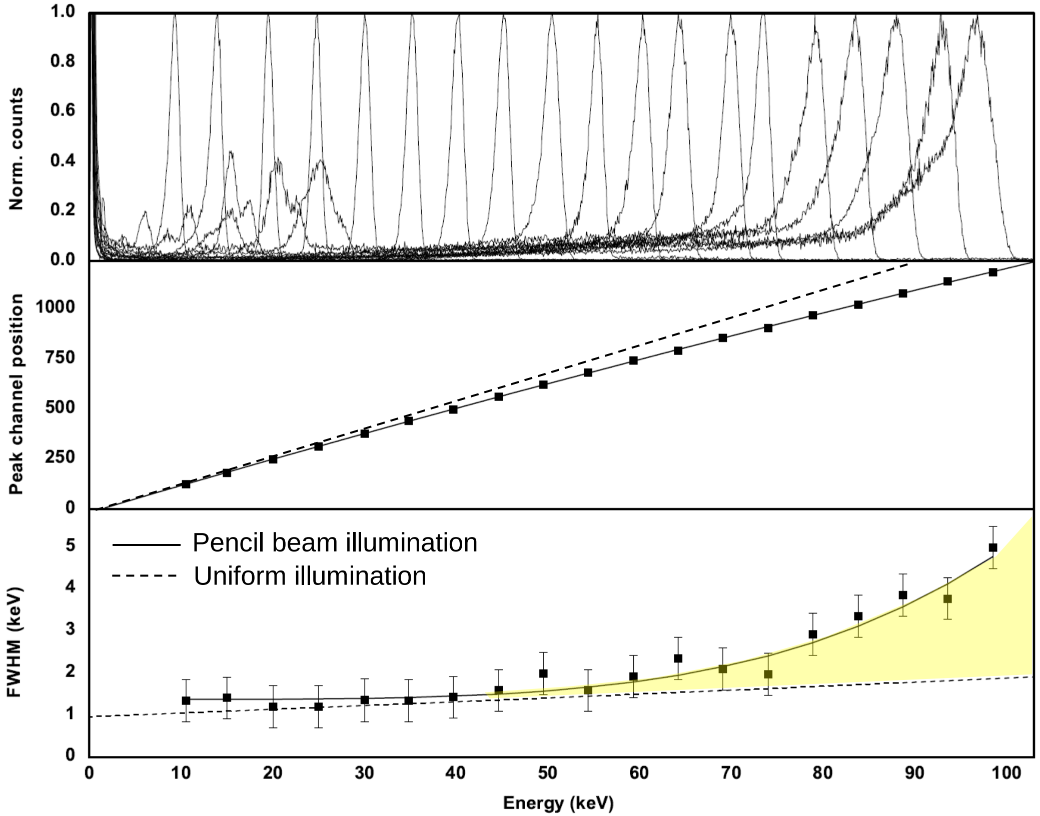

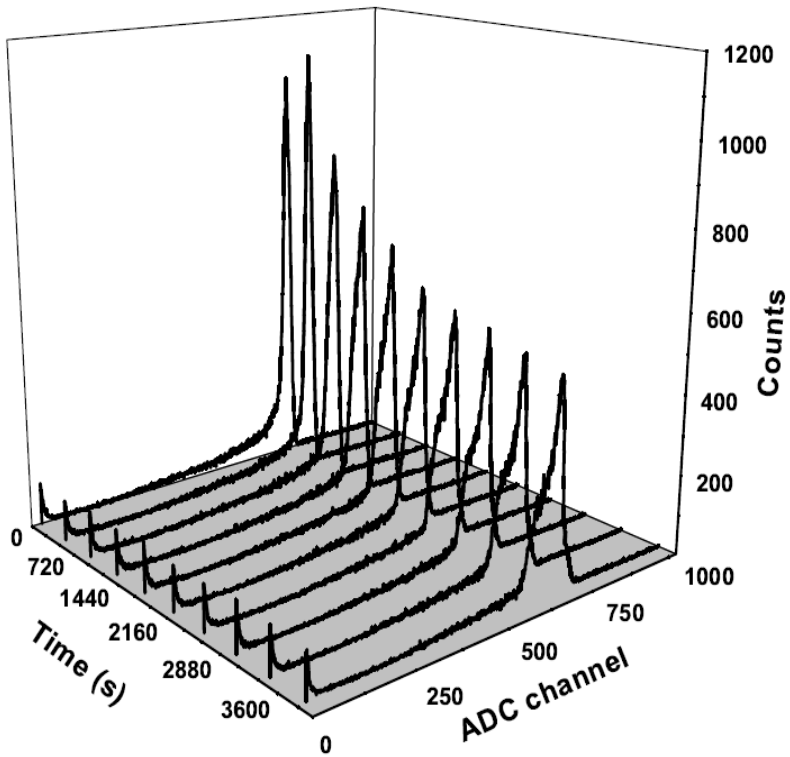

Left: composite energy loss spectra covering the energy range 10-100 keV. Right: a series of “snapshots” of the 60 keV lineshape with exposure time under a constant illumination of 10^3 photons s^{-1}.

The pump and probe technique

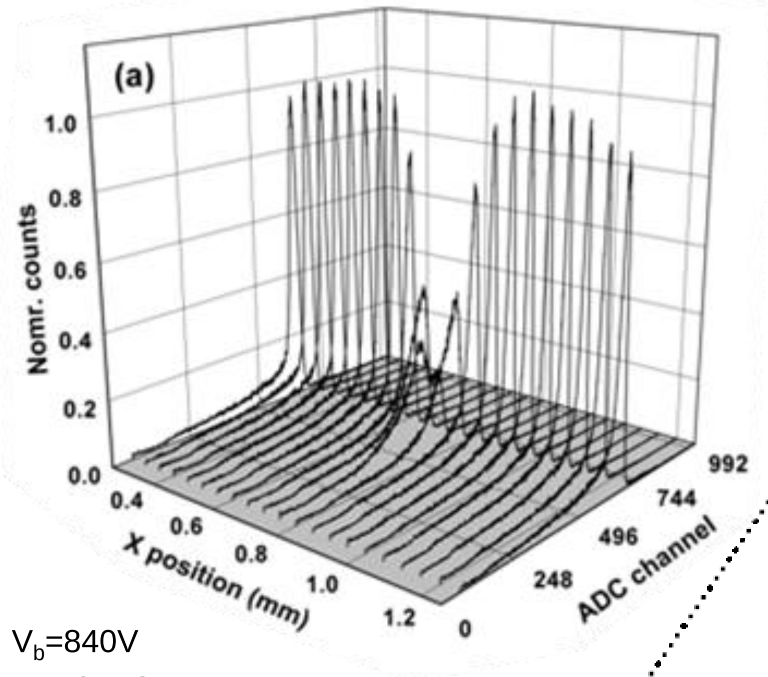

V_b=840V
T=-25°C

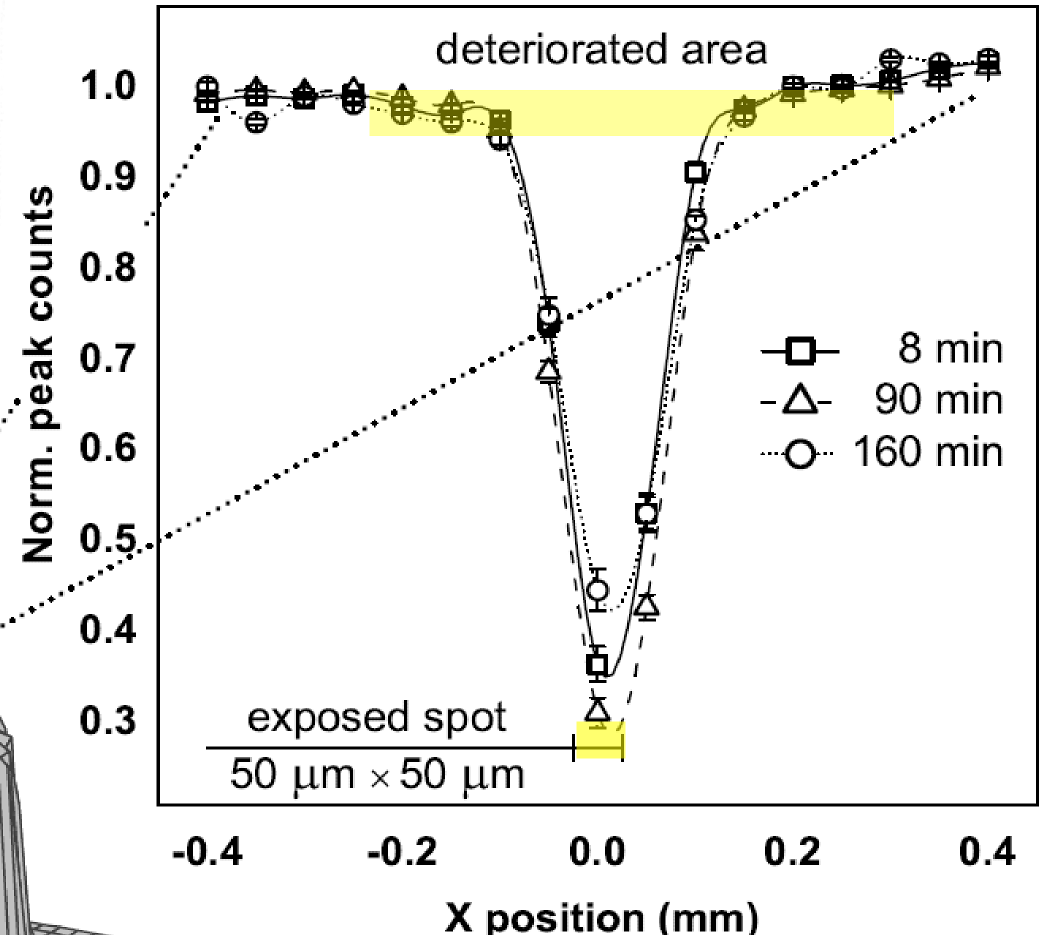

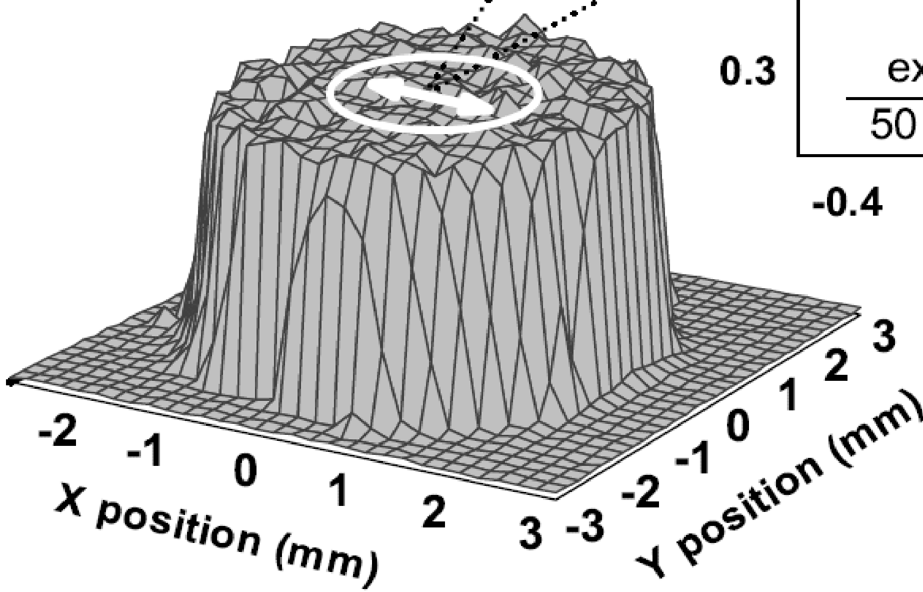

Pump with 2x10^6 60 keV photons at (0,0) with a 50 x 50 µm^2 spot

Probe ± 0.5 mm across pump spot using 60 keV beam (10^3 photons per step)

Repeat as a function of bias and temperature

Evolution of peak parameters

60 keV pump and probe

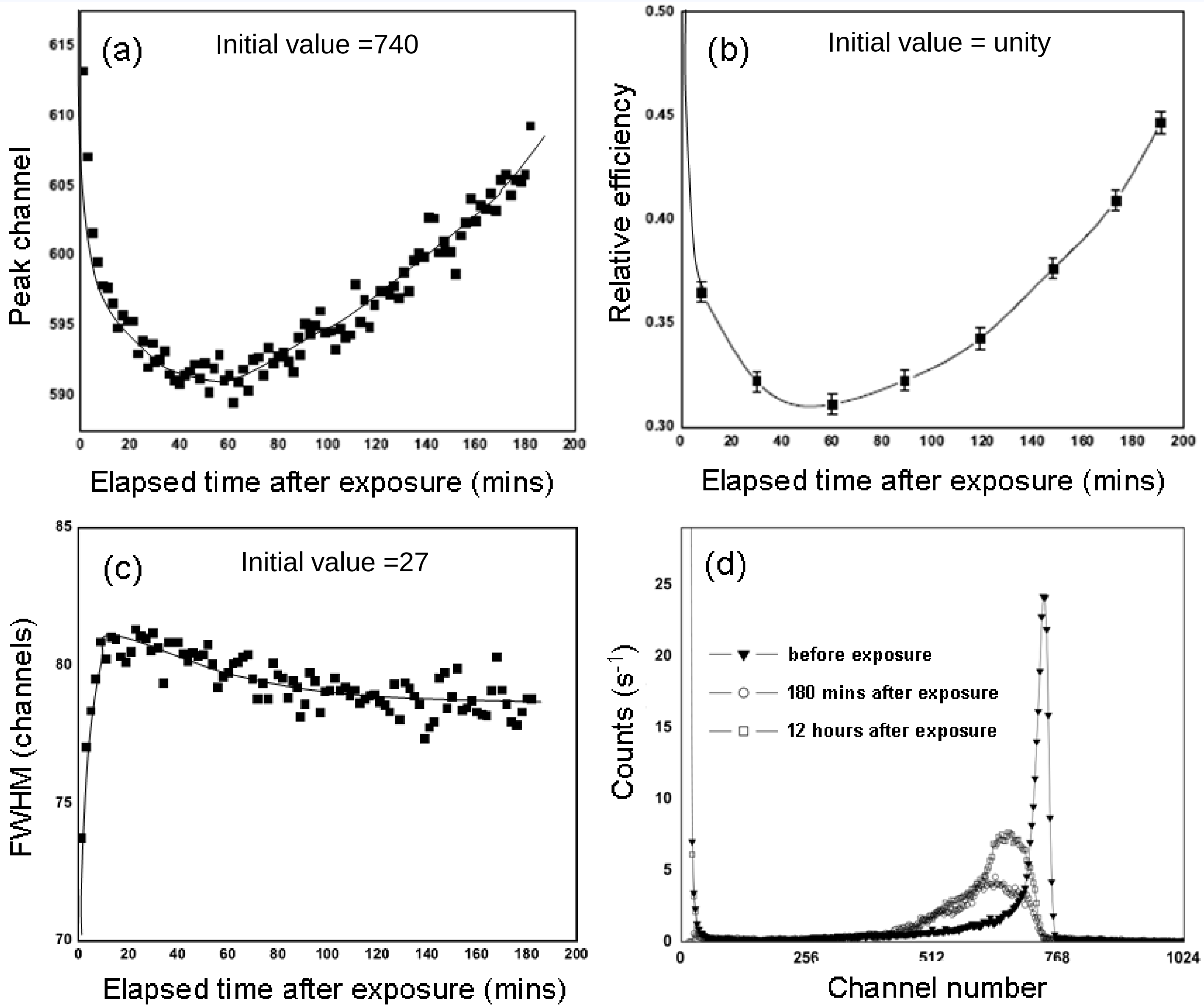

Potential profile

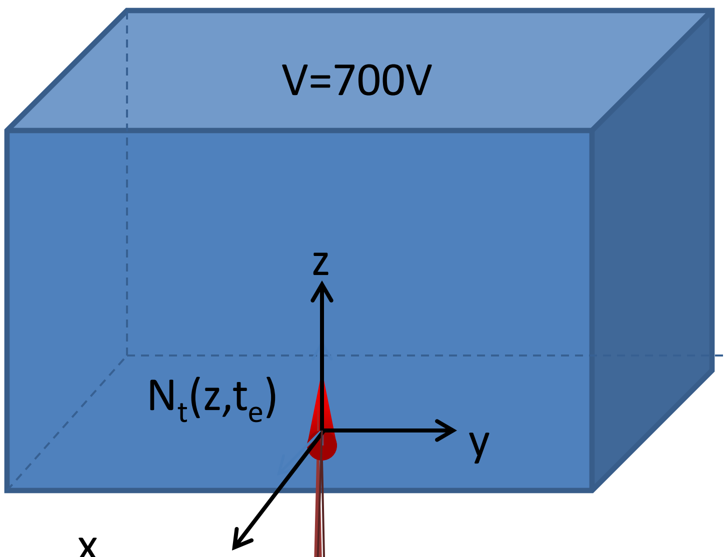

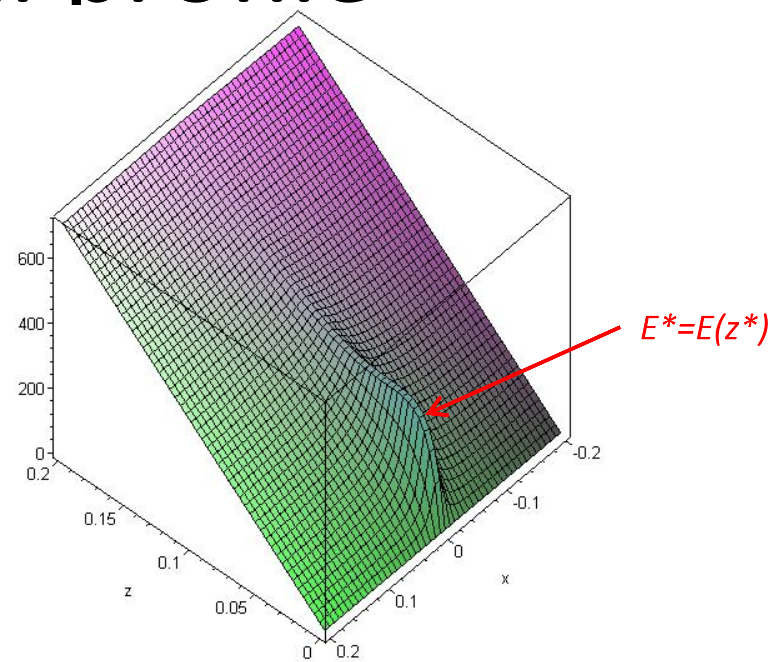

$$\Phi(\mathbf{x},t) = V\frac{z}{L} + \frac{4\pi e}{\varepsilon}\int\int\int \mathrm{d}\mathbf{x}' p_t(\mathbf{x}',t) \sum_{n=-\infty}^{+\infty}\left[\frac{1}{|\mathbf{r}-\mathbf{r}'+\mathbf{k}(z-z'+2nL)|} - \frac{1}{|\mathbf{r}-\mathbf{r}'+\mathbf{k}(z+z'+2nL)|}\right]$$

$$\frac{\partial p_t}{\partial t} = \frac{p}{\tau_h}\left(1-\frac{p_t}{p_t^0}\right) - \gamma p_t - R_t n p_t$$

$$p_t(\mathbf{x},t) = \int_0^t \frac{\mathrm{d}t'}{\tau_h} p(\mathbf{x},t')\exp\left[-\int_{t'}^t \mathrm{d}t''\left(\gamma' + \frac{p(\mathbf{x},t'')}{p_t^0\tau_h}\right)\right]$$

$$\int_{r<R} \mathrm{d}\mathbf{r}\, p(\mathbf{r},z=0)E_z(\mathbf{r},z=0) = \frac{I_0}{\mu_h E_{eh}}\frac{\pi d^2}{4}$$

RTSD R16-3

Simulation of line-shape

$$Q = Q(\mathbf{x}_a) = -eN_0 \exp\left(-\frac{t^*(\mathbf{x}_a)}{\tau_e}\right) - eN_0 \int_0^\infty \mathrm{d}t' \left[\frac{1}{\tau_e} \exp\left(-\frac{t'(\mathbf{x}_a)}{\tau_e}\right) \frac{z_e(t',\mathbf{x}_a)}{L} - \frac{1}{\tau_h} \exp\left(-\frac{t'(\mathbf{x}_a)}{\tau_h}\right) \frac{z_h(t',\mathbf{x}_a)}{L} \right]$$

$$S(\mathbf{x}_a, Q) = \frac{1}{\sqrt{2\pi}\sigma(\mathbf{x}_a)} \exp\left[-\frac{(Q - Q(\mathbf{x}_a))^2}{2\sigma^2(\mathbf{x}_a)}\right]$$

$$S(Q) = \int_0^L \mathrm{d}z P_s(z, E) S(z, \mathbf{r}_a, Q)$$

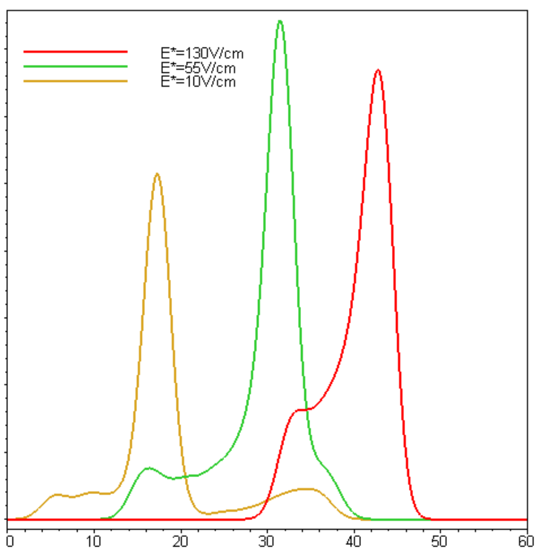

Line shapes near the pinch point

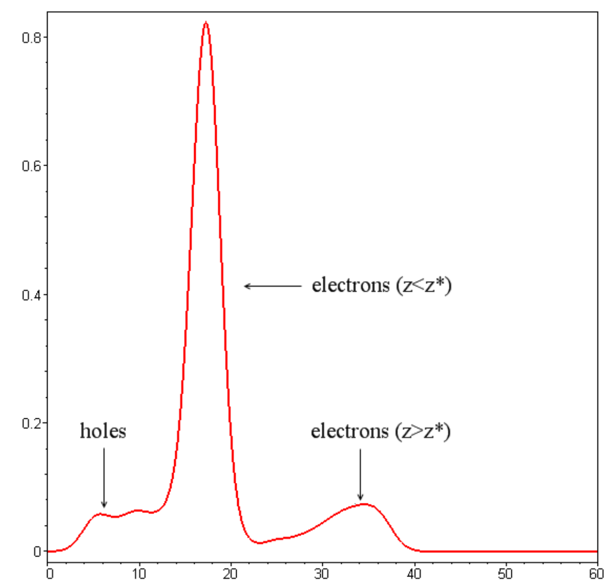

Preliminary polarization results

Observations

- The spatial extent of the polarized region is much larger that the initial pump region.
- In TlBr and CdZnTe, the overall lineshape is very sensitive to the hole $\mu\tau$ product
- While peak channel and CCE, recovery on time scales of hours, spectral resolution and particularly the line shape recover on time scales of days.

Conclusions

- The pump and probe technique is an ideal technique to investigate dynamic processes and their evolution.
- The primary cause of polarization effects is due to the charging of deep traps by one of the carriers.
- The build-up of space charge perturbs of the internal electric field affecting the collection of the other carrier.
- At the "pinch" point the induced field due to the space charge is equal to the applied field resulting in a catastrophic loss of performance
- De-polarization proceeds through thermal recombination and cannot be effectively achieved through modulation of the bias voltage as previously thought.

Next steps – use 3D analytical model to derive hole mu-tau products, trap densities, occupancy rates and ionization energies $\rightarrow$Identify the particular trap(s) involved.

Defect metrology

Crystal defects - primer

Twins – grain boundary defect, in which a crystal is joined to its mirror image – size up to ~ ~mm

Dislocation – line defect that may run the length of the crystal – size up to ~mm

Grain boundaries – Boundary between two crystals in a polycrystalline solid size up to ~ ~mm

Voids – macroscopic holes in the lattice - size up to ~mm

Inclusions – regions of a different phase, size 1-10’s of micron

Precipitates – small regions of a different phase, size up to ~micron

Macroscopic defects

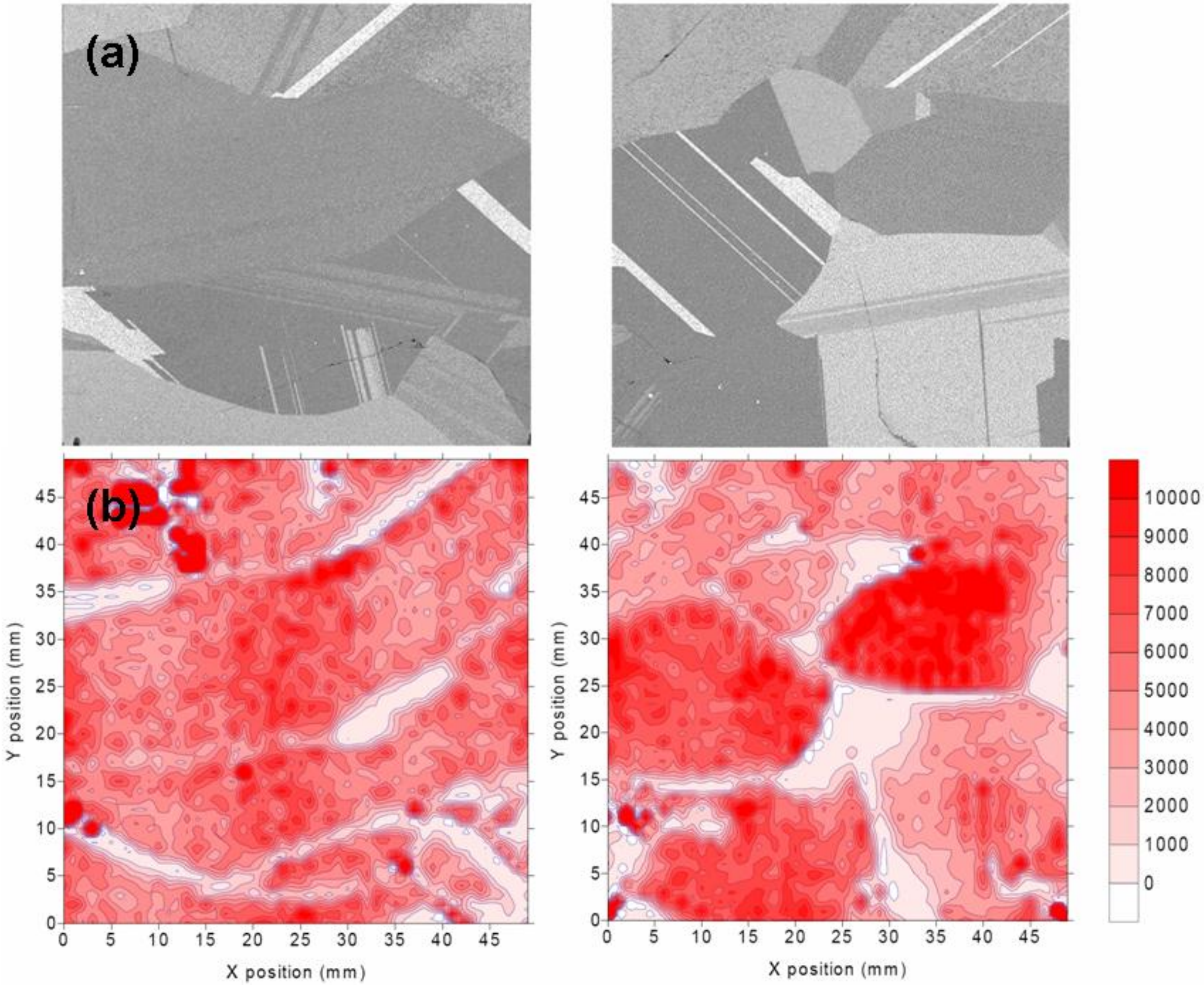

a) Optical images of two 50 × 50 mm^2, 3 mm thick slices of a CdZnTe crystal grown by the High Pressure Bridgman method. Numerous grain boundaries and twins are apparent in the image. *b*) The crystals count rate response, measured with a ^{57}Co radioactive source is shown in the lower images, illustrating poor charge collection at the grain boundaries.

 C. Szeles, M.C. Driver, *"Growth and properties of semi-insulating CdZnTe for radiation detector applications"*, Proc. of the SPIE, **3446** (1998) 2

Coplanar grid
CZT crystal
imperfections

ESRF
beamline ID15

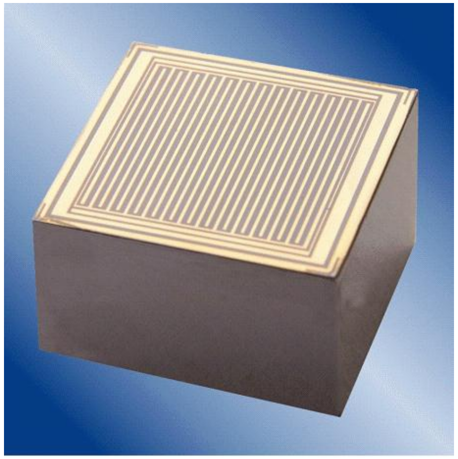

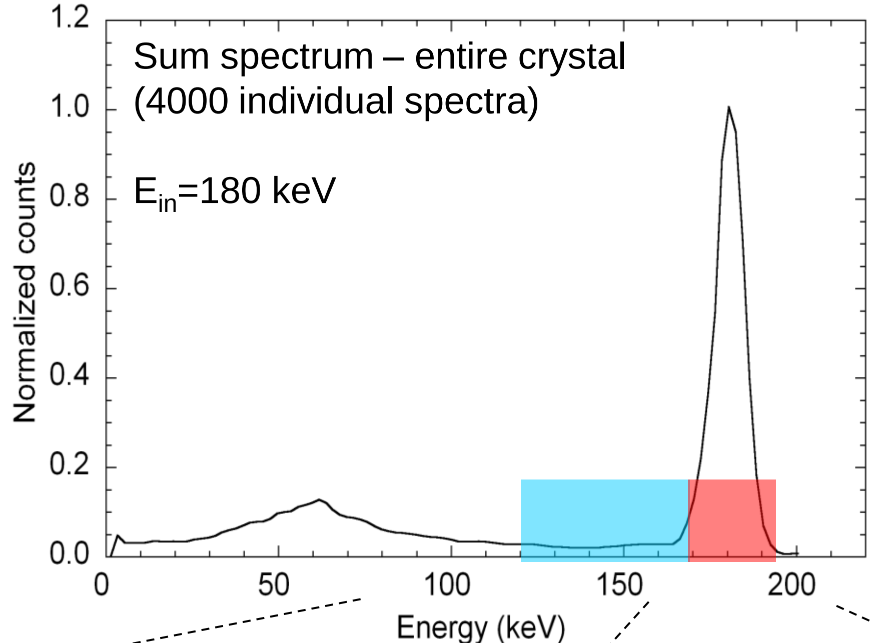

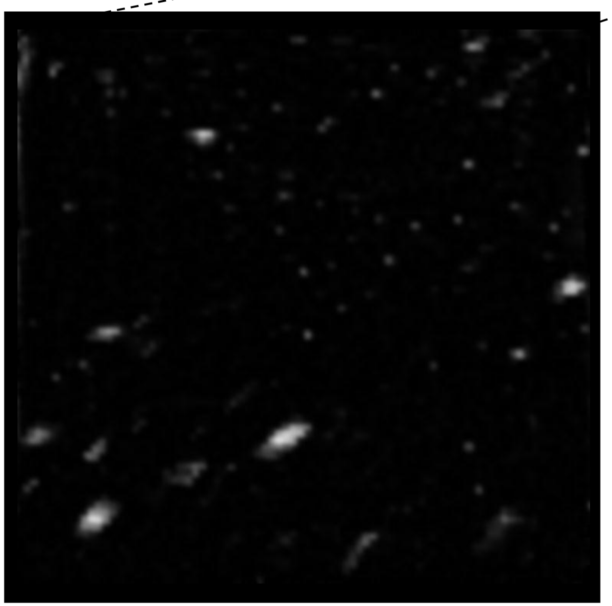

Counts between 120-170 keV

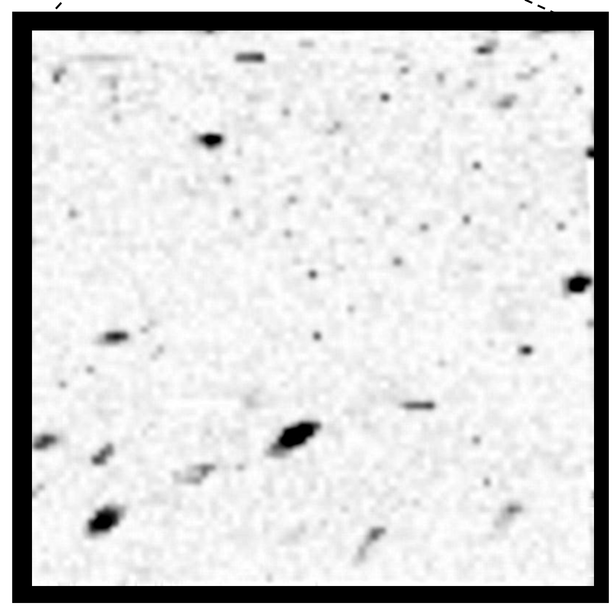

Counts between 170-193 keV

Crystal defects

The X-ray world with finer spatial resolution

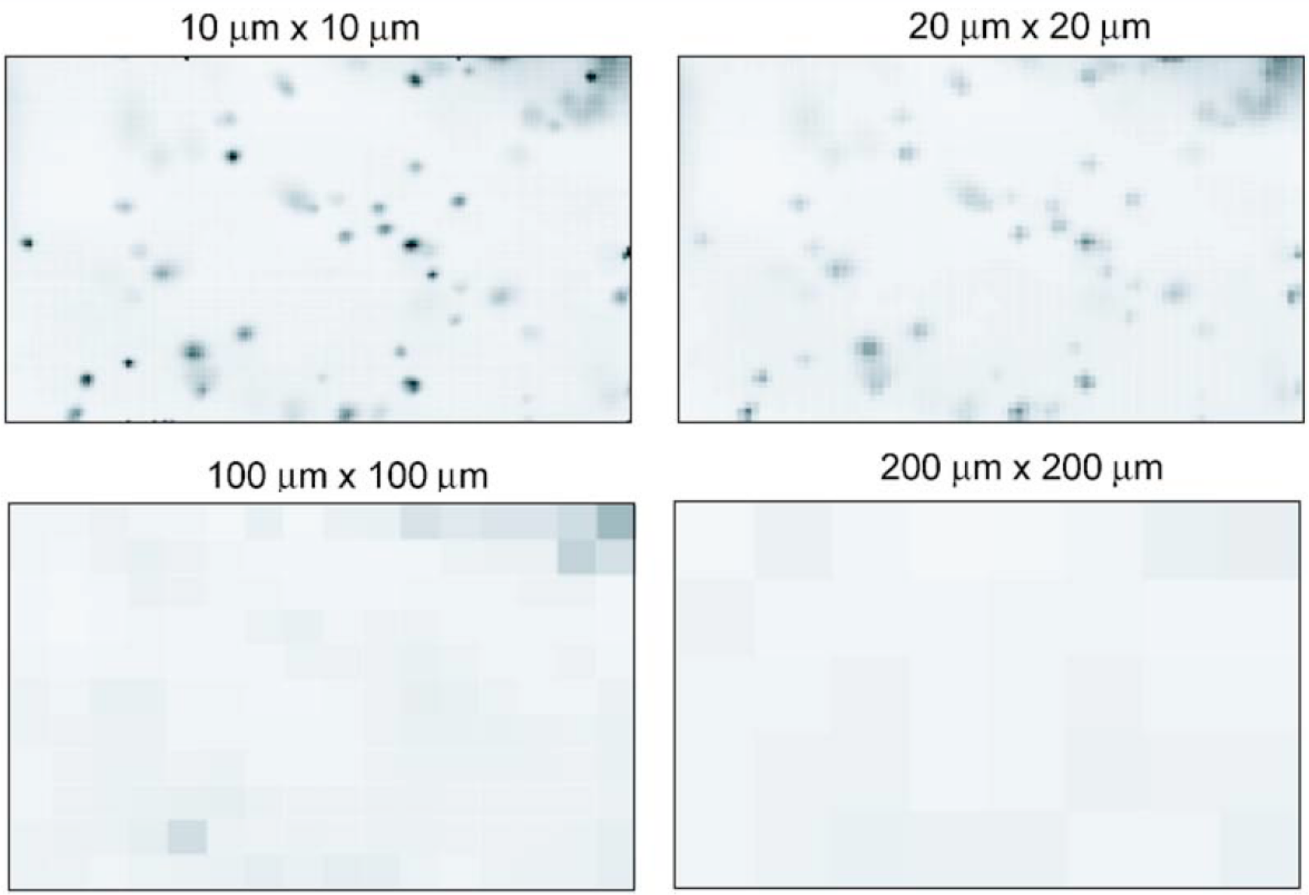

FIG. 4. (Color online) X-ray maps evaluated for the same area of the device, but with different spatial resolutions: 10×10, 20×20, 100×100, and $200\times200\ \mu m^2$.

Carini, et al., "*Effect of Te precipitates on the performance of CdZnTe (CZT) detectors*," Appl. Phys. Lett., **88** (2006) 143515-1

Crystal defects

Finer spatial resolution

IR micrographs

X-ray images

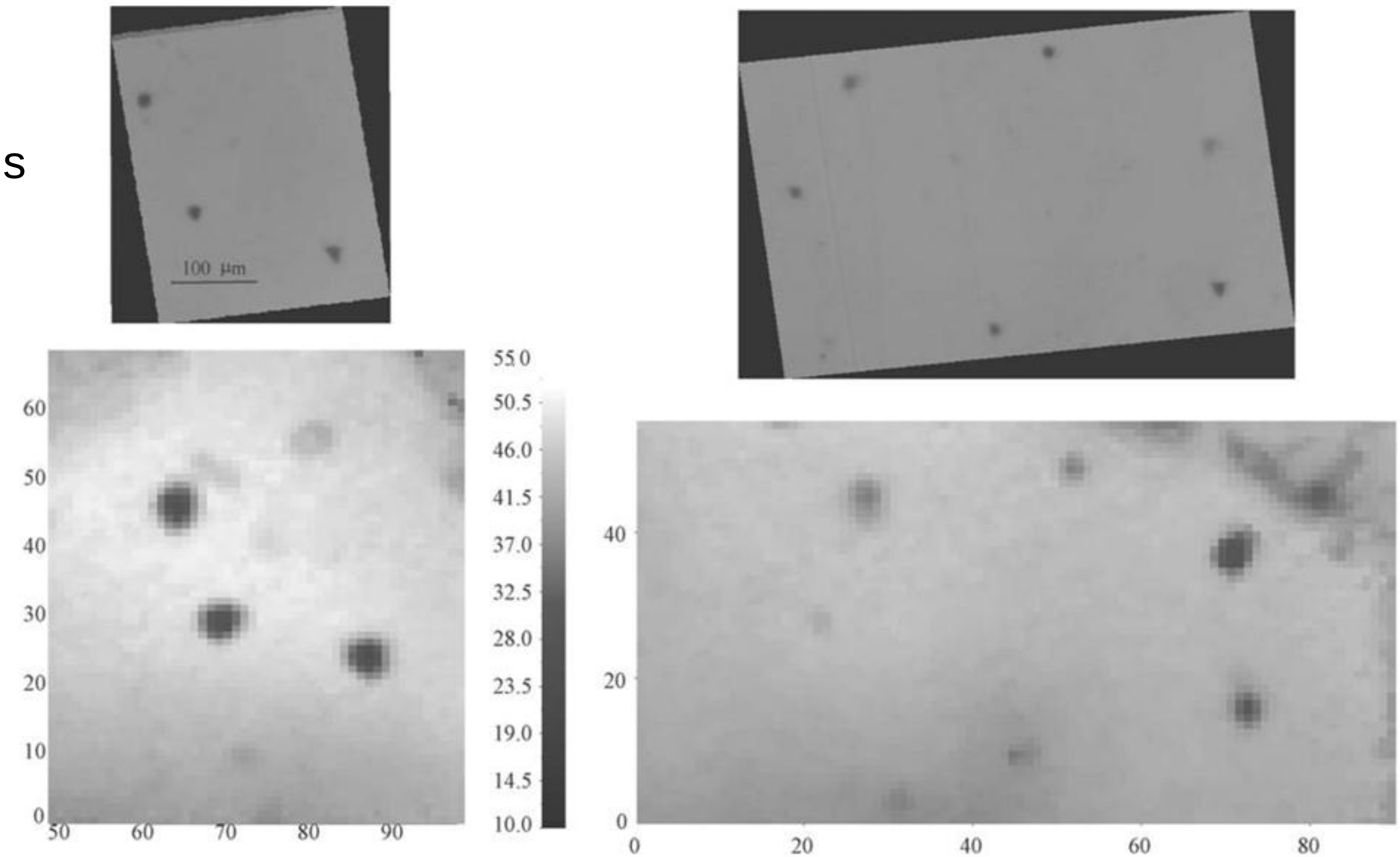

IR and X-ray mages of Te inclusions/precipitates measured in a 1-mm thick CZT crystal. The lower images are X-ray maps when of the crystal when operated as a simple planar detector. The dark spots in this case correspond to a drop in the detector response, demonstrating the link between precipitates and poor device performance. The scans were performed by using a 10×10 μm^2, 85 keV X-ray beam.

Carini, et al., "*Effect of Te precipitates on the performance of CdZnTe (CZT) detectors*," Appl. Phys. Lett., **88** (2006) 143515-1

IR transmission microscopy

IR system allows us to take "in-depth" images of Te inclusions and collapse them on a single plane. We can do a 3-D reconstruction of images. We can also measure sizes and concentration of Te inclusions.

Example of the crystal with high concentration of Te inclusions.
1.1x1.5x10 mm^3

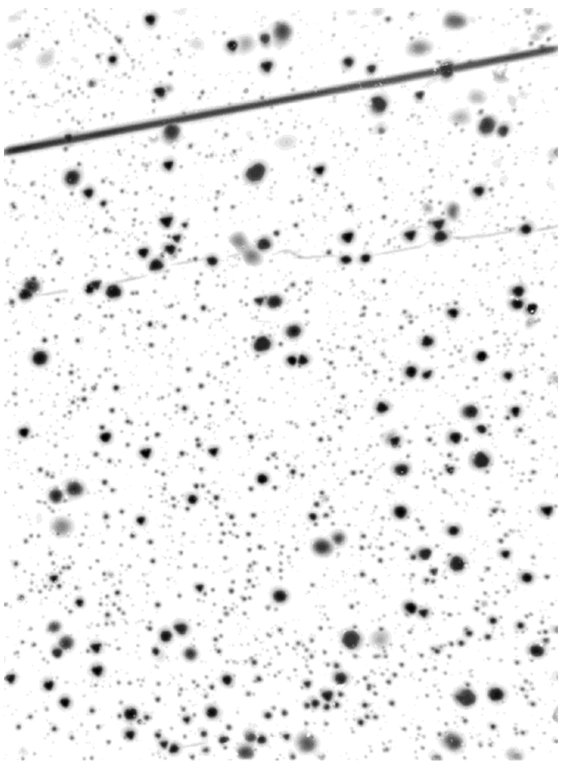

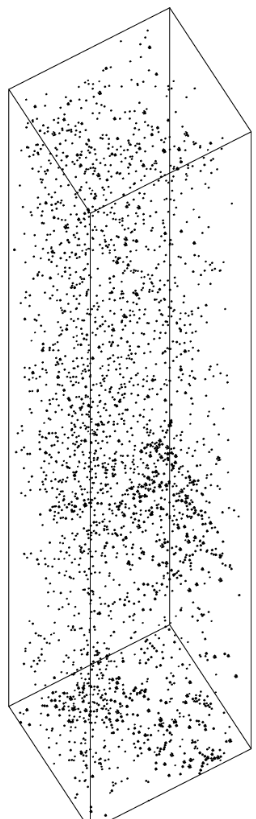

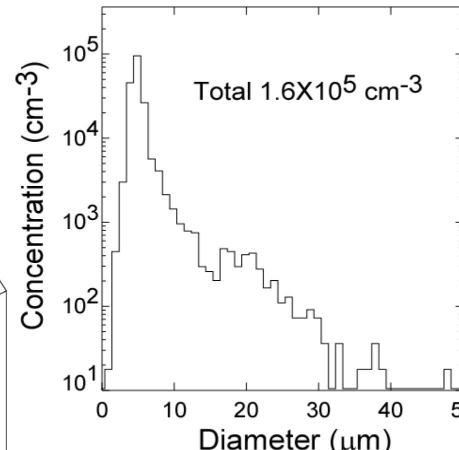

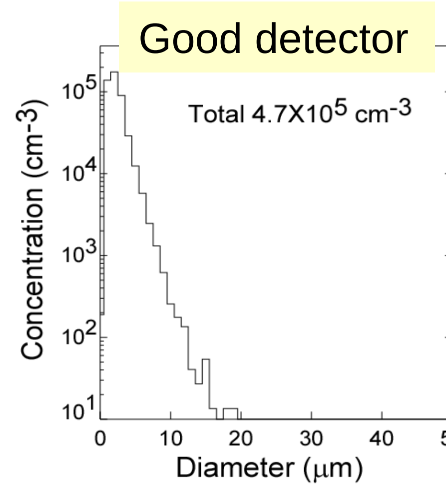

For each inclusion we measure x,y,z, and diameter.

Plug data into the model to generate X-ray response maps and pulse-height spectra.

Currently, our model assumes that Te inclusions are opaque to carriers. It depends on a single adjustable parameter: the ratio between effective and actual size of inclusion.

Bolotnikov et al., *Extended Defects in CdZnTe Radiation Detectors*, IEEE Trans Nucl. Sci, 56 (2009) 1775.

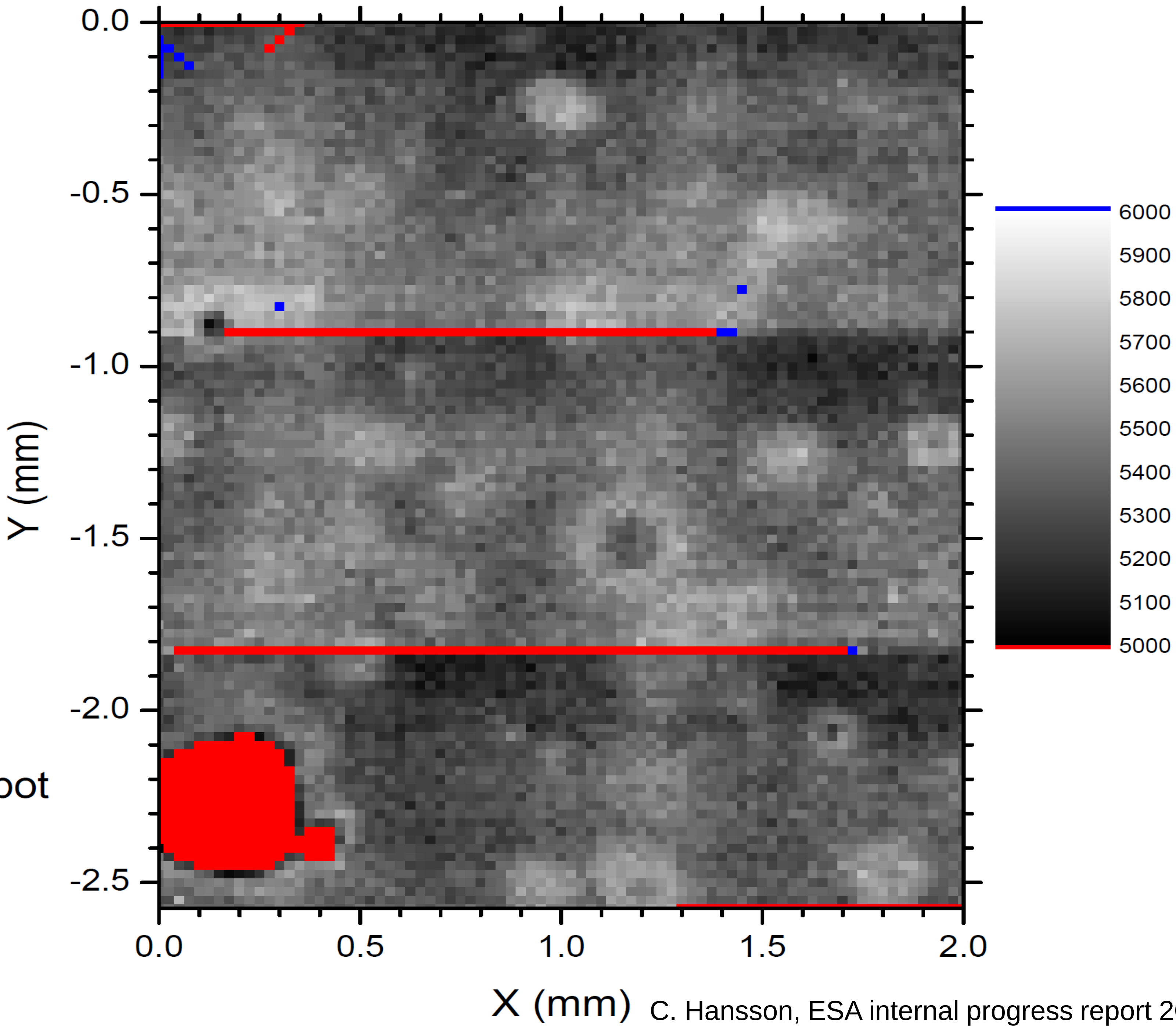

First spot
X=0
Y=-2.2

C. Hansson, ESA internal progress report 2011

Small area/ high resolution scans – R Large

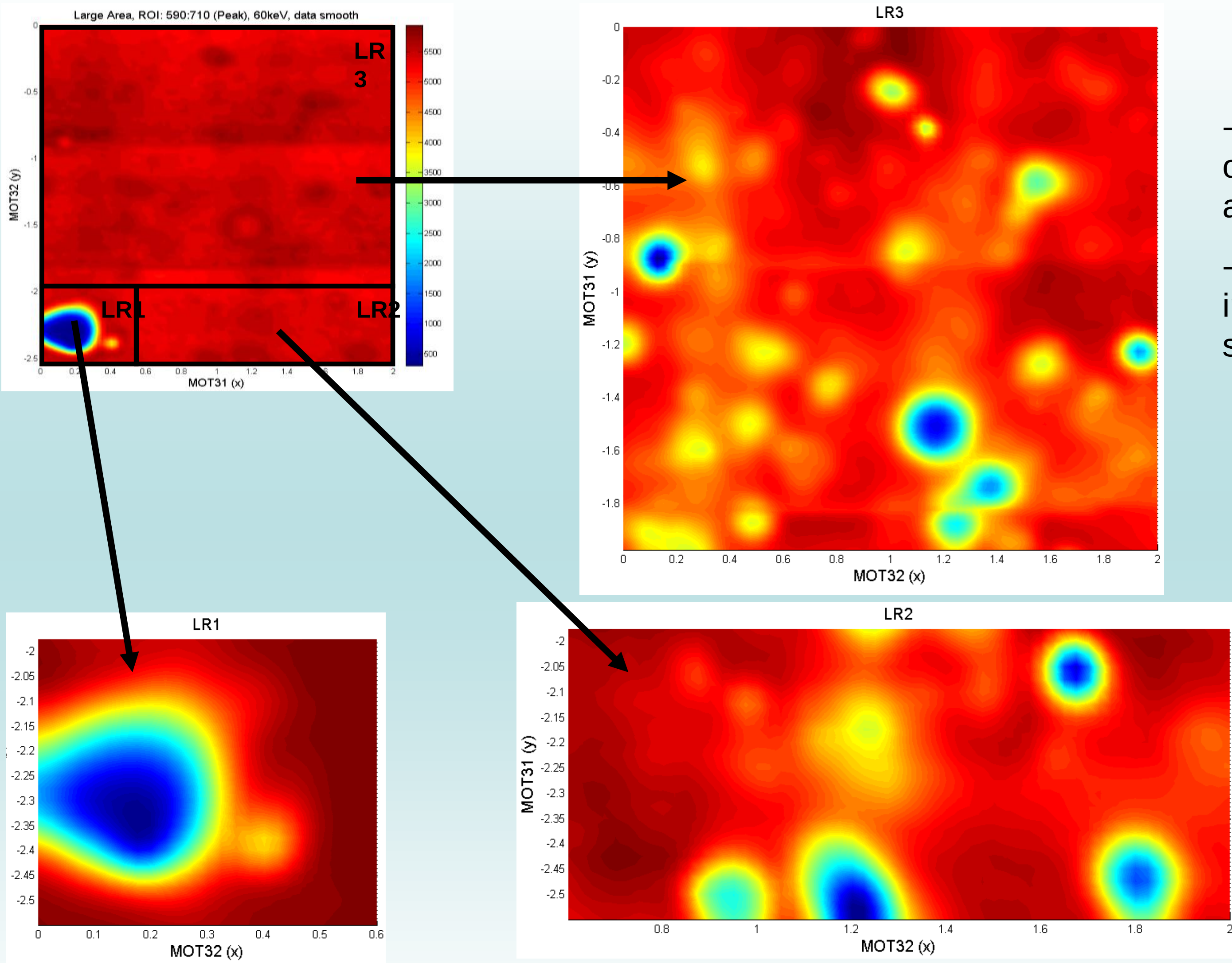

- 24 inclusions were observed in region LR2 (5) and LR3 (19)
- 18 inclusions were investigated with respect to spectral response.

see poster by Hansson

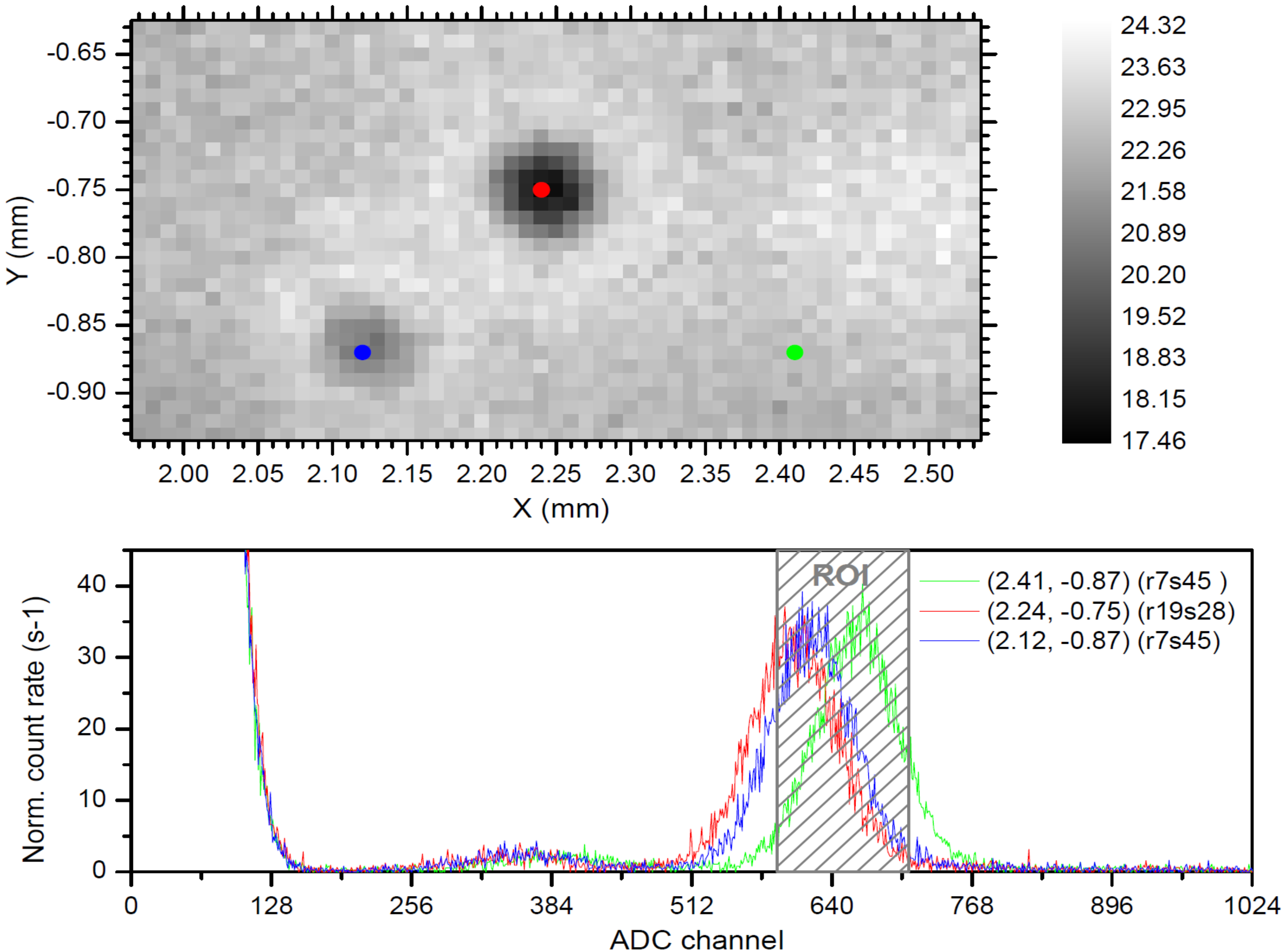

Basic spectral response (60keV)

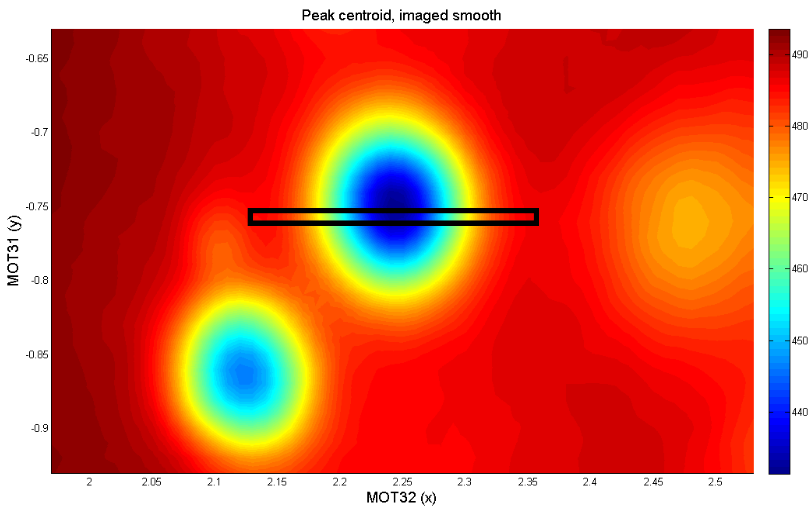

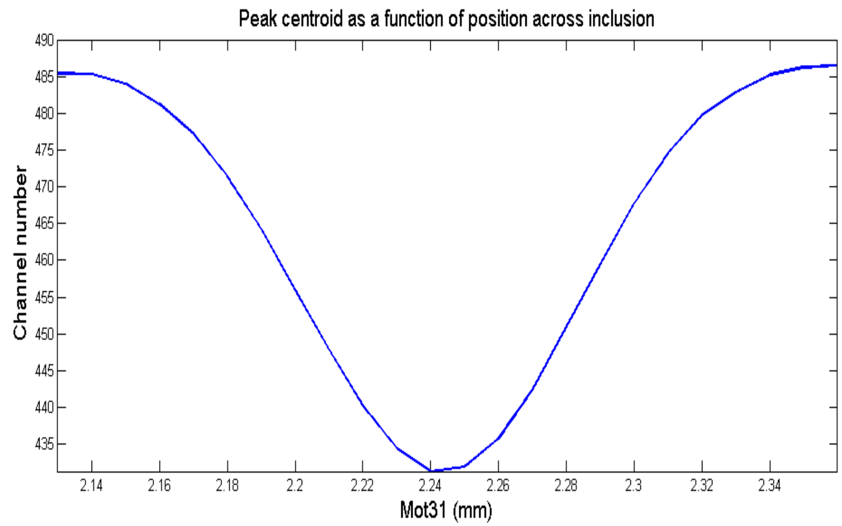

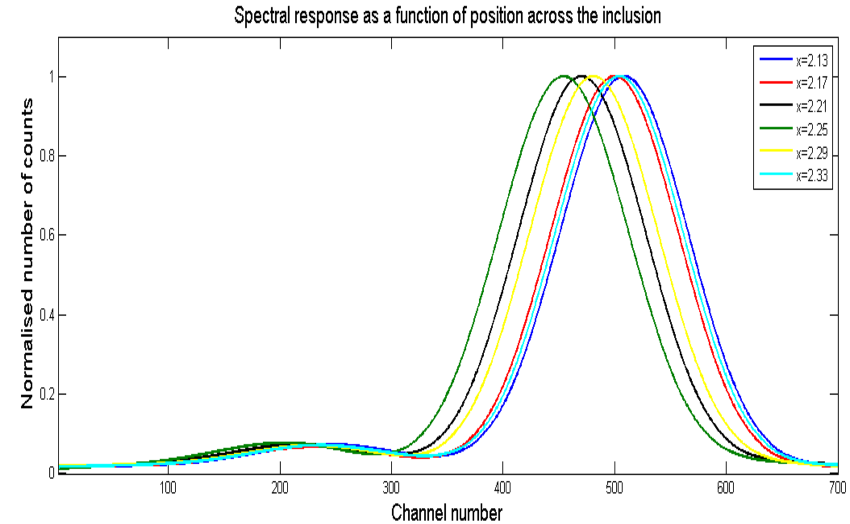

The basic response when monitoring the spectral evolution across the inclusion was a reduction in peak centroid up to the centre and a recovery when moving out of the inclusion.

R2 inclusion 1

Summary & conclusions

X-ray mapping using synchrotron radiation provides a very powerful technique to investigate crystal defects

- Inclusion/precipitates acquire a space charge and modify the local electric field
- Measured spectrum within an inclusion shifts to lower energies
- Counting efficiency and FWHM of the photopeak remain largely unchanged, however
- CCE's are reduced by ~10%
- Double peak structure seen at high energies (depths)
- No correlation between peakshift and inclusion size
- Near field devices could act as X-ray microscopes
- Next steps: await input from UL

  X-ray measurements with CVD material (MTPVT) – expect only voids

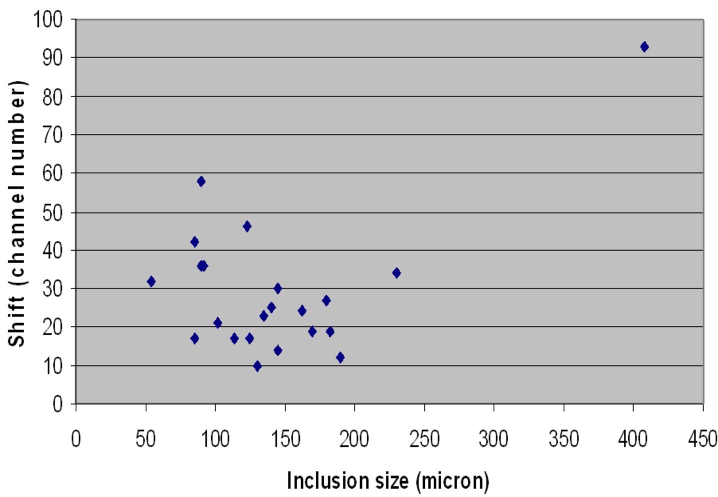

Scintillator studies - non-proportionality

1 inch right circular crystals coupled to XP2060B 10-stage PMTs

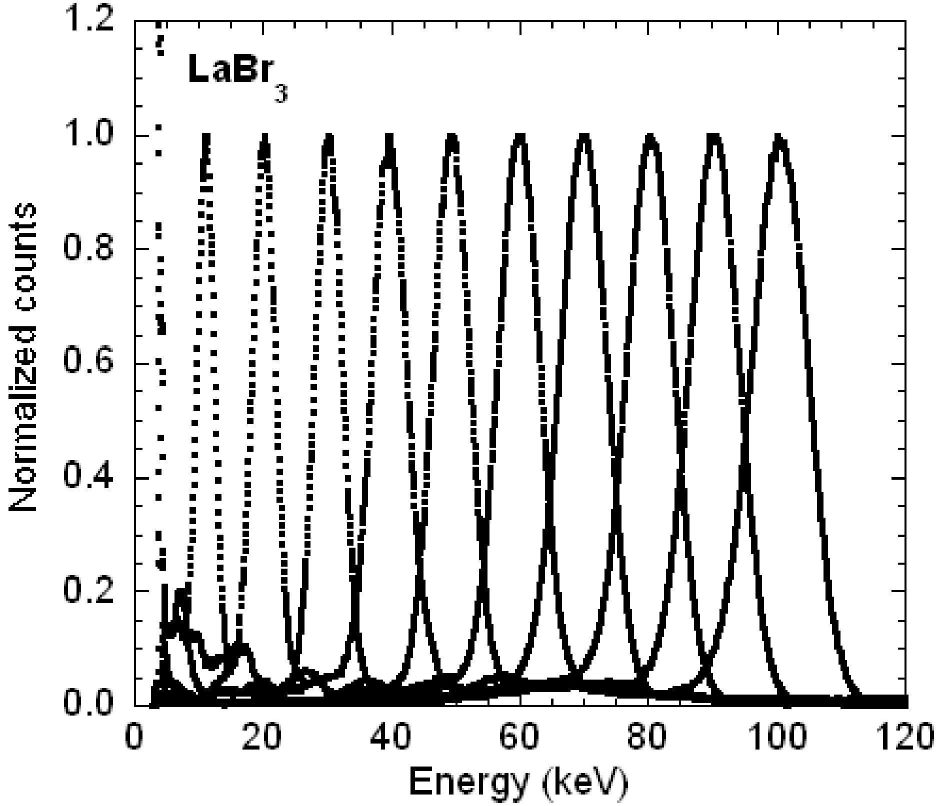

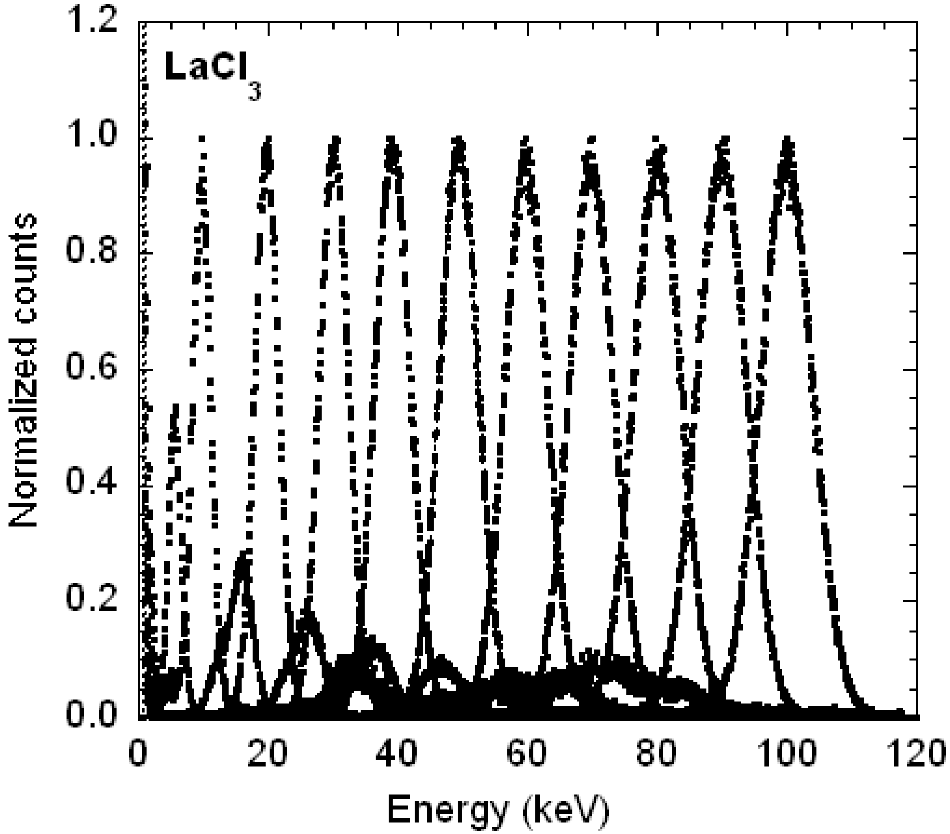

ΔE @ 60 keV ~ 10% ($LaBr_3$) and 12% ($LaCl_3$)
ΔE @662 keV=3.0% ($LaBr_3$) and 4.1% ($LaCl_3$)

Scintillator studies - non-proportionality

Large change in linearity below the La edge

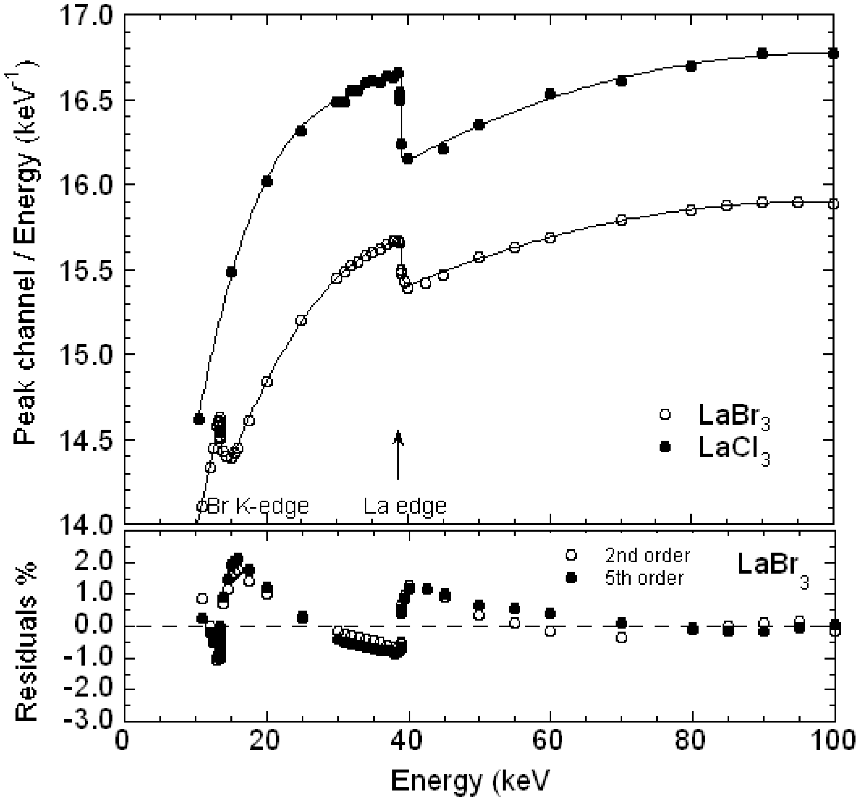

Owens et al., *The hard X-ray response of Ce-doped lanthanu halide scintillators*, Nucl. Instr. Meth.,**574** (2007) 158

Latest work from TU Delft

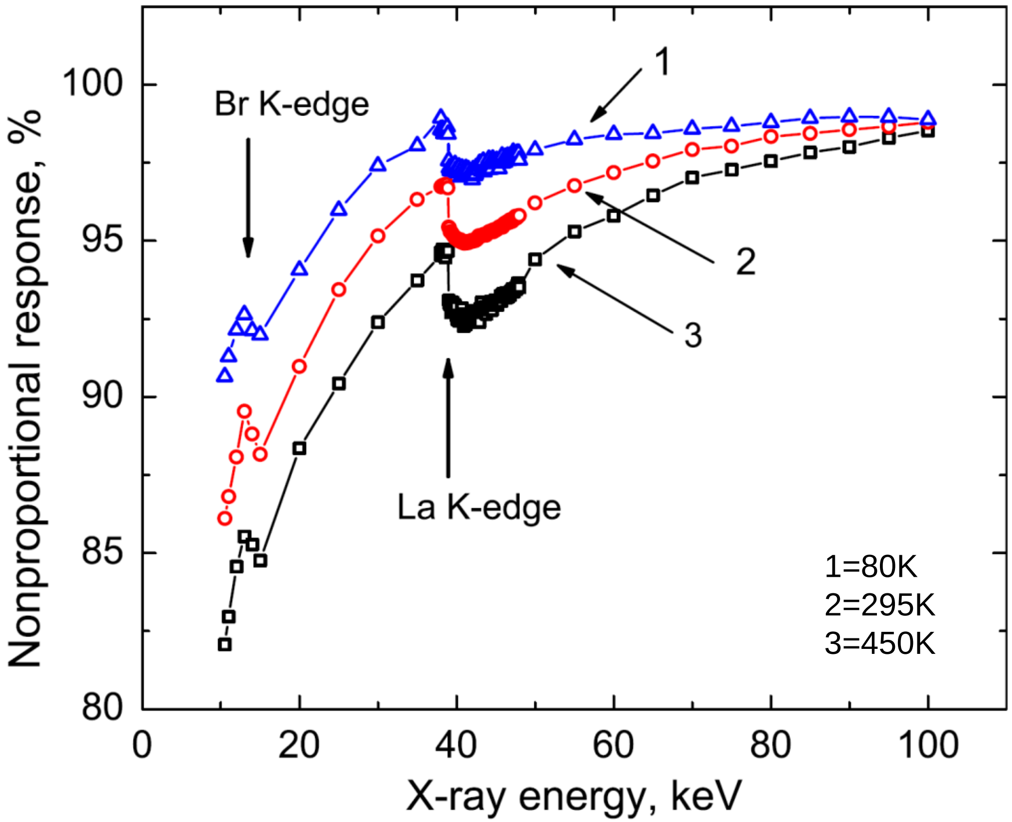

Khodyuk et al., *Improved scintillation proportionality and energy resolution of LaBr3:Ce at 80K*, Nucl. Instr. Meth., **642** (2011) 75.

Scintillator studies - non-proportionality

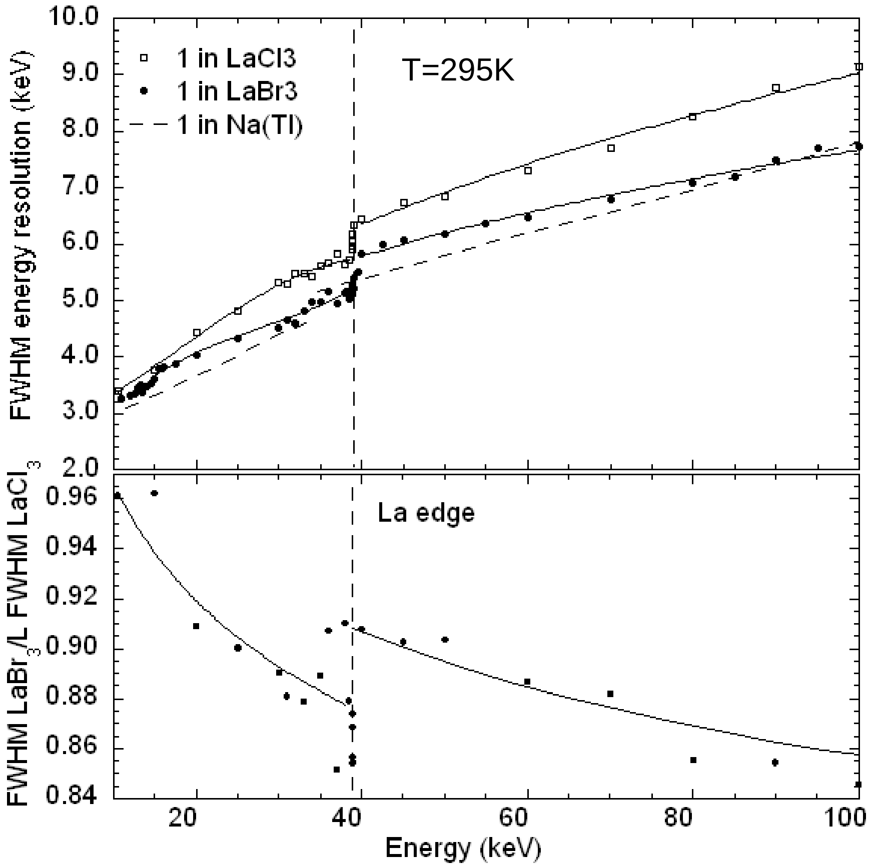

Owens et al., *The hard X-ray response of Ce-doped lanthanu halide scintillators*, Nucl. Instr. Meth.,**574** (2007) 158

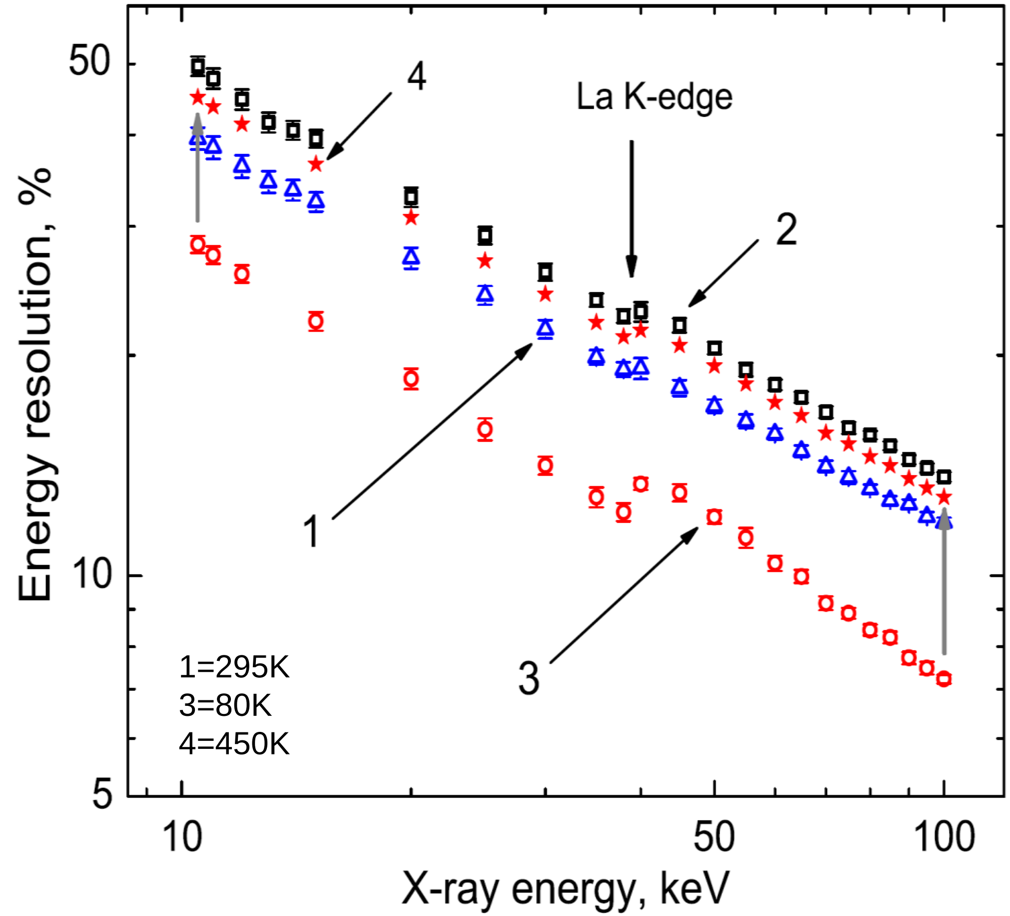

Khodyuk et al., *Improved scintillation proportionality and energy resolution of LaBr3:Ce at 80K*, Nucl. Instr. Meth., **642** (2011) 75.

Non-proportionality - K-dip spectroscopy (TU Delft)

Can obtain high accuracies down to 30eV. More accurate than CCT below 3keV

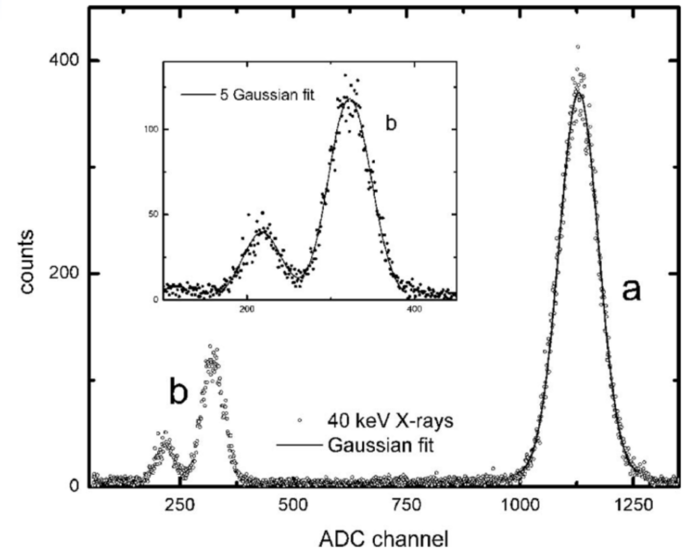

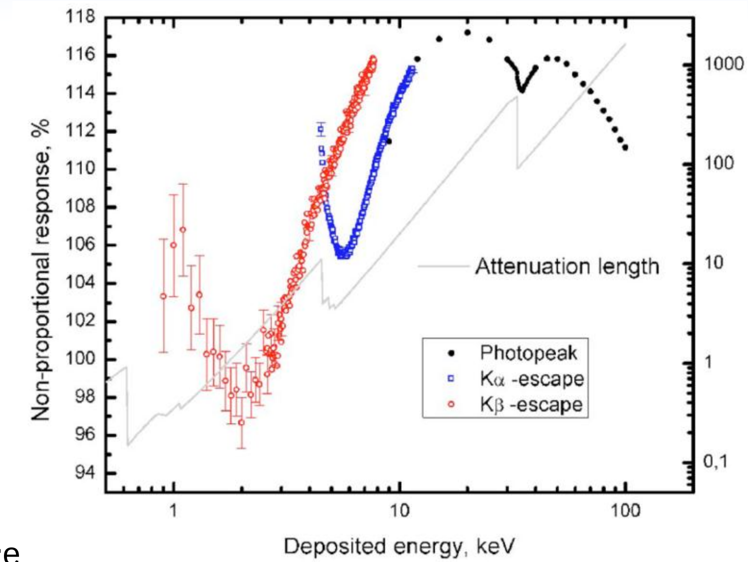

$$E_d = E_X - E_e$$

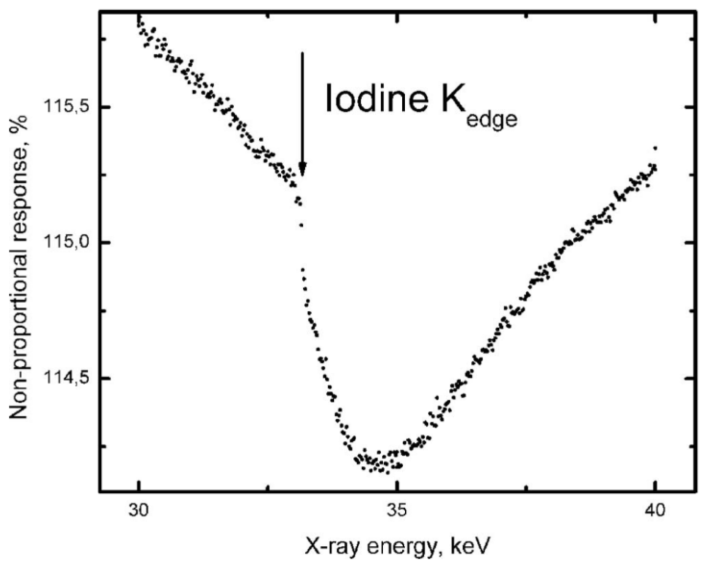

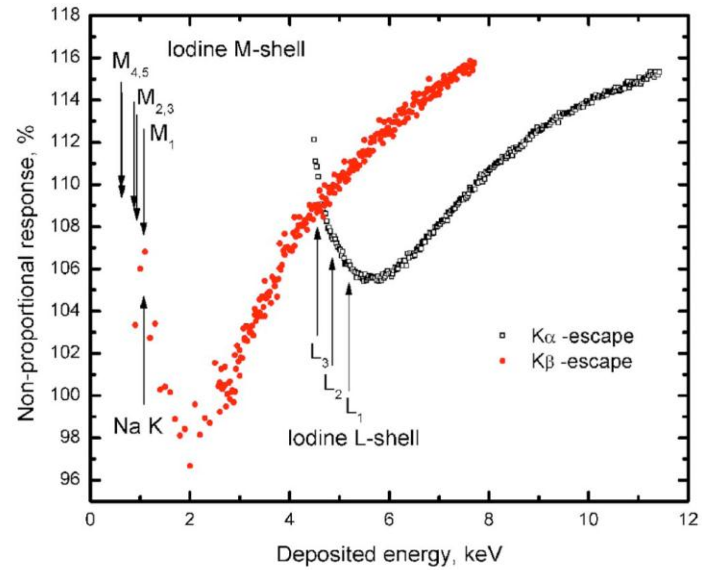

Khodyuk, et al. *Nonproportional scintillation response of NaI:Tl to low energy x-ray photons and electrons,* J. Appl. Phys., **107**(2010) 113513 2

XAFS structure

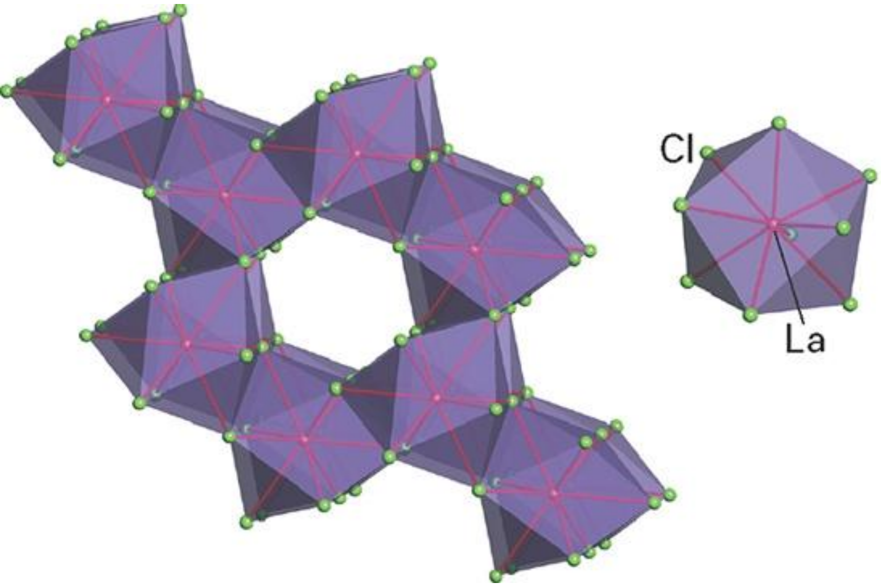

UCl3 type lattice with P63/m space group

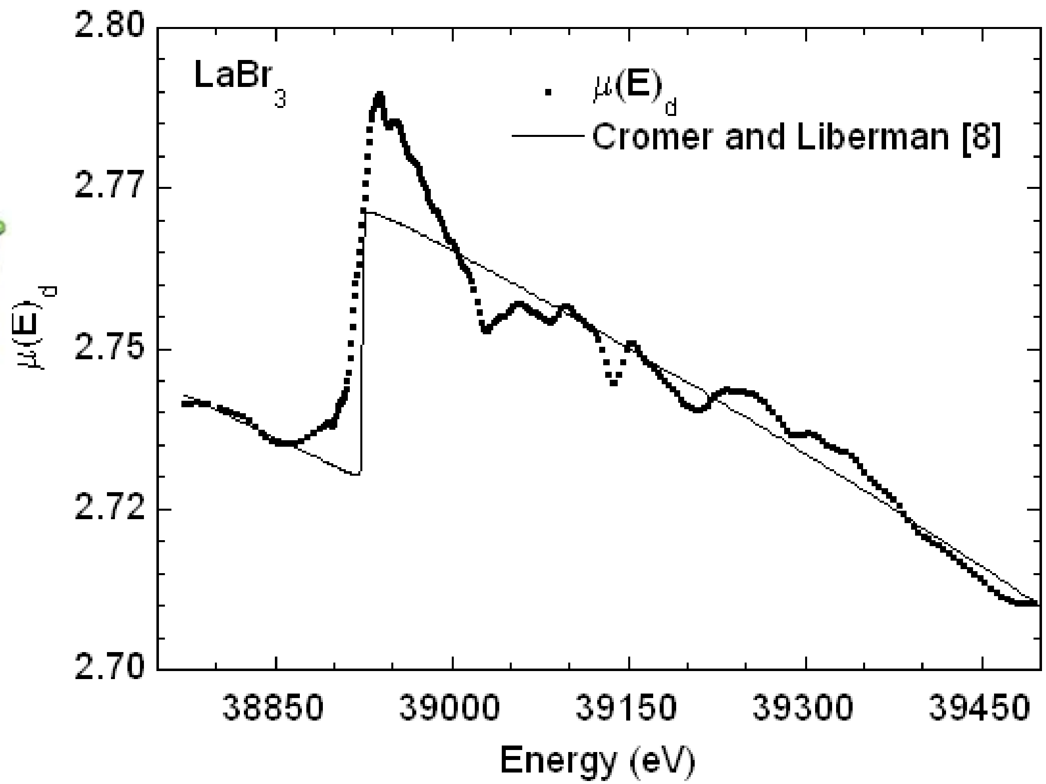

Little evidence for extended fine structure suggesting that the bulk of the structure arises from the local coordination environment. Lanthanum halides crystallize with hexagonal symmetry around a. It is assumed that when doped, the Ce atoms uniformly replace the La atoms—and this could be a source of disorder leading to a suppressed EXAFS signal.

Owens et al., *The hard X-ray response of Ce-doped lanthanum halide scintillators*, Nucl. Instr. Meth.,574 (2007) 158 esa

X-ray Absorption Spectroscopy and Metrology

XAFS and metrology

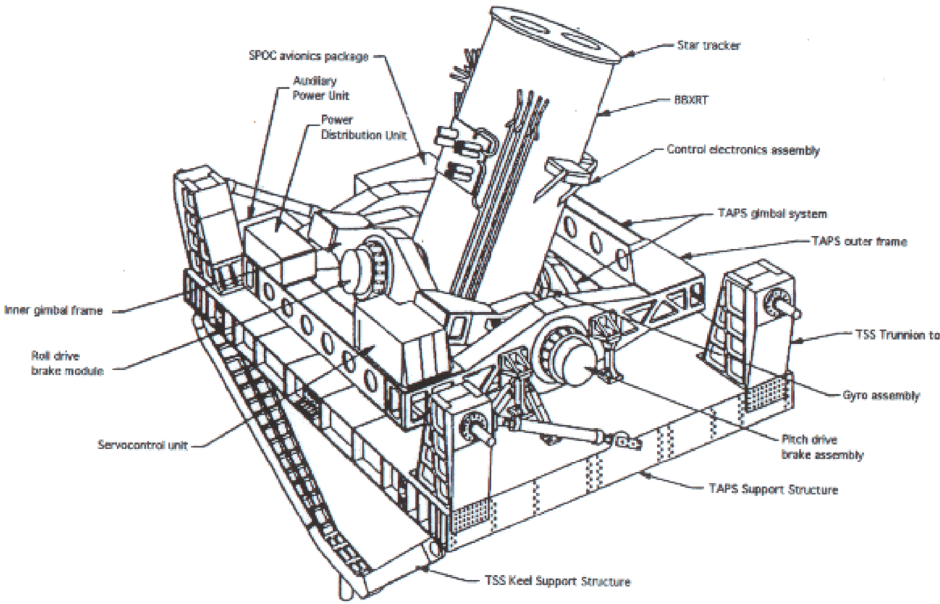

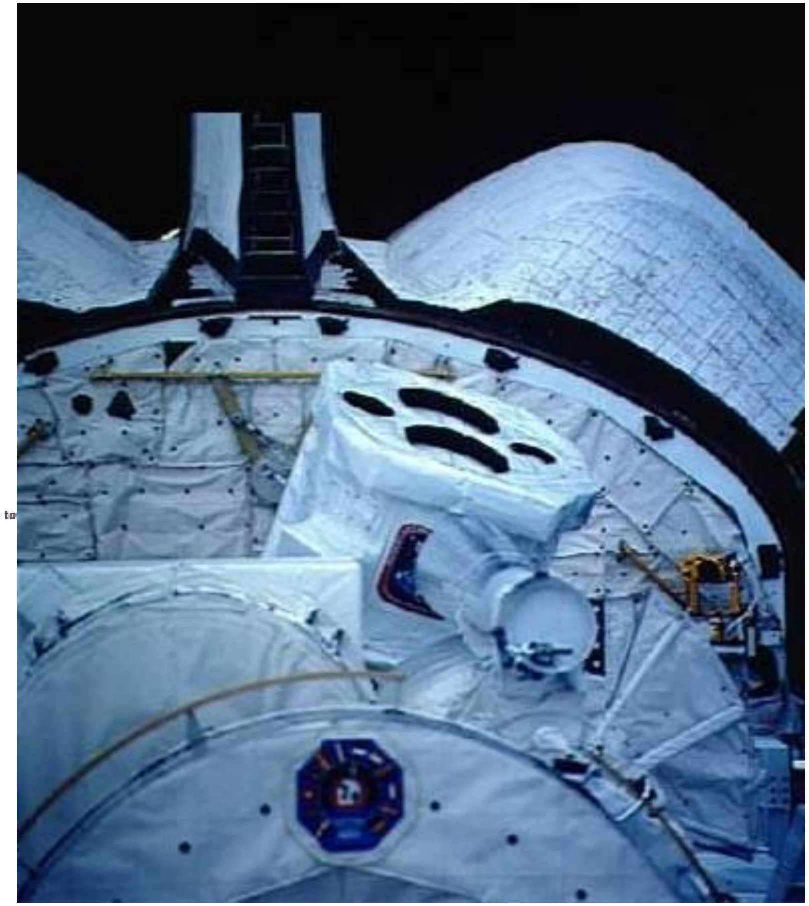

The Broad Band X-ray Telescope (BBXRT) was flown on the space shuttle Columbia (STS-35) on December 2-11, 1990, as part of the ASTRO-1 payload. The flight of BBXRT marked the first opportunity for performing X-ray observations over a broad energy range (0.3 to 12 keV) with moderate energy resolution (150 eV at 6 keV). The BBXRT consists of a pair of coaligned thin foil conical X-ray mirrors, with a cryogenically-cooled, Si(Li) spectrometer at the focus of each.

X-ray Absorption Fine Structure

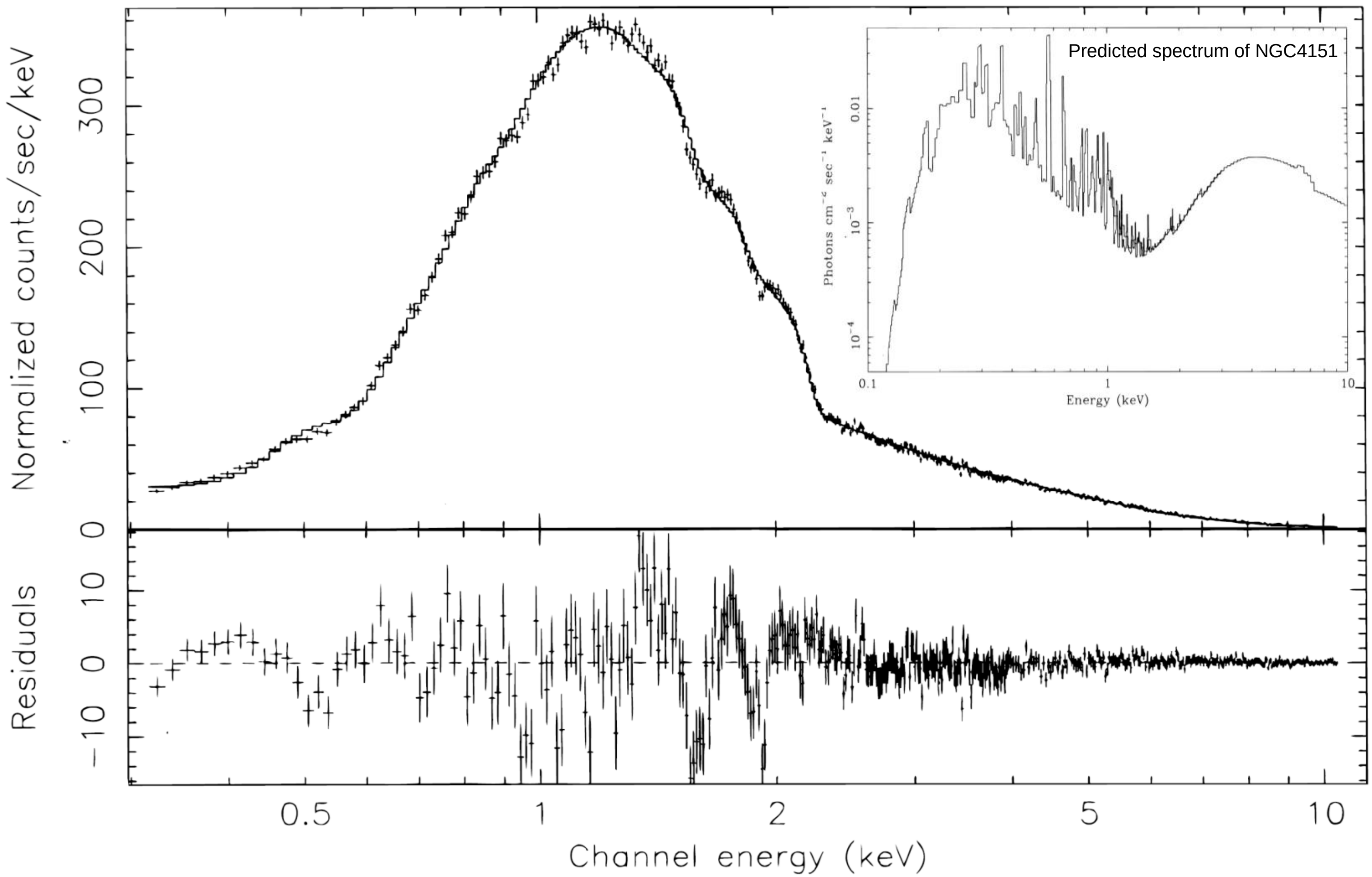

FIG. 1.—Measured BBXRT spectrum of the Crab Nebula. The solid line is the best-fit absorbed power law through the data points. The bottom panel shows the residual count rate after the underlying continuum has been subtracted, illustrating dramatically the effects of XAFS. Features at energies appropriate for the Si, Al, and O edges can be delineated clearly in the residuals.

Owens et al., *The Effect of X-Ray Absorption Fine Structure in Soft X-ray Astronomical Telescopes,* Ap. J., **476** (1997) 924

What is X-ray Absorption Fine Structure?

X-ray Absorption Fine Structure (XAFS) occurs due to interference effects as photoelectrons leave the surface of a material following photoabsorption. The interference depends on the interatomic distance between the atom that ejected the photoelectron and the nearest neighbour atom, and to lesser extents the next nearest neighbour and other atoms.

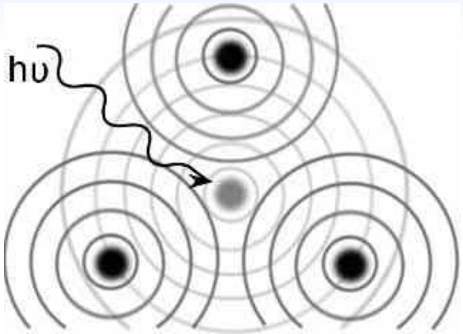

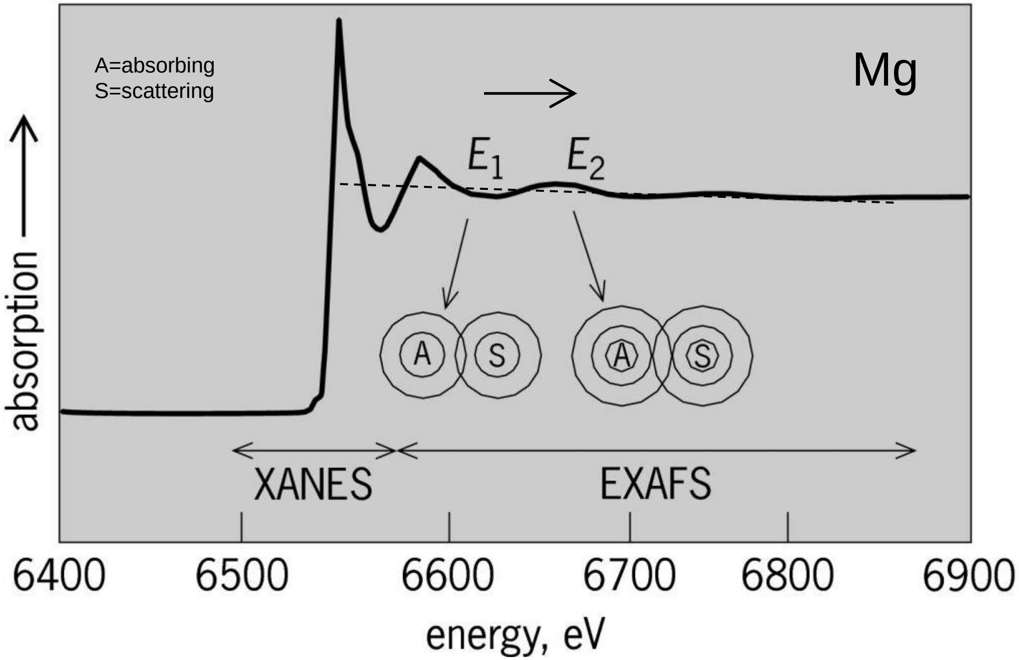

<u>XAS spectra are usually divided in three energy regions</u>

<u>Edge</u> – the edge including the white line

XANES – X-ray Absorption Near Edge Structure attributed to multiple scattering processes leading to structure within about 50 eV of the edge. Much larger signal than EXAFS

Sensitive to electronic structure and symmetry

EXAFS – Extended X-ray Absorption Fine Structure attributed to single scattering processed leading to oscillatory structure up to ~few hundred eV above the edge. Influence over larger energy ranges than XANES

Sensitive to bond distances, coordination numbers and local disorder

de L. Kronig, R., *Z. Phys.*, 1931, vol. 70, p. 317.

Post BBXRT – The X-ray observatories

XMM-Newton:

- Energy range 0.1 – 15 keV
- Mirror area 0.4 m^2
- Focal length 7.5 m
- Spatial resolution 15″ HEW
- Energy resolution 130 eV @ 5.9 keV
- Δ E/E = 500 @ 0.5 keV
- Limiting sensitivity: 10^{-15} erg cm^{-2} s^{-1}

Chandra:

- Energy range 0.1 – 10 keV
- Mirror area 0.08 m^2
- Focal length 10 m
- Spatial resolution 0.5″ HEW
- Energy resolution 130 eV @ 5.9 keV
- ΔE/E = 400-1000 @ 0.5 keV
- Limiting sensitivity: 10^{-16} erg cm^{-2} s^{-1}

X-ray transmission, absorption and reflection

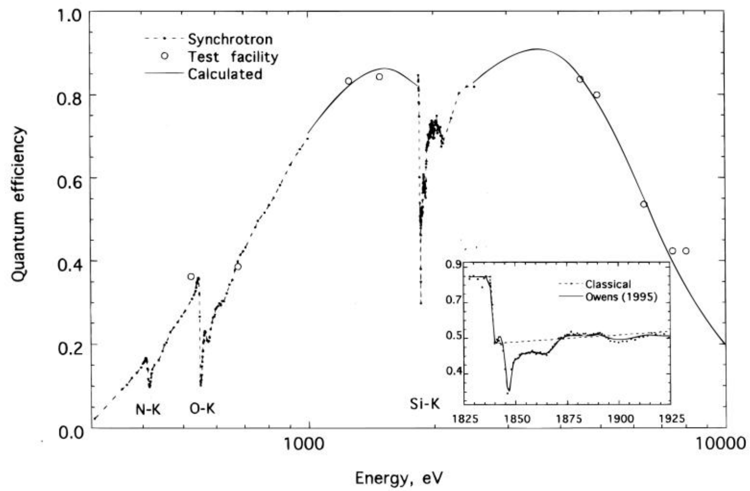

FIG. 3.—The measured CCD quantum efficiency for 1–4 pixel events. For comparison, we show also individual discrete line measurements (*open circles*) along with Monte Carlo calculations (*lines*). The inset shows an expansion in the region of the Si K-edge. As expected, the quantum efficiency above the edge shows considerably more structure than that expected from silicon alone, showing clear evidence of a strong SiO_2 component. For comparison, we show also the shape of the edge predicted from standard atomic and nuclear data tables and on newly measured cross sections.

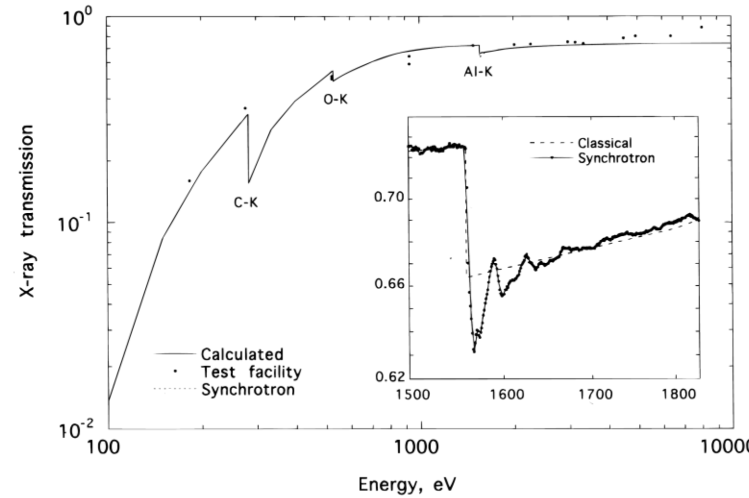

FIG. 4.—The soft X-ray transmission efficiency as a function of energy for the 800 Å JET-X optical filter. The curve is a composite of calculation (based on the classical tables of Saloman et al. 1988) and SRS measurements normalized by discrete line measurements. The inset shows an expansion in the region of the Al K-edge.

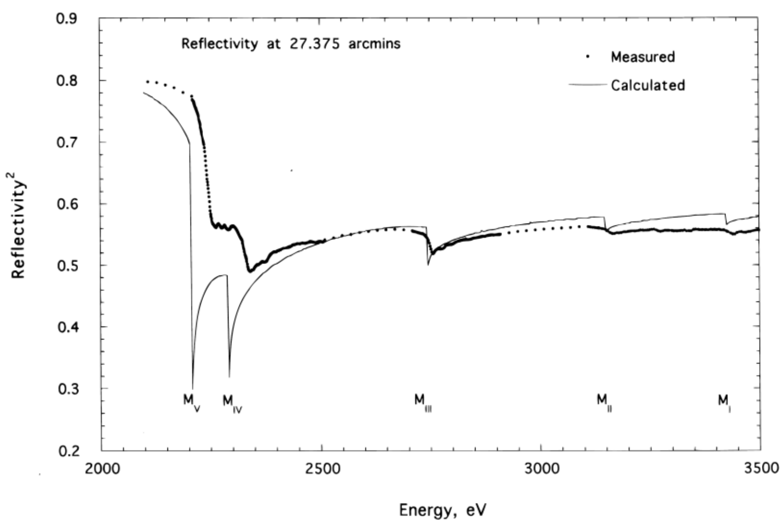

FIG. 5.—Predicted JET-X mirror reflectivity for an angle of incidence of 27.375 based on single reflectivity Au measurements. For comparison, we show also calculated values based on the calculations of Cromer & Liberman (1970).

The Effect of X-Ray Absorption Fine Structure in Soft X-ray Astronomical Telescopes, Ap. J., **476** (1997) 924

Apparent discrepancy between measured and tabulated M absorption edge energies, Ap.J., **468** (1996) 451

Woo, *EXAFS and XANES: New Astrophysical Tools to Study the Solid State Structure of Interstellar Grains***,** Ap. J., **447** (1995) L129

Understanding the response function, spectral unfolding

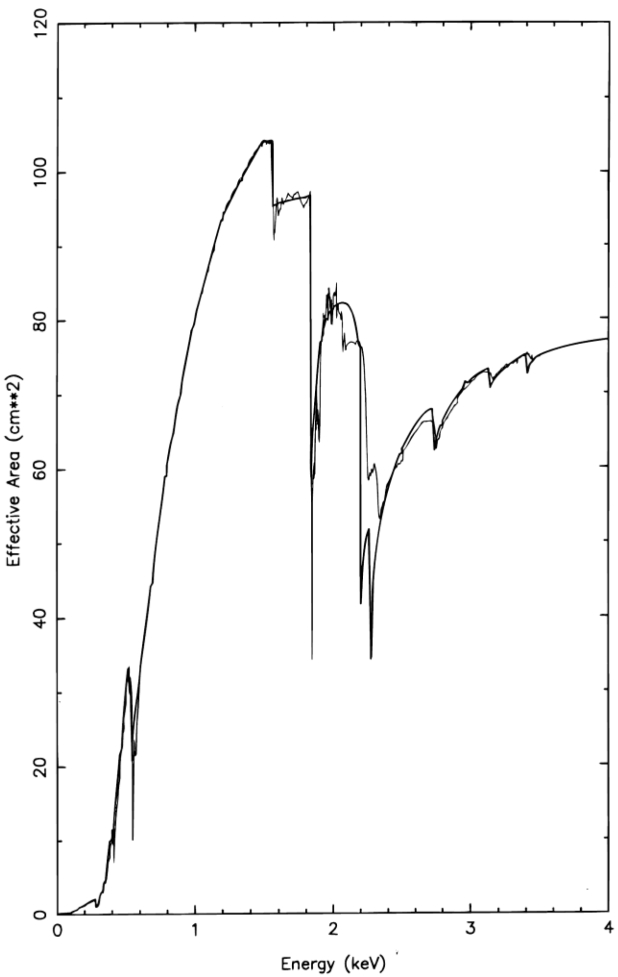

FIG. 6.—The full-up effective area for the JET-X telescope. Two curves are given one for which the detailed edge structure was input from direct measurement (*thin line*) and the other in which the edge shapes were calculated using cross sections (*thick line*).

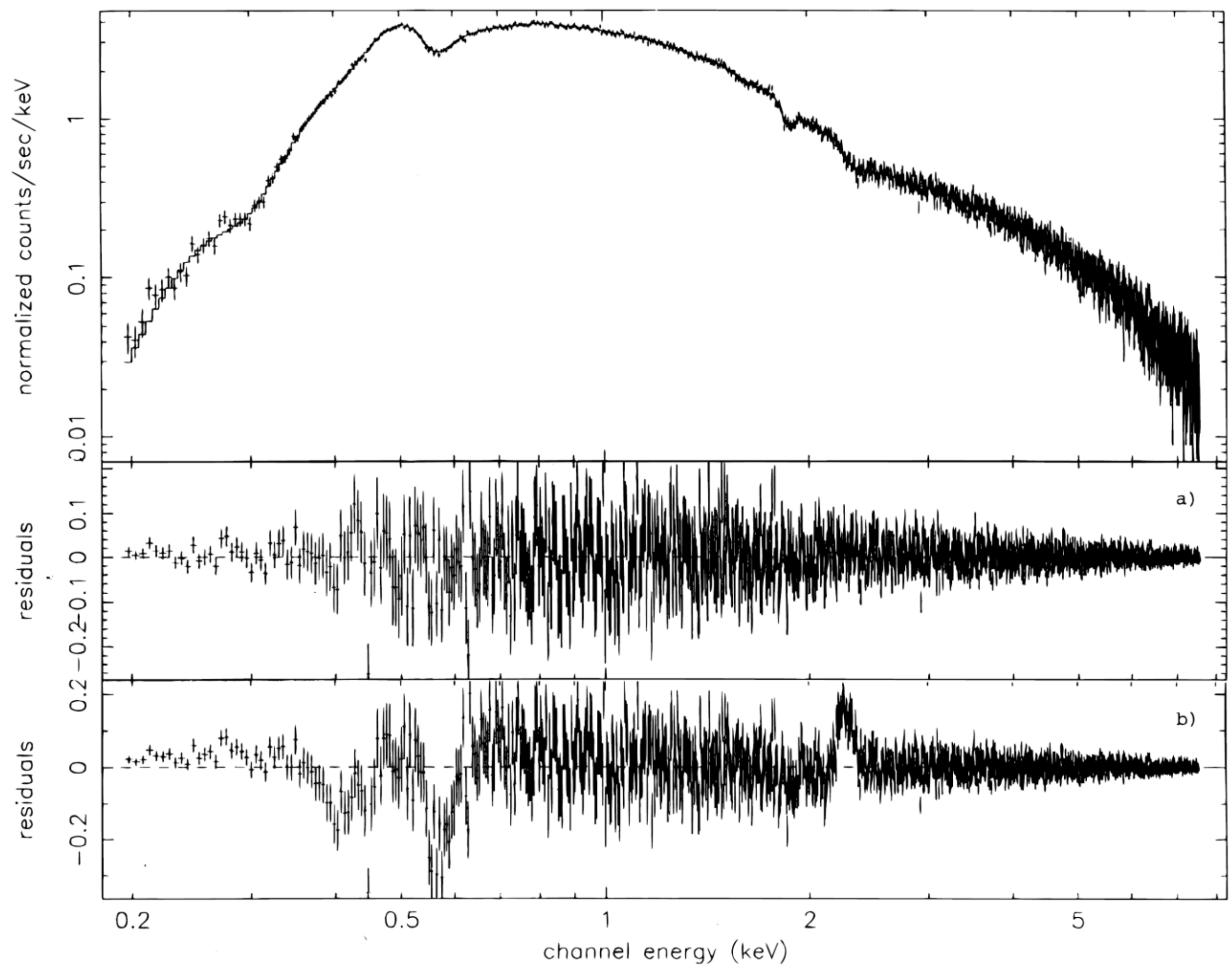

FIG. 7.—Measured energy-loss spectrum for a 10^5 observation of a 10 millicrab source. The solid line shows the folded source model through the measured response function. The residuals (i.e., measured spectra − model spectra) shown below are for two cases: (*a*) where the data have been unfolded using the XAFS response function and (*b*) where the data have been unfolded using the classical response function (see text).

XMM Newton

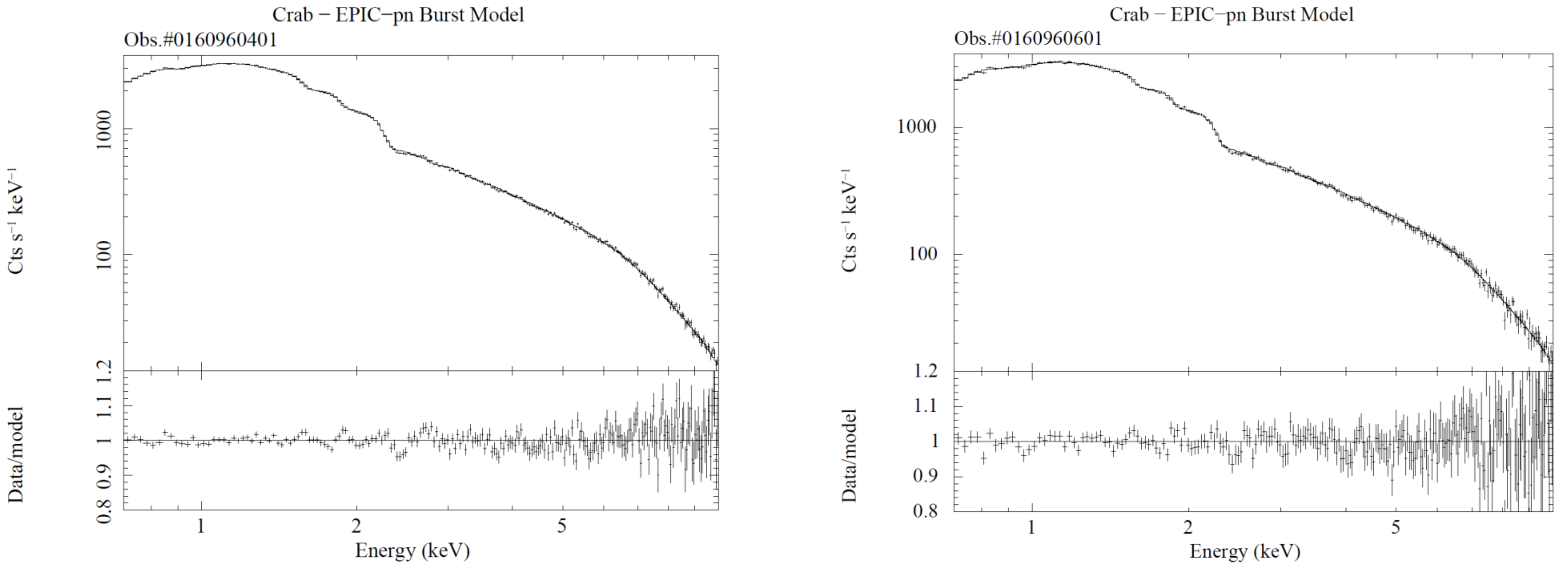

Figure 4: Spectra (*upper panels*) and residuals in units of data/model ratio (*lower panels*) when the Crab spectra of Obs.#0160960401 (*left panel*) and 0160960601 (*right panel*) are fit with a photoelectrically absorbed power-law (cf. Tab. 2). For plotting purposes only, spectra are rebinned in such a way that each spectral channel has got a signal-to-noise >10.

XAFS, surface metrology and process control

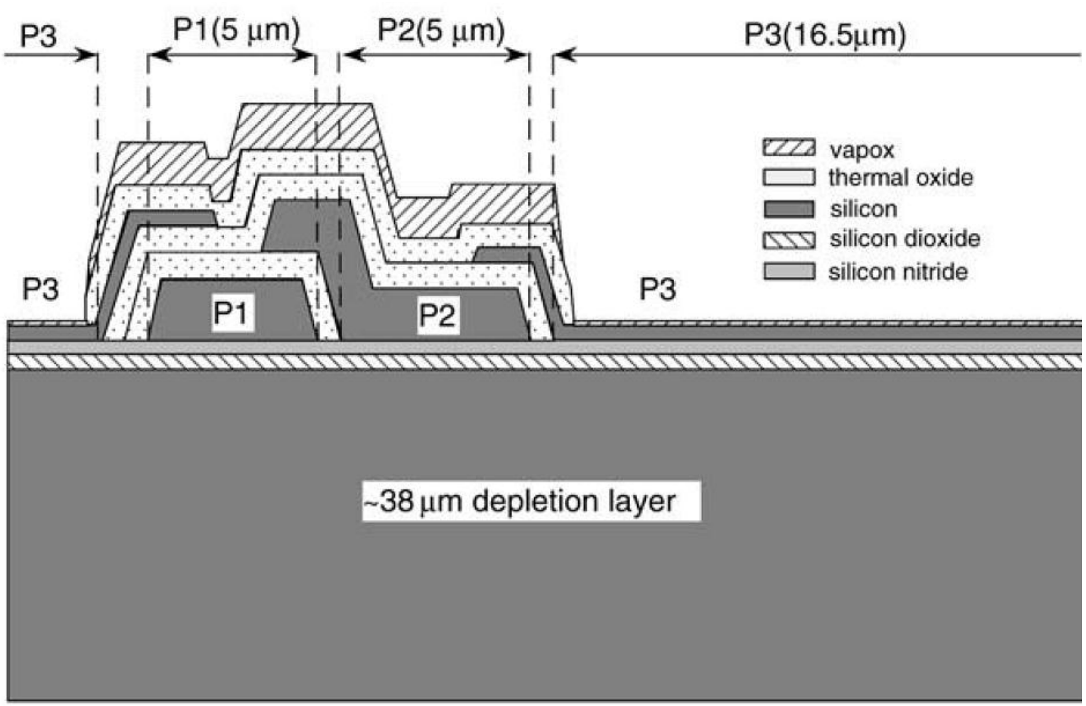

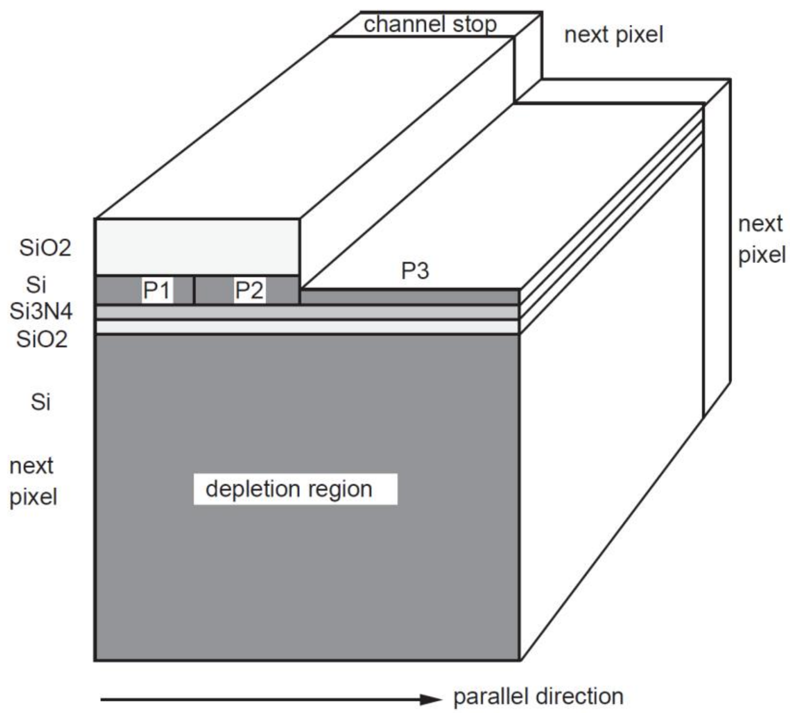

Single pixel of an EEV large area 20.7 × 27.6 mm^2; multi-pixel (768 × 1024) three-phase front-illuminated MOS X-ray CCD

Simplified cross-sectional view

From the depletion region outwards: SiO_2 850Å (100%) passivation layer, Si_3N_4 (850Å) dielectric layer, SiO_2 8000Å (50%), Si 1700Å (P3), thermal oxide (100Å)

A. Owens, Nuclear Instruments and Methods in Physics Research A 526 (2004) 391–398

Step 1- Measure the quantum efficiency

Low current run – full area illumination

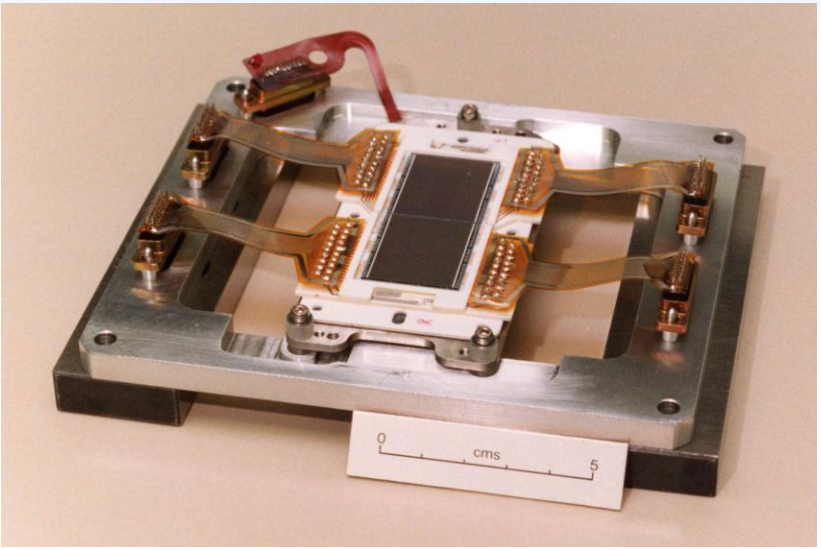

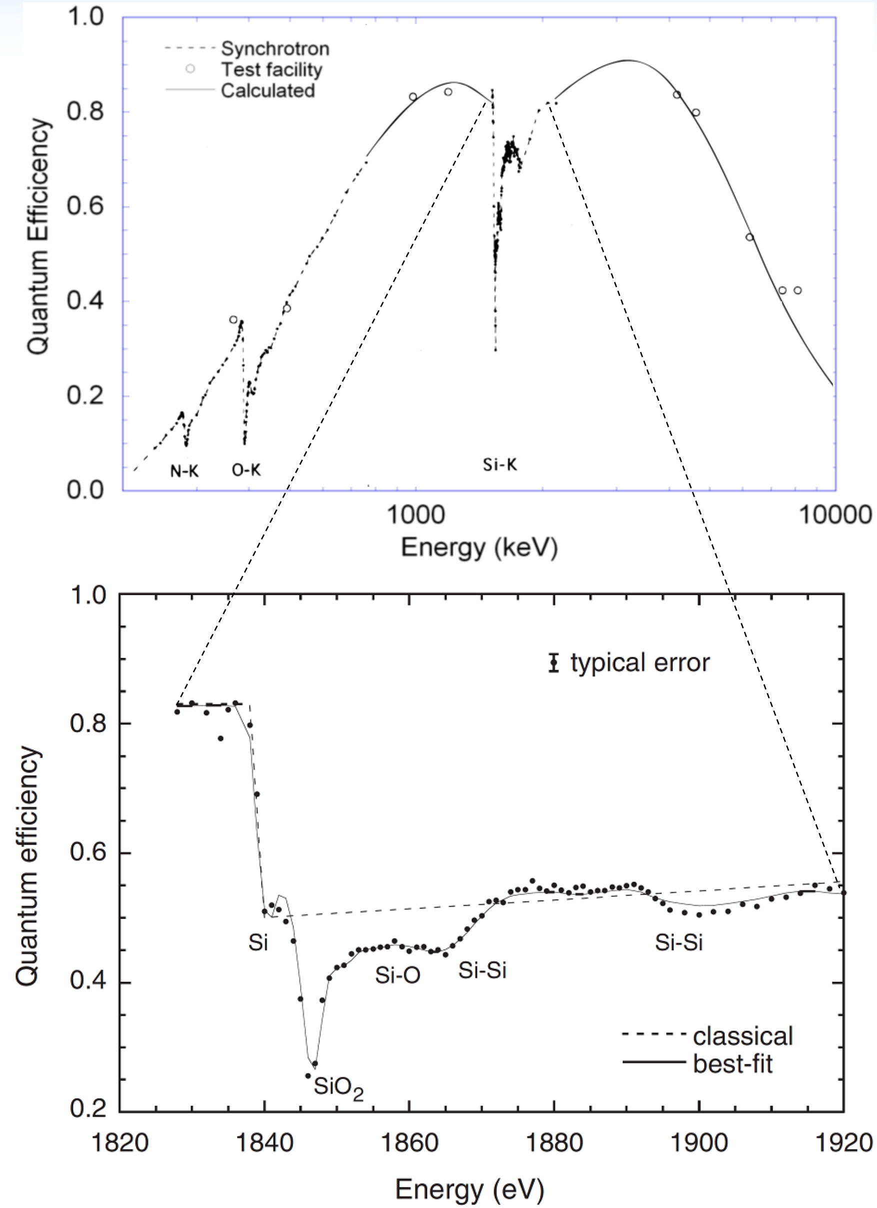

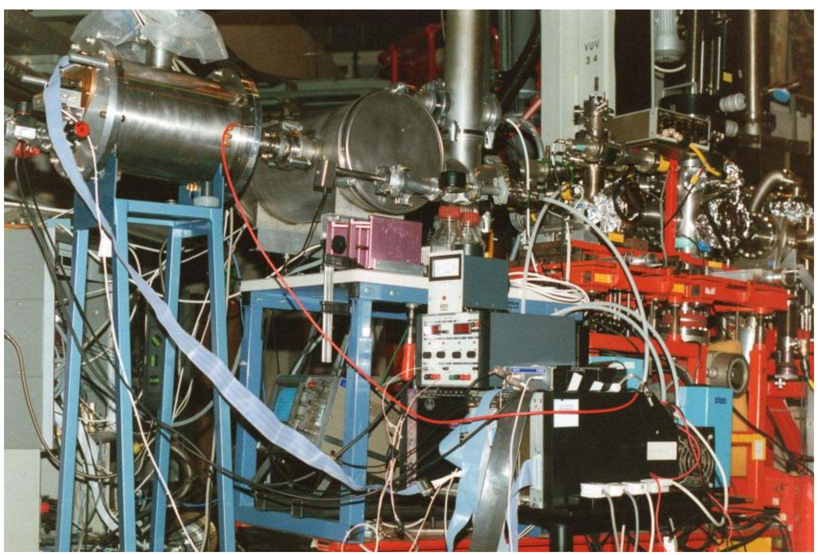

SRS beamline 3.4, InSb[111]

Step 2 – measure the near edge cross sections

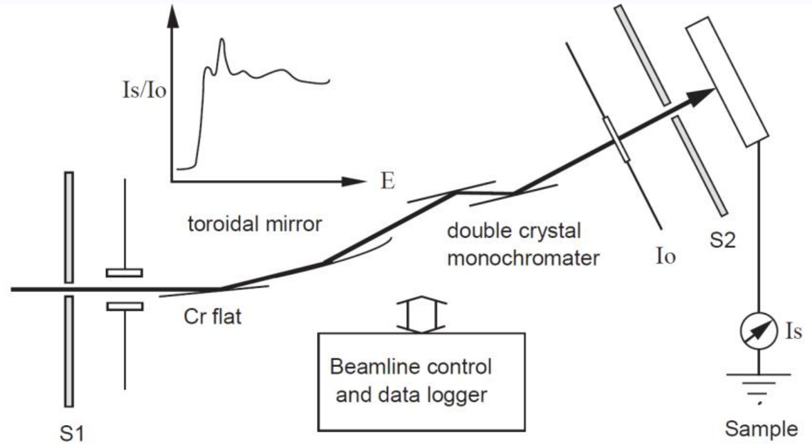

Fig. 1. The experimental configuration of beamline 3.4 at the Daresbury SRS.

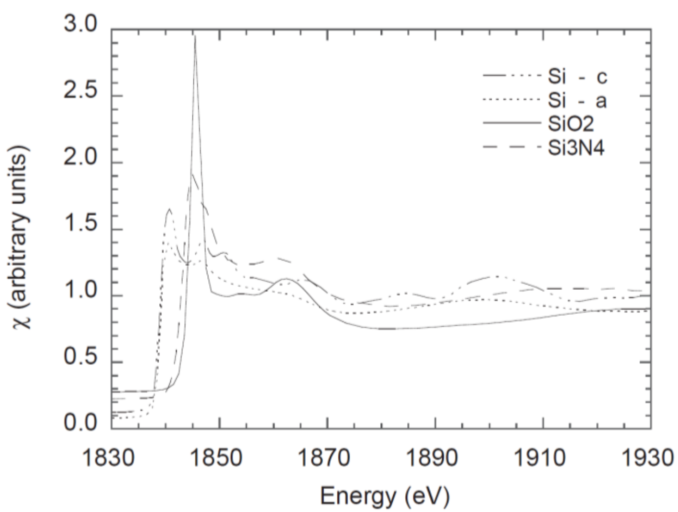

Fig. 2. Measured photocurrent X-ray absorption fine structure from a crystalline Si sample (c), an amorphous Si sample (a), an amorphous SiO_2 sample and an amorphous Si_3N_4 sample.

$$\chi(E) = \mu(E)\{\alpha + \beta E\}$$

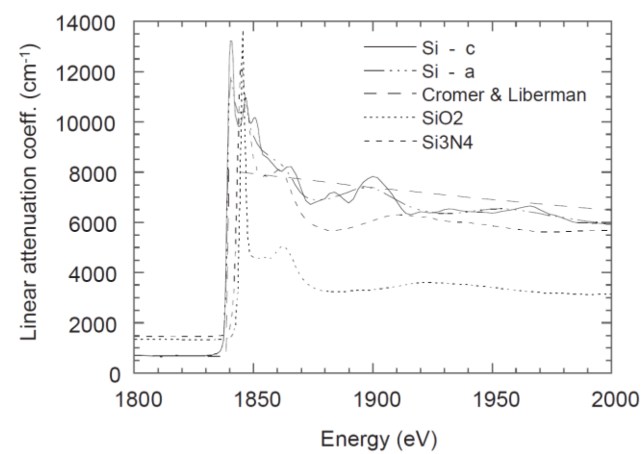

Fig. 3. The derived linear attenuation coefficients across the Si K-edge. For Si, the letters c and a refer to crystalline and amorphous. We also show the 'classical' Si curve based on the calculation of Cromer and Liberman (1970).

 A. Owens et al., *Near K-edge linear attenuation coefficients for Si, SiO_2 and Si_3N_4* Rad. Phys. & Chem., **65** (2002) 109.

Step 3 – fit the quantum efficiency

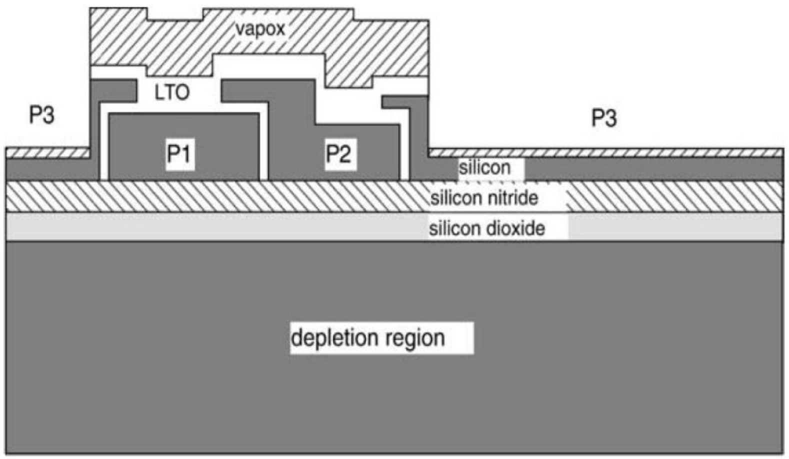

Simplified CCD geometry assumed in the model.

$$\mathrm{QE} = \frac{1}{p}[1 - \exp(-\mu_d d)] \times \int_0^p \prod_{i=1,n} \exp[-a_i(x)(\mu_e)_i t_i]\, \mathrm{d}x$$

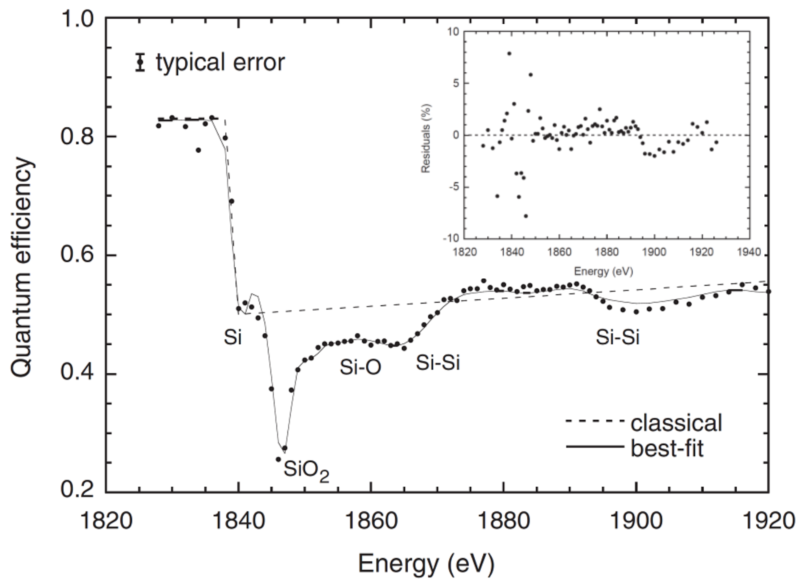

Comparison of the thicknesses of surface structures specified by the manufacturer and those derived by best-fitting the measured quantum efficiency

Structure	Manufacturers spec. (μm)	Best fit (μm)
P1, P2	0.65 ± 0.13	0.51 ± 0.10
P3	0.17 ± 0.03	0.26 ± 0.07
Vapox + LTO	1.2 ± 0.24	1.06 ± 0.11
P3 SiO_2	<0.01[a]	0.11 ± 0.04

[a] Re-measured to be 0.1 μm.

Precisions of 1%
Factor of 2 better than process control
Combined with XPS, possible to tomographically isolate features